DNA Polymer Physics in Complex Nanofluidic Environments

Alexander R. Klotz

Doctor of Philosophy

Department of Physics

McGill University

Montreal, Quebec

June 2015

A thesis submitted to the Faculty of Graduate Studies in partial fulfilment of the requirements for the degree of Doctor of Philosophy

ABSTRACT

A complex nanofluidic device consisting of a slit embedded with an array of nanopit cavities is used to study the physics of confined DNA. By measuring the number of cavities occupied by a molecule in varying geometries, the entropic free energy of confinement and effective molecular width were measured. By measuring the correlation time of contour fluctuations between two pits, the dependence of the dominant relaxation modes on the local free energy landscape was investigated. By measuring the fraction of a molecule occupying single pits of varying size, the effects of excluded volume interactions in cavities were studied. The results were considered in light of a model for the free energy of confinement taking into account semi-flexibility, excluded volume, and entropic elasticity, components of which were developed to understand these experiments.

RÉSUMÉ

Nous utilisons un dispositif nanofluidique complexe avec une fente composé d'un treillis des fosses, et étudions la physique de l'ADN confiné. Nous mesurons le nombre de fosses qui sont occupées pour une molécule en différentes géométries. Nos données démontrent l'énergie libre de confinement entropique et la largeur effectif de l'ADN. Nous mesurons le temps de corrélation des fluctuations du contour entre deux fosses, et le dépendence des modes de relaxation sur le potentiel. Ensuite, nous mesurons la fraction d'une molécule qui occupe des fosses uniques de taille variable, et nous étudions les effets stérique dans des cavités. Nous considérons les résultats en tenant compte d'un modèle pour l'énergie de confinement qui comprend la semi-flexiblité, la volume exclu, et l'élasticité entropique. Ce modèle a été développé afin d'interpréter les résultats.

ACKNOWLEDGEMENTS

The four years of my Ph.D. have been some of best of my life. I am proud to have shared them with the other graduate students in the McGill physics department, and the friends I have come to know in Montreal. I hope the relationships I have forged here will be an ever-present part of my life. My family has always supported me in my academic endeavours, athough they were sad to see me leave my hometown for so long. I am greatful for the help I received over the past several years from people who dedicated their efforts to this project for almost nothing in return. These include Hugo Brandao, Philippe Fortin Simard, Simon Papillon, Lyndon Duong, Laurence Coursol, and Mikhail Mamaev. I am also greatful to Hendrick de Haan and Jeff Chen, for developing the theoretical models required to fully understand this project. I appreciate the help that other members of Walter's research group have given me over the years, and the camaraderie between Rob Welch, Yuning Zhang, Ahmed Khorshid and myself, whose struggles mirror those of one another. I am greatful to my supervisor Walter Reisner for his guidance and for making my graduate years possible, and for providing me with a project that so closely met my interests.

Statement of Originality and Contribution

This thesis represents the work I have done at McGill over the past four years, which is an extension of the project I began for my master's project in 2009. It has lead to several new discoveries in the field of DNA nanofluidics, which have been or will be published in the journal Macromolecules with myself as the first author. These include a paper on diffusion published in 2012, a paper on fluctuations that has been published after initial submission, and a paper on free energy measurements that has been published after initial submission. A theoretical paper was written by Hendrick de Haan, a co-author on my 2015 papers, to help understand the underlying physics of my experiments, and it has been published in MacroLetters. One aspect of the analysis code was written as a summer project by Hugo Brandao, who is an author on my 2012 paper. Some experimental work and data analysis was performed by Mikhail Mamaev and Lyndon Duong, who are co-authors on my 2015 papers, as well as Laurence Coursol who may appear as a co-author on a potential fourth paper. Jeff Chen developed a new theoretical model for my project and is a co-author on one fo the papers, and may write up his theoretical work separately. The entire project was under the supervision and guidance of Walter Reisner.

Explicitly, the distinct contributions to scientific knowledge in this thesis are: demonstration of controllable macromolecular diffusion using nanotopography, measurement of the entropic free energy of confinement in slits and cavities and the verification of the Chen-Sullivan formula, measurement of the effective width of DNA on a single-molecule basis and its scaling with ionic

strength, experimental and theoretical mapping of the stable-unstable pit occupancy transition, observation of two harmonic modes in nanoconfined DNA, measurement of the correlation time-scales of these modes, and their scaling, measuring the speed of tension propagation through confined DNA, measurement of single-molecule partitioning into cavities and its scaling, measurement of a partitioning peak corresponding to a transition in slit physics, measurement of the fluctuations in the partitioning and its surpression due to finite size effects.

TABLE OF CONTENTS

CHAPTER 1
Introduction

1.1 Complex Nanofluidic Environments

Over the past decade, a field has emerged dedicated to studying the behaviour of isolated DNA molecules confined in nanofluidic environments. Nanofluidic environments, such as channels, slits, and cavities created in glass with electron-beam lithography, can confine macromolecules in spaces far below their typical size, altering their equilibrium and dynamic properties. Interest in this field comes from the fact that DNA is stretched at equilibrium by nanoconfinement, allowing genomic information to be read in a spatially organized manner, and from connections to polymer physics for which DNA is the best model system. From an applications perspective, the DNA-nanoconfinement field has been driven largely by interest in single-molecule nanochannel-based mapping technologies. After a decade of intense experimental and theoretical effort, the physics of DNA in nanochannels has become well understood in recent years, and applications are becoming mainstream. What is less-understood and under-utilized compared to nanochannels are systems of *complex nanoconfinement*.

In contrast to simple nanofluidic systems such as nanochannels or nanoslits that force the molecule to extend in one or two dimensions, complex nanoenvironments offer multiple scales of confinement and regions of varying dimensionality and topography (Figure 1–1). For example, a complex nanofluidic

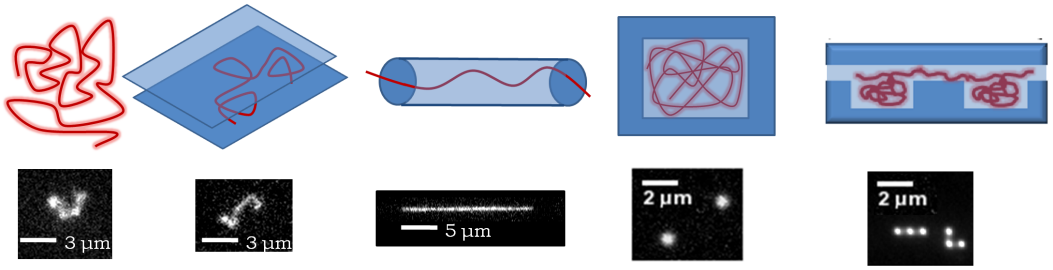

Figure 1–1: Schematics of polymer chain behaviour under different types of confinement, compared to fluorescent DNA images. From left to right: bulk, quasi-2D (nanoslit), quasi-1D (nanochannel), quasi-0D (nanocavity), and complex nanoconfinement.

geometry might contain slit regions of varying height, such that a free-energy variation induces partitioning of the chain between the different regions. An early example of a complex nano-environment is an electrophoretic gel, where DNA is confined in cavities separated by small pores, leading to a length-dependent mobility that can separate molecules by size. Size-exclusion chromatography operates on similar principles, using excluded volume interactions to segregate different sizes of macromolecules. Entropic sieving devices, consisting of arrays of microcavities connected by nanoslits, operate on a similar principle, where the probability of a chain escaping each entropic trap depends on its length. Recently, a new genetic sequencing technology has been developed that confines small sections of a molecule in a micro- or nano-cavity that acts as a zero-mode waveguide for incident light, allowing individual fluorophores to be read. Using "top-down" nanofabrication techniques, precisely defined nano-environments that enable controlled partitioning, and serve as model systems to study other complex environments found in biology or industrial systems. Many applications relate to biopolymer size-separation, a necessary step in many bio-assays such as genetic sequencing.

All of these devices rely on the fact that entropy is restricted in narrow environments, and a polymer chain will partition most of its contour into a wider nano-environment, while minimizing the contour in a narrower nano-environment. In this thesis, I study the partitioning of DNA between different regions of confinement in a complex nano-environment, to study the underlying physical principles that dictate equilibrium partitioning in complex nanofluidic systems. The complex nanofluidic system chosen here consists of a nanofluidic slit, with a height on the order of 100 nanometers, which is embedded with a lattice of square cavities (or pits) etched into one of the walls of the slit to twice the depth of the slit. Because the cavities are twice as deep as the slit, a chain can increase its entropy by partitioning contour into them, but if the concentration in the cavities becomes sufficiently high, excluded volume interactions drive contour back into the slit, and the equilibrium configuration is a balance of these considerations. Such devices have previously been used to study molecular self-organization, where it was shown the non-trivial equilibrium structures could be dictated using complex nanotopography [1]. These devices have been used to show that mobility can be controlled using complex nanotopography to halt driven molecules [2], making an analogy to the "lakes-straits" model of gel electrophoresis. The research in this thesis takes this type of device beyond the phenomenological level, and uses complex nanotopography to make precision measurements of quantities relevant to fundamental polymer physics that have not been measured before.

1.2 DNA as a Model Polymer

This thesis studies the behaviour of DNA molecules in confined geometries, to probe the physics of polymers on a single-chain basis. Interest in

confined DNA is largely shared by two fields of scientific inquiry: biotechnology, where confinement is used to better read genomic information from the molecule, and soft condensed matter physics, where DNA molecules serve as a model system to study polymer physics. A sub-discipline has emerged in its own right dedicated to understanding polymer physics of confined DNA as well as applications of such systems. Most research groups in the field work on both areas, although this thesis is concerned with the physics aspect.

The development of the field is relatively recent: experimentally, appropriate microscopy and microfabrication techniques have only been available since the late 90s or early 2000s [3]. Theoretical models did not progress beyond a heuristic level until the 2010s, when computational algorithms and technology reached the point of simulating experimental conditions with chains comparable in length to the DNA used in experiments [4].

The conformation of a polymer depends on the geometry of its environment [3]. In the bulk, with three free dimensions, polymers will form a random coil with some characteristic size that maximizes entropy. Here, entropy is based on conformational degeneracy: the number of different microscopic configurations the chain can adopt consistent with a given coil size. If a molecule is confined between two parallel plates, in a slit, with a separation less than the characteristic size of the molecule (the radius of gyration), the conformations along the confinement direction are restricted and the molecule spreads out in the two free dimensions, in what is known as quasi-two-dimensional confinement. The equilibrium structure is now a random coil in two dimensions. If the molecule is confined in a narrow tube rather than a slit, in quasi-one-dimensional confinement, there is only the axial degree of freedom and the

molecule extends along the tube axis. Conformational degeneracy is so restricted that there are no fluctuations in shape, only in extended length along the channel. Finally, if a polymer is confined in a cavity smaller than its characteristic size in three dimensions, quasi-zero-dimensional confinement, it simply occupies the confines of the cavity. In the context of DNA as a model polymer, such confinement begins at the radius of gyration of λ-DNA, roughly 700 nanometers, and the three systems of often called nano-slits, nano-channels, and nano-cavities (Figure 1–1).

The behaviour of a polymer chain is governed by various length-scales (Figure 1–2). The total contour length of the chain represents how long it would be if entirely stretched out. For the DNA used in these experiments, that is roughly 16 microns [3]. The persistence length, a manifestation of bending rigidity, represents the scale below which the chain behaves as a rigid rod, which for DNA is roughly 50 nm (in some conventions the Kuhn length, twice the persistence length is used). The effective width represents how close two sections of the chain can be to each other before being mutually repelled. For DNA under physiological buffer conditions, this is typically below 10 nanometers, larger than the double-helix width of two nanometers because of the cloud of counter-ions around it [5]. The overall behaviour of the chain depends on a combination of these length scales, and the average "size" of the polymer's equilibrium structure is given by its radius of gyration. The relevant length-scales of DNA in polymer physics are typically larger than the length-scales associated with the double-helix structure. Base-pairs subtend a contour length of roughly 0.3 nm, the double helix is roughly 2 nm in diameter, and the major grooves along the backbone are separated by roughly 3 nm.

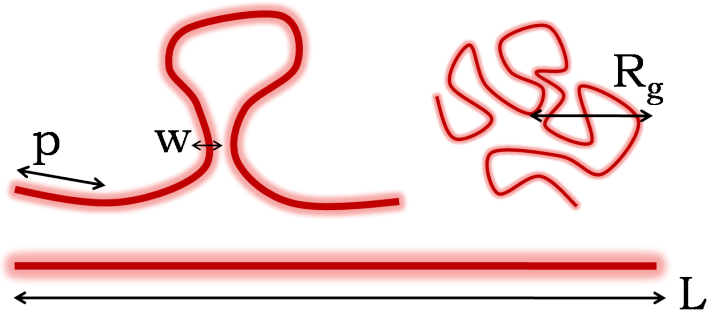

Figure 1–2: Schematic of a polymer highlighting the different length scales: the total contour length L, the persistence length p, the effective width w, and the radius of gyration R_g which depends on all three.

1.2.1 Physical Motivation

A large part of polymer physics focuses on understanding the bulk properties of plastics, gels, and other complex fluids by describing their behaviour on a single-chain level. This can be used, for example, to predict the viscosity of a polymer melt as a function of chain size [6]. Bulk measurements based on scattering or rheometry do not directly address the single-chain level. One particularly powerful concept in bulk polymer physics is the reptation tube model, which posits that a single chain in a polymer melt behaves as if it is confined in a virtual tube defined by entanglements with its neighbours. With traditional synthetic polymers it is difficult to perform experiments on a single-molecule level, and DNA fills this niche quite well. It is monodisperse, as all genomes from a given organism are the same size. It can be stained fluorescently and seen in an optical microscope. It is large enough for its features to be resolved with optical microscopy, but small enough that thermal fluctuations remain the dominant driver of physics. Several theoretical models had been developed

to describe a chain confined in a virtual tube, and by placing a real chain in a real tube, these predictions could be verified on a single-molecule basis.

When a polymer is confined, conformational states that extend beyond the dimensions of the confining geometry are restricted. Reducing the number of accessible states lowers the entropy of the system. Confining a chain may also increase the probability of pairwise collisions between its segments, or cause the chain to bend more than it normally would. The energy between the bulk and the confining geometry due to the change in entropy, excluded volume interactions, and bending rigidity is known as the **free energy of confinement** and is the work required to bring a chain from the bulk into confinement. At equilibrium, a confined chain will orient and partition itself in such a way as to minimize the free energy of confinement. It is a quantity that is sensitive to the underlying polymer physics, and measuring it can help elucidate the different regimes that govern physics at that scale. Measurements have typically focused on examining conformations of confined chains, be it the extension along a nanochannel or the span along a slit, but prior to this work the free energy of confinement has not been directly measured. Numerous controversies still exist that have not been conclusively answered by these studies, including the role of excluded volume under confinement, and the existence of and transitions between various posited scaling regimes. Measurements of the free energy of confinement can clarify these questions.

DNA nanofluidics experiments have largely focused on nanochannels, where the extension is an easily measurable quantity. There has been less work on DNA in slits, with some experiments focusing on diffusion or in-plane size of the molecule. There have been no systematic studies of the confinement

physics of DNA in cavities. Typical experiments use simple uniform geometries such as slits and channels, with the size of the confinement being the only experimental degree of freedom. By combining multiple confinement-scales together on a single device, there are multiple experimental degrees of freedom that can be tuned and the partitioning between different confining regions can be used to measure the free energy of confinement.

Energy is not a quantity that is typically measured directly. In thermal and statistical physics, energy is related to probability through the Boltzmann distribution, where the probability of observing a system in a given state is exponentially disfavoured by the energy of that state. In nanofluidic systems, probability manifests itself in the partitioning of molecular contour between different sized geometries.

In this work, I use a device containing a nanofluidic slit with an embedded lattice of cavities. It allows me to simultaneously probe slit- and cavity-confinement physics, and measure the free energy of confinement by making observations of the partitioning. Through these measurements, I can examine how the free energy of confinement scales between different regimes of slit confinement and measure the strength of excluded volume interactions under confinement, clarifying standing questions in confined polymer physics. I apply this knowledge of the free energy to the dynamics of confined DNA, using it to control the internal fluctuation time-scales and global diffusivity.

1.2.2 Novelty and Importance of this Thesis

This thesis uses a unique experimental technique, in the sense that nobody else uses it, to make measurements that nobody has made before. I demonstrate that a complex nanofluidic device can be used to tune the local free

energy landscape to halt or promote diffusion. I measure for the first time the confinement free energy of DNA in slits and cavities. I show that DNA can be either stably trapped or freely diffusing depending on the confining potential. I demonstrate the reduction of internal molecular fluctuations into controlled harmonic modes. Methods of controlling DNA stability and dynamics on long and short timescales factor into the design of lab-on-a-chip bio-devices.

The results resolve several questions in the field of DNA nanofluidics. One concerns the relevant scaling in the so-called "transition" regime between the Odijk and deGennes limit, which is the subject of some debate [7]. Another is the role excluded volume interactions under confinement and their scaling, which have been of recent theoretical interest [8] but experimental tests have been nearly absent [9]. I also present the first measurements of the effective molecular width in nanofluidic systems and their scaling with ionic strength. Previously, the effective width was only measured in bulk [10], but here it is measured on a single molecule basis. In addition to the experimental results presented, two new theoretical models were developed to help understand them: the full theory of the stretched confined chain [11], and the eigenvalue problem for the semi-flexible chain in a cylinder.

As of the time of this writing, this work has lead to a paper published on diffusion [12], a paper on fluctuations that has been accepted for publication, and a paper on free energy measurements that is currently being peer-reviewed. I am the first author of all three, and a fourth may be written.

1.3 Literature Review

1.3.1 Physical Properties of DNA

The experimental picture of the polymer physics of DNA is not complete. A basic quantity is the Flory exponent, describing the radius of gyration as a function of length, but spectroscopy experiments that attempt to measure the Flory exponent of DNA have not yielded consistent results: Nepal et al. [13], have found consistent ideal scaling (ν=0.52) up to 46 microns, while other experiments by Robertson et al. [14] and Smith et al. [15] find an exponent closer to 0.6 with molecules up to about 100 microns. However, an analysis from Mansfield and Douglas [16] finds that the metric used by those experimentalists does not represent the true size scaling, which upon re-analysis is closer to the ideal value. Some of these differences may be due to different ionic conditions between experiments. The persistence length and effective width of DNA are both dependent on ionic strength. The experimental picture, as summarized by Savelyev [17] is not clear, and many of the experimental results may themselves be based on theoretical assumptions, for example, when fitting to stretching data. It is generally agreed upon to be between 50 and 60 nanometers over several decades of ionic strength, but the behaviour at low ionic strength is still controversial. The persistence length can be considered as the sum of two contributions: the inherent structural rigidity of the molecule, and an electrostatic component that depends on ionic strength. There are two models in the literature describing the electrostatic contribution but disagreeing with each other. The Odijk-Skolnick-Fixman model (OSF) [18] posits that it is inversely proportional to ionic strength (proportional to the square of the Debye length), while the Dobrynin model [19] posits that it is proportional to

the reciprocal square root of ionic strength, or to the Debye length. Interestingly, despite the weaker scaling with ionic strength, the Dobrynin model has a much larger prefactor and thus depends more strongly on ionic strength.

The dependence of the effective molecular width on the ionic strength is discussed by Stigter [5], who considers the screened electrostatic interaction between charged rods (a treatment of non-adjacent anisotropic monomers). The effective width is the distance at which this interaction potential is of order kT. The effective width as predicted by Stigter is slightly larger than the naive prediction of the double helix width (2 nm) plus twice the Debye length, due to the breakdown of the Debye-Huckel approximation near the molecule. The principal experimental investigation of DNA effective width and its scaling with salt was performed by Rybenkov [10], who measured the probability of DNA knot formation before cyclization, as measured by gel electrophoresis. He found that salt-dependent scaling consistent with Stigter's theory. Less exhaustive measurements have been performed by measuring the osmotic pressure exerted by DNA [20] and by light scattering [21]. On a single molecule basis, experiments were lacking before I measured the quantity, as is described in this thesis. More recently, Lee et al. [22] noticed that DNA at very low ionic strengths cannot flow into nanofluidic slits below a certain height, and concluded that the critical height represents the effective width.

Experiments in this field typically use an intercalating dye for fluorescence measurements, but the effect of the YOYO-1 intercalating dye on the persistence length of DNA is also not clear: stretching experiments suggest a slight stiffening [23] while AFM measurements [24] suggest a floppening. It is generally agreed upon that the total contour length increases upon intercalation.

Several experiments have examined different staining ratios of YOYO-1 on DNA in nanofluidics. Persson et al. [25] measured the extension-confinement relationship of DNA in nanochannels at different YOYO-1 concentrations and found a 27 percent increase in extension between the strongest and weakest stains, with very minor differences in the confinement scaling. A similar experiment by Strychalski [7] in slits rather than channels found little effect from different staining ratios, besides increased intensity.

The DNA typically used for polymer physics experiments is the genome of the λ (Lambda) bacteriophage, a virus that infects E. coli. The genome is 48,490 base pairs long making it roughly 16 microns when extended. In the virus, it is coiled inside an icosahedral capsid roughly 60 nanometers in diameter. When the virus attaches to the membrane of a bacterium, the DNA is injected through the tail into the cytoplasm. The other genome typically used in the field is that of the T4 bacteriophage, which is similar but has a genome roughly four times as long. Recently, it was suggested by Tree et al. [26] that this is not sufficiently long to obey asymptotic polymer physics behaviour. Biochemically, λ has sticky ends that allow it to hybridize or cyclize, and precaution must be taken to prevent this. It also has an AT-rich region near its midpoint, which makes it susceptible to photonicking in two.

1.3.2 DNA Nanofluidics: State of the Field

Some of the first studies of DNA in nanochannel confinement were performed by my supervisor Walter Reisner, henceforth referred to as Walter, as a Ph.D. student. An initial paper in PNAS [27] showed that the chain extension was linear with contour length, consistent with one-dimensional Flory

statistics. A later paper in Physical Review Letters made the first set of measurements of the confinement-extension relation [28] which generated a great deal of interest in the field. It was realized that the chain extension was a good metric of the underlying polymer physics, and various experiments attempted to measure it as a function of ionic strength [29], macromolecular crowding [30], and molecular topology [31]. The initial PRL also made measurements of the end-to-end relaxation time, showing a peak near the transition between two scaling regimes, and subsequent research also attempted to make measurements of internal fluctuation time-scales [32], the relaxation time of wavemodes along the chain [33], and to distinguish between similar confinement regimes using fluctuations [34]. Equilibrium nanochannel confinement is at this time generally well understood, and now experiments are turning to non-equilibrium physics: collapsing molecules with AC electric fields [35], compressing them with optically trapped beads [36], and using them as force probes of thermophoretic effects [37].

Theoretically, the extension was traditionally understood in terms of chain deflection in narrow channels and blob-partitioning in large channels, the so-called Odijk [38] and deGennes [39] regimes discussed in greater detail below. However, most experiments took place in channels whose sizes placed the physics between these two regimes. In 2011, Wang et al. [4] developed Monte Carlo simulations to simulate the extension of DNA in nanochannels, a feat previously not computationally possible. They posited an "extended-deGennes regime" in the transition region, in which the blobs become elongated, predicted the same scaling in the extension as the deGennes regime but different scaling in the fluctuations. Other papers attempted to clarify

the properties of this regime [40], examine the interplay between excluded volume and semi-flexibility [41], and examine backfolding in the Odijk regime in greater detail [42]. Although these predictions are often in terms of scaling laws, recently an exact prediction for the extension and fluctuations of a chain in the extended-deGennes regime has been derived, down the prefactor level [43].

DNA nanoconfinement in slits has not been studied to the extent that channel confinement has been. Measurements of the in-plane radius of gyration with respect to height have been made in terms of static properties [7] [44], with limited agreement to the theoretical predictions. Measurements of the diffusion coefficient [45] and relaxation time [46] as a function of slit height have been made to attempt to clarify the role of hydrodynamic interactions under confinement. The most detailed study of hydrodynamic interactions is by Jones et al. [47] who measured intra-chain intensity correlations as a function of spatial separation and found that the correlations decay when the spatial separation exceeds the height of the slit. Lee et al. examined the size-scaling at very low ionic strength to clarify the competing role of electrostatic and confinement effects [22]. One of the most systematic studies of size-scaling in slits as a function of height and ionic strength [48], showing an electrostatic depletion length between the molecule and the wall, was retracted due to improper data analysis and left a bit of a vacuum in the field. In particular, it is still controversial as to whether the molecular span reaches a constant size in sufficiently small slits. Non-equilibrium measurements have also been performed: a group in Taiwan measured the retraction rate of DNA from a slit into a reservoir [49] and a group in Denmark attempted to measure the

filtering of Fourier fluctuation modes due to confinement when the chain is pulled by a optical tweezers [50].

The theoretical developments for slit confinement have been similar, with various simulations [51] and scaling analyses [52] attempting to fill in the gaps between the Odijk and deGennes limits (where the slit height is much smaller than or much larger than the persistence length, respectively), although it is thought that in wide slits the behaviour is dominated by semi-flexibility rather than excluded volume. Recent work by Muralidhar et al. [53] looked at the Odijk regime in slits in greater detail and showed that excluded volume effects in slits are negligible.

Prior to this thesis there have been no systematic explorations of the physics of DNA in nanofluidic cavities. Experiments in similar systems by Walter [1] [2] and myself [12] have examined applications of cavity physics but not the physics themselves. Nykypanchuk and coworkers examined DNA diffusing through spherical cavities connected by pores [54] [55] and saw some of the same quantitative behaviour I observed in my master's thesis. In one experiment [9], he examined the partitioning of DNA between two differently sized spheres, comparing the probability of the molecule occupying the smaller sphere to theoretical predictions with and without excluding volume, and found that excluded volume was relevant.

1.3.3 Applications of Nanofluidics

DNA is more than just a useful model for polymer physics: it also contains our genetic sequence. There is significant technological interest in using nanoconfinement to read the genetic information contained in DNA. In a cell or in the bulk, the genetic sequence is spatially disorganized, and a small step

in space can lead to a totally different part of the genome [56]. Current genetic sequencing technology is limited in its ability to see large-scale structure by the fact that they require many copies of very small segments of DNA to be individually read and stitched together.

When a molecule is stretched out along the axis of a nanochannel, there is a strong correlation between the genetic position along the molecule, and the spatial position along the channel, and several technologies have been developed to use this for large-scale genomic mapping. A simple technique is to attach a sequence specific fluorophore to the DNA, and looking at the spatial distribution of those fluorophores [25] [57]. This technique is now in commercial use, by a company called BioNanoGenomics. A technique developed by Walter involves partially melting stretched DNA [58], allowing the AT bonds to denature while keeping the CG bonds closed. The intercalating dye from the AT regions leaves the molecule, leaving a "barcode" of the AT- and CG-rich regions of the genome. This was used by Rob Welch in his master's thesis to make a large-scale map of the yeast genome [59]. While this technique has a higher information density than site-fluorophore mapping, its resolution is still diffraction limited to hundreds or thousands of base-pairs. Nanochannel mapping techniques are useful for large-scale structural information, for example determining if one chromosomal segment has been transplanted to another site, as occurs in certain cancers, and also for rapid identification of strains, for example to distinguish between regular and antibiotic-resistant bacteria in a hospital setting [3]. These techniques cannot read the genetic sequence. Similar techniques takes advantage of slit rather than channel confinement [60] [61] but operate on generally the same principles.

Recently, technologies have been developed based on DNA confined in small cavities that act as zero-mode waveguides [62]. The cavities are not meant to specifically confine the DNA, but they provide an evanescent optical field that can excite single fluorphores on the molecule as it binds to sites in the cavity, allowing the fluorophores to be read one at a time. Such devices, developed by Pacific Biosciences, are now in commercial use [63].

An area that has received a large amount of interest is nanopore sequencing [64]. A nanopore is a very small hole with a diameter typically of ten nanometers. As an ionic fluid flows through the pore under a voltage bias, the electric current can be measured, and if a DNA molecule goes through the pore, it blocks the flow of ions, causing a small dip in the measured current. If this can be measured precisely enough, the blockage caused by each individual base pair may be detected, allowing the sequence to be reconstructed. The basic nanopore setup is fundamentally limited in sensitivity because both the signal and the noise are fundamentally linked to the rate at which the voltage bias drives fluid and DNA through the pore. There are other proposed methods to overcome this, including measuring a transverse tunnelling current across the pore (rather than through it) [65], or controlling the flow of DNA through other nanofluidic mechanisms [66]. One company (Oxford Nanopore) claims to have developed a working nanopore sequencer, but results are limited [67]. Independently of their use in biotechnology, a large body of theoretical and computational work has been developed to describe the polymer physics of these systems [68]. This thesis concerns the equilibrium properties of DNA, and nanopores are a decidedly non-equilibrium system.

A biological connection to this field is the packaging of genetic material in cells and capsids. A human cell contains several meters of DNA compressed into a few microns. The DNA of 100 people would stretch to a length of a light-year. The study of how this much DNA is packaged into such a small volume is of interest to cell biology. In viral capsids, DNA is arranged more like a liquid crystal than a polymer solution [69] and it has been proposed that the process of viral DNA ejection is determined entirely by its free energy of confinement [70]. In mammalian cells, the complex network of proteins that compactify DNA contribute to the organization of the nucleus. In bacteria, however, the confinement of the chromosome is most similar to DNA in nanofluidic systems. There has been research studying compactification by cellular proteins, both experimental [71] and theoretical [72], the segregation of bacterial chromosomes during cell division has been discussed in the context of polymer mixing in nanochannel confinement [73]. This may suggest a very fundamental statement: the first cells divided simply in order to increase entropy.

1.4 Theory of Polymer Physics

This section covers the basic models of polymer physics and the analytical tools that are used to develop to them. Theory as it directly pertains to my experimental system, as well as new theoretical models developed for this thesis, will be discussed elsewhere.

1.4.1 Polymer Models

The simplest model of a polymer is the *ideal chain* (Figure 1–3). A polymer of total contour length L can follow a random walk through space with steps of length b, called the *Kuhn length*, representing an intrinsic monomer

size. There is no correlation in orientational order along the chain, and the ideal chain can cross itself such that two segments occupy the same point in space. There are many different conformations a chain of a given length can occupy, but the conformations that leave the chain in an extended state are relatively rare, as well as are extremely compact conformations. The entropy of the chain arises from the degeneracy of conformational states for a given macroscopic size. If the two ends of the chain are held fixed, the entropy of the chain arises from the degeneracy of conformations that yield the same end-to-end distance. When the chain is maximally stretched there is only one microscopic state and entropy is minimal, while when the ends are closer together it can be re-oriented many ways maintaining that distance, thus the higher entropy state is one where the ends are closer together. In contact with a thermal reservoir, the chain will sample many possible configurations and is likely to be found in one with high conformational degeneracy

Considering the distance between the two ends, because both ends fluctuate and sample many configurations, the average separation will be zero, much like how the average distance covered by an ensemble of random walks is zero. However, the mean-squared end-to-end distance, much like the mean-squared displacement of a random walk, is nonzero. The mean vector displacement from a segment of the chain to the centre of mass is zero, but the root-mean-square distance from the centre of mass, called the *radius of gyration*, is nonzero, and represents the characteristic size of the molecule. For the ideal chain in three dimensions, the radius of gyration scales as the square root of the contour length, because the mean-square displacement scales as the contour length.

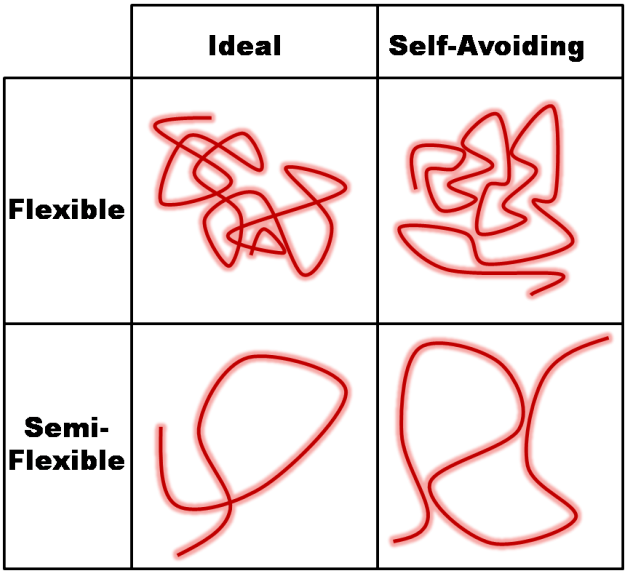

Figure 1–3: Table of different classes of polymers, depending on whether excluded volume and semi-flexibility are taken into account.

$$R_g^{ideal} = b\sqrt{\frac{L}{6b}} \approx L^{\frac{1}{2}} \tag{1.1}$$

Realistically, no two segments of a chain can occupy the same point in space at the same time. This is known as *self-exclusion* or the *excluded volume interaction*. The simplest proscription of this interaction is that of hard-spheres, while Lennard-Jones repulsion or screened electrostatic interactions may be more realistic [74]. A random walk that is forbidden from re-visiting an already accessed location is called a self-avoiding walk, and is mathematically equivalent to an Ising model with zero spin degrees of freedom. Because a self-avoiding walk is less compact than a true random walk, a polymer that experiences self-exclusion is called a *swollen chain*. Making an analogy between an ideal chain and an ideal gas, the swollen chain is to the ideal chain as the van der Waals gas is to the ideal gas. The fact that a self-avoiding walk cannot

visit the same site twice means that a swollen chain has a radius of gyration larger than that of an ideal chain with the same contour length: its gyration radius has a characteristic growth exponent closer to 3/5 than to 1/2. (more detailed calculations put it closer to 0.588 [26]). This is often called the *Flory exponent* after Paul Flory and is important for dictating polymer behaviour.

$$R_g^{swole} = b\left(\frac{L}{b}\right)^{\frac{3}{5}} \approx L^{0.6} \tag{1.2}$$

The classical Flory exponent in D dimensions is $\frac{3}{D+2}$: 0.6 in 3D, 0.75 in 2D, and 1 in 1D.

While polymer chains lack long-range orientational order along the chain, there is a length-scale over which the chain orientation is correlated. *Semi-flexibility* describes behaviour where the polymer behaves as a rigid rod over short length scales and performs a random-walk over long length scales. The *persistence length* is defined as the exponential decay length of tangent-tangent correlations along the chain in the bulk, and is equal to the bending rigidity of the chain.

$$\langle \cos\theta(s) \cdot \cos\theta(s+\Delta s)\rangle = e^{-\frac{\Delta s}{p}} \tag{1.3}$$

The theoretical model of the semi-flexible polymer is called the worm-like chain (WLC) or Krotky-Porod model [75]. It describes the end-to-end distance and radius of gyration of the chain that interpolates between two limits.

$$R_{WLC}^2 = 2pL\left(1 - \frac{p}{L}\left(1 - e^{-L/p}\right)\right) \tag{1.4}$$

When the contour length is much shorter than the persistence length, it is essentially a rod and the radius of gyration grows with length. When it is much longer than the persistence length, the chain behaves like a random coil, with $b = 2p$. The Kuhn length is thus physically the step-size of the random walk that describes the semi-flexible polymer conformation in the limit where L≫p. DNA behaves as a semi-flexible chain with excluded volume interactions. It has an effective width between 5 and 20 nanometers, a persistence length between 50 and 80 nanometers (both depend on buffer conditions), and a contour length (for the λ-DNA used in experiments) of roughly 300 times its persistence length. There is no simple analytic theory for a semi-flexible, excluded volume chain, and the different interactions can interfere with each other (for example, two segments on a rigid chain would not interact with each other through excluded volume as they otherwise would, if the chain cannot bend enough to get them close to each other). Several textbooks exist providing more thorough summaries of polymer physics, including Rubinstein and Colby [76].

1.4.2 Scaling Laws, Blob Models and Flory Theory

Many predictions in polymer physics are not in terms of exact equations but rather through *scaling laws* describing how one quantity changes with variations in another. These are often expressed in terms of power laws, where an exponent dictates the relationship. For example, in the previous subsection it was shown that the relationship between radius of gyration and contour length is $R_g \approx L^{0.5}$ for an ideal chain and $R_g \approx L^{0.6}$ for a swollen chain. Working in terms of scaling laws and exponents is useful for working out complex theoretical predictions without worrying about individual constants or small effects

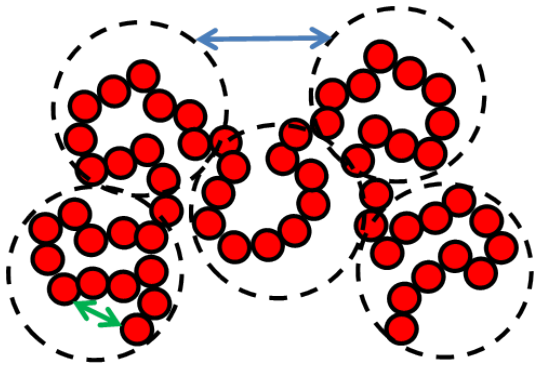

Figure 1–4: Schematic of a chain partitioned into blobs. Within the blob length-scale, individual monomer interactions are considered, but at larger length-scales interactions between the blobs are considered.

that would not change the scaling. Experiments often plot data on log-log axes to compare the measurements to a known power scaling prediction.

A powerful concept used to derive scaling relations in polymer physics is that of the blob (Figure 1–4). A blob is a small region of space containing part of the polymer, over which the polymer experiences equilibrium bulk physics, and the physics over larger length scales can be treated as interactions between these blobs. In the bulk, the blob length scale is typically the length scale below which the chain does not interact with itself, thus within the blob the chain obeys ideal statistics while over larger length scales the polymer can be treated as a swollen chain of these blobs, and the average number of collisions per blob is one. A subtlety in blob theory is that because the blobs are in thermal and mechanical equilibrium with each other, each must have an energy of order kT.

Under confinement, the blob length scale is typically the dimension of confinement, the length-scale below which the chain will not interact with the confining walls. The chain statistics within the blob are those of the

bulk geometry, be it ideal or swollen, while the chain statistics between the blobs are those of the reduced dimensionality. This can be used to derive some fundamental scaling relations, for example the confinement-extension relation of a chain in a nanochannel. If the chain is partitioned into spherical blobs with the same diameter as the channel, within the blob the chain obeys statistics such that the contour length per blob scales according to the 3D Flory exponent. Between the blobs, the chain can be treated as a string of excluded-volume spheres obeying 1D Flory statistics. The total extension of the chain is simply the diameter of the blobs (same as the channel, D) times the number of blobs, which is the total contour length (L) divided by the contour per blob g, known from the in-blob statistics that $D \approx g^{0.6}$ implying $g \approx D^{1/0.6}$. Because L is independent of D, the scaling of the chain extension with respect to D is just D over g, scaling as $D^{1-1/0.6} = D^{-2/3}$. This is an experimental prediction that was derived without knowing anything about the properties of the chain or its interaction with the walls, only using blob analysis.

An alternative derivation of the extension of DNA in a nanochannel comes from what is known as Flory theory, where the total free energy is written as the sum of entropic and excluded volume considerations. The entropic component is a harmonic and the excluded volume component is proportional to the ratio of the square of contour length to the volume of the channel segment that contains the confined chain. The equilibrium extension scaling (ignoring order-unity prefactors) can be found by minimizing the energy:

$$\frac{F_{Flory}}{kT} = \frac{R^2}{bL} + \frac{bL^2}{D^2R} \rightarrow \frac{dF}{dR} = 0 = \frac{2R}{bL} - \frac{bL^2}{D^2R} \rightarrow R_{eq} \approx LD^{-2/3} \qquad (1.5)$$

This gives the same scaling for the chain extension as blob theory. However, expanding the free energy about equilibrium gives a $D^{-4/3}$ scaling, while the blob argument gives $D^{-5/3}$. This contradiction, two derivations predicting the same size scaling but different energy scalings, can be resolved by rewriting a blob model that allows anisotropic blobs with ideal in-blob statistics, with an additional constraint that the extension within the blob is such that it would have the same length assuming both ideal and swollen statistics. This gives us two regimes: the deGennes regime described by spherical blobs with self-avoiding statistics, and the so-called Extended deGennes regime described by ellipsoidal blobs with ideal statistics [3]. Both of these regimes are invoked to describe nanoconfined DNA: the Extended deGennes regime describes semi-flexible chains confined in geometries too narrow for spherical blobs to form (roughly 100 nm to 500 nm wide channels), while the deGennes regime describes wider channels.

Blob and Flory arguments are useful for deriving scaling relations from a small number of assumptions with fairly simple algebra. They are limited in their precision: the prefactors of the scaling arguments cannot be derived with blob logic, which require either a more rigorous field theory or detailed numerical simulations. Another limitation of blob and scaling arguments in general is that they apply in the limit of infinitely long chains, but the DNA molecules used in a typical experiment may be too short to obey this universal behaviour. For example, even though a DNA molecule has excluded volume interactions between different segments of the chain, if the chain is not long enough, it is unlikely for different segments to interact with each other and it will behave like an ideal chain.

1.4.3 Field Theory

More precise models describing confined chains can be developed from polymer field theory. The distribution of the contour concentration of an ensemble of chains is equivalent to the probability of a brownian particle visiting a specific location, which is governed by the diffusion equation. The ground state solution of the diffusion equation for a given set of boundary conditions is a monomer concentration profile [77]. The differential equation can be made more complex to incorporate semi-flexibility through the wormlike diffusion equation [8] or excluded volume by adding nonlinearity to the PDE [78]. Because these equations do not often have closed-form solutions, self-consistent field theory (SCFT) is often used, where a solution is guessed and iterated towards. Polymer field theory is more precise in its predictions than blob scaling, and recently has been used to derive prefactors as well as scalings for the nanochannel problem [43].

The simplest differential equation for the polymer concentration field is the diffusion equation, which is equivalent to the time-independent Schroedinger equation with a real solution Ψ representing the probability of finding a monomer at a given location:

$$\left[-\frac{b^2}{6}\nabla^2 + V\right]\Psi = E\Psi \tag{1.6}$$

Here, E is the energy eigenvalue of the problem and V is some external potential. Solving this equation with an appropriate potential and boundary conditions can yield the density profile Ψ^2 and the free energy of confinement.

1.4.4 Numerical Simulations

The macroscopic behaviour of polymers can be studied by simulating their microscopic behaviour, through numerical simulations. If blob arguments and field theory represent a "top-down" approach to understanding polymers, numerical simulations represent the "bottom-up." By simulating large ensembles of chains, the expected behaviour can be determined. Chains are often represented as spherical beads connected by springs. In addition to the nearest-neighbour spring interactions, the beads can interact through excluded volume (for example a Lennard-Jones repulsion between non-adjacent beads) and semi-flexibility can be imposed with a bending potential, allowing simulations of a semi-flexbile excluded volume chain where theory is lacking. The chains can be simulated through Monte Carlo sampling, where the system evolves through perturbations with a Boltzmann-weighted probability, or through molecular dynamics, where the chain evolves over time through Newton's laws of motion, with stochastic thermal noise and an effective viscosity.

To calculate the extension of a chain in a tube, similar to the previous blob section, an ensemble of chains would have to be simulated inside tubes of different sizes and their mean extensions recorded and averaged. A long-standing challenge is the simulation of long polymer chains, long enough to be experimentally relevant and to display universality. Simulations of longer chains are more computationally intensive and risk having much lower sampling compared to short chains. In recent years, computer technology and the development of algorithms have allowed simulations with chains long enough to be experimentally and theoretically relevant. The "modern era" of numerical simulation in this field can be traced to the paper of Wang, Tree, and

Dorfman in 2011 who simulated the extension of DNA in nanochannels and obtained good agreement to experiment [4].

1.4.5 The Free Energy of Confinement of an Ideal Chain in a Slit: A comparison of three methods.

As discussed previously, the free energy of confinement is the work that is required to bring a polymer chain from the bulk into a confining geometry. It arises due to the loss of entropy under confinement, and contributions of excluded volume and bending energy as segments of the chain are brought into closer proximity. Here, the free energy of confinement of an ideal chain in a slit is derived according to the three discussed methods, as an example of how they can be used to generate experimental predictions.

Blob argument. Consider an ideal chain in a slit of height h, dividing the chain into a series of connected blobs with length-scale h (Figure 1–5). Within each blob, a given monomer does not feel the effects of confinement, and obeys bulk statistics, which we declare to be ideal. Thus, the contour length is related to the blob length scale through the relation $bg^{\nu} = h$, where we take the Flory exponent ν to be $1/2$, b is the monomer size and g is the number of monomers per blob. Because the blobs are in thermal equilibrium with each other and do not interpenetrate, each one contributes a free energy kT, and the total energy is $F = GkT$ where G is the total number of blobs. The number of blobs is the total number of monomers L/b divided by the number of monomers per blob, $G = L/(bg)$. From the ideal scaling we have $g = (h/b)^{1/\nu}$ and $G = (L/b)bh^{-1/\nu}$. With ideal statistics, the free energy of confinement is $F = kTLbh^{-2}$, which is equivalent to the exact expression to within a prefactor.

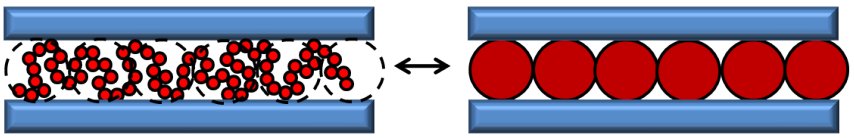

Figure 1–5: A blob picture of a confined chain.

Numerical simulation. I generated random walks on a square grid with 2000 steps (Figure 1–6). A "slit height" was chosen, and it was observed whether a given walk exceeded the bounds of the slit or not. The proportion of walks that satisfied the confinement conditions was measured as a function of height. The probability of finding a chain in a confined region is equivalent to its Boltzmann-weighted free energy of confinement, thus the free energy of confinement can be calculated from the logarithm of the proportion of chains satisfying the confinement conditions. By performing a power law fit to this data, the scaling of the free energy of confinement can be measured. From these rudimentary simulations, we find a power-law scaling of -2.2 ± 0.3, consistent with the ideal blob argument. The prefactor for an inverse-square scaling describing this data is approximately 2000, the length of the chain, matching the blob model for b=1. With greater time devoted to computation, the precision can be improved.

Exact solution. The exact solution is ultimately arrived at by finding the probability of a monomer being found at a specific location, which is a form of the diffusion equation in an external potential. In the case of an ideal chain in a slit, the potential is zero within the slit, infinite elsewhere, and has boundary conditions such that the probability of finding a monomer on a wall is zero. This leads to an ordinary differential equation that is the same

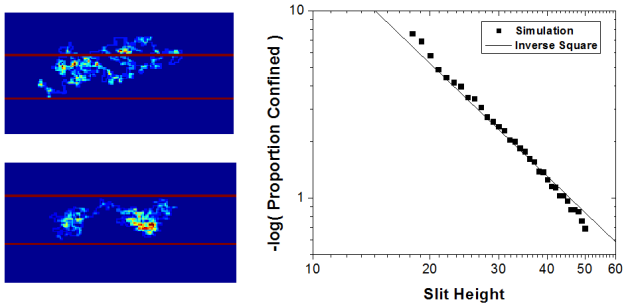

Figure 1–6: A simple numerical model I developed to compute the free energy of confined chains. Random walks are generated, and the fraction satisfying the confinement conditions is measured. The free energy of confinement is the logarithm of the probability of finding a confined chain.

as the quantum particle in an infinite square well. The ground state energy eigenvalue of this system is

$$F = kT\frac{\pi^2}{6}\frac{Lb}{h^2} \tag{1.7}$$

This again matches the predicted scaling of the blob model as well as the numerical simulations, but solving the problem exactly allows a measurement of the prefactor, approximately 1.64.

1.4.6 More Complete Models of Slit-Confined Polymers

The above derivations apply to a freely jointed ideal chain, which may approximate DNA in a slit much larger than its persistence length. When the confinement is much smaller than the persistence length, the conformational states leading to the classic spherical blobs are surpressed by bending rigidity. A more realistic description of the chain involves deflection back and forth between the walls, and this is known as the Odijk regime after Theo Odijk (Figure 1–7). Rather than being re-normalized into blobs, the chain can be divided into these deflection segments, and in nanochannels the extension in

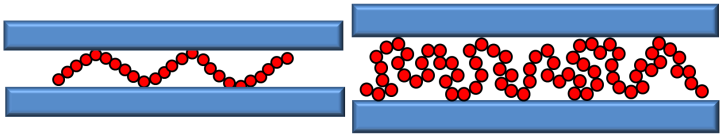

Figure 1–7: Schematic of the Odijk (left) and deGennes (right) regimes. In the Odijk regime, the chain deflects between the walls, in the deGennes regime the molecule is partitioned into blobs inside which the monomers do not feel confined.

this regime can be calculated just by considering the length of each segment, $(ph^2)^{1/3}$ and the number of segments per chain. The free energy of confinement is characterized with a similar kT-per-partition argument, with a known numeric prefactor:

$$\frac{\Delta F}{kT} = \frac{1.104}{(ph^2)^{\frac{1}{3}}} L \tag{1.8}$$

The blob picture for an ideal chain in a slit was described previously, and the exact value of its free energy of confinement in equation 1.7 and is proportional to the inverse square of height. I refer to this as the Ideal regime; it can also be referred to as the Gauss-deGennes regime. There is also a regime characterized by blobs obeying swollen statistics, known as the deGennes or Flory-deGennes regime, which is characterized by a $h^{-5/3}$ scaling in the free energy. However, this is thought to apply more to nanochannels than to slits [53].

The Odijk and Ideal regimes apply when the slit height is much less than or much greater than the persistence length. Most experiments in this field, however, take place in systems whose confining length-scale is on the order of a few persistence lengths, where neither limiting case applies. Although an exact expression cannot be derived, the free energy of confinement for a

semi-flexible chain in a slit can be found using polymer field theory. Jeff Chen (JC), at the University of Waterloo, along with co-worker Sullivan, solved a modified diffusion equation representing the probability distribution of a worm-like chain, with the boundary conditions of slit-like confinement [79]. The energy eigenvalue of those numerical solutions is the free energy of confinement per Kuhn length at that height. By solving the equation at heights in between the Odijk and Ideal limits, they were able to find a smooth function that describes the free energy of confinement at all heights. Similar interpolations were found by Smyda and Harvey [80] and the Dorfman group [53]. The interpolating expression is:

$$\frac{\Delta F}{kT} = \frac{\pi^2}{6} \frac{\frac{2p}{h^2}}{\left(1.2865\left(\frac{2p}{h}\right)^2 + 0.992\left(\frac{2p}{h}\right) + 1\right)^{\frac{2}{3}}} L \tag{1.9}$$

As can be seen in Figure 1–8, in the region of parameter space where experiments typically take place, neither limiting regime's prediction as accurate, differing by as much as 1 kT per Kuhn segment. This demonstrates the necessity of having a more complex theoretical model than a simple power scaling argument. DNA may never be able to enter the "true" Odijk regime if it requires slits to be smaller than its effective width, and the DNA typically used in experiments, λ, is too small to be confined in the "true" Ideal regime.

1.4.7 Confinement in Cavities

Confinement in cavities is different from slits and channels because there is only one possible macroscopic state: the chain filling the cavity. For a chain in a channel, as more contour is added, the chain can just move farther down the channel to avoid excess energy from excluded volume and bending. When

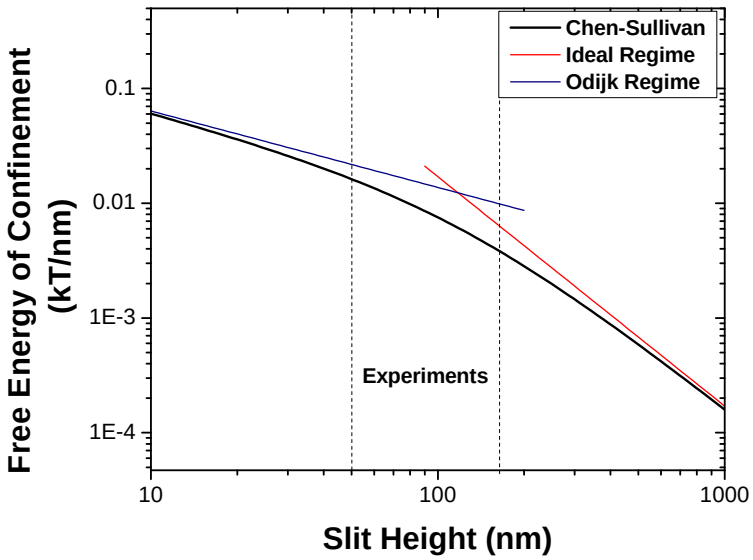

Figure 1–8: The free energy of confinement per unit length for a semi-flexible polymer confined in a slit, as a function of the slit height, using the persistence length of DNA (p=52 nm). The Chen-Sullivan curve [79] describes the entire range of heights, while the Odijk and Ideal regimes describe very narrow and very wide slits, respectively. Experiments in this thesis cover an intermediate range where neither fully applies.

a chain is in a cavity, and more contour is added, the chain cannot reconfigure itself in the same way, and the concentration and bending angles increase. Thus, the free energy of confinement in cavities is not purely entropic but has contributions from excluded volume and bending rigidity, which do not necessarily scale linearly with contour length.

The simplest extension of the slit and cavity analysis is to consider the ideal chain in a box, where the only contributor to the free energy is the loss of entropy. This has the same inverse-square scaling in the free energy with the length-scale of the box, but a higher prefactor than for the slit or channel. Recently, Chen has solved the wormlike diffusion equation in spherical geometries to incorporate semi-flexibility and study an analogue of the Odijk regime where the chain develops nematic order, and bending rigidity rather than entropy is the main contributor to the free energy. Interestingly, the free energy follows the same scaling laws in both regimes with different prefactors [8].

The most complete description of cavity-confined polymer physics is by Takahiro Sakaue [78]. He describes the free energy of confinement of an excluded volume semi-flexible chain in a spherical cavity, as a function of the length of the chain and volume of the cavity V. The calculations are based on a combination of self-consistent field theory and blob arguments. He describes five different regimes depending on the ratio of the different length-scales. There are regimes characterized by strong bending and liquid crystalline order which are not very relevant to nanofluidics and were discussed by Chen.

For the largest spheres in the phase diagram, there is a regime characterized by a bulk-like packing of blobs obeying swollen statistics, and if

the monomer concentration is increased by decreasing the cavity volume (or adding contour), the mean field regime is entered. In the mean field regime, the concentration is roughly uniform through the cavities and the free energy is dominated by pairwise segment interactions. This justifies truncating the virial expansion of the energy at the second coefficient, giving a free energy that scales quadratically with contour length. The entropic loss due to confinement in this regime may be treated as a surface term, contributing to the linear coefficient. Within this regime, the free energy of confinement due to excluded volume is:

$$\frac{\Delta F_{cavity}}{kT} = \frac{\pi}{4}\frac{w}{V}L^2 \tag{1.10}$$

An analogy can be made to a quantum particle in a box, which is mathematically equivalent to an ideal chain in a box. If there is a single electron in an infinite square well, in its ground state its probability amplitude is sinusoidal and the expectation value of the electron's position is in the centre of the box. For an ideal chain in a box, the analogy to the wavefunction is a density field that when squared gives the local concentration. The interpretation of the sinusoidal ground state is that the monomer concentration is highest in the centre of the box, and it falls off towards the edges. If multiple repelling electrons are in a box together (ignoring Fermi statistics), it is less likely to find an overdensity of electrons in the centre, and the wavefunction will be flatter as the electrons minimize their repulsion energy. There will still be a fall-off in the wavefunction towards the walls, which is no longer sinusoidal [81] and becomes tanh-like. With an excluded volume chain, the concentration

will redistribute from the ideal case to minimize the excess energy, which will result in a more uniform density profile: the mean field.

1.4.8 Entropic Elasticity

If the end-to-end separation, R_{ee}, is treated as the macroscopic state of a chain, and the highest-degeneracy state is one with the ends close together, when the ends of a chain are stretched and released the system will evolve into a higher entropy state with the ends closer together. This is known as entropic elasticity, and the force that resists pulling the ends of a chain apart is an entropic force. The simplest model of a polymer, the freely jointed ideal chain, has a harmonic elasticity. This can be seen by considering that the probability of a certain end-to-end separation is Gaussian with that separation, and the probability is also related to the energy through the Boltzmann distribution, implying that the energy is quadratic with separation.

The entropic force f is often written in terms of the dimensionless relative extension $x \equiv R_{ee}/L$. For an ideal chain the force is:

$$f = kT\frac{3}{2p}x \tag{1.11}$$

A similar argument can be made for an excluded volume chain, but typically is not. In the high-tension limit, the force response is characterized by a reduction in transverse fluctuation modes rather than a loss of conformational states. The force-extension relationship for a semi-flexible chain interpolates between the low-tension and high-tension limit, and is given by the so-called Marko-Siggia force law:

$$f = \frac{kT}{p}\left(x + \frac{1}{4\left(1-x\right)^2} - \frac{1}{4}\right) \tag{1.12}$$

This was tested experimentally by attaching DNA to optically stretched beads and stretching the molecules, using the beads as force probes [82]. The equation describes the force-extension relationship well, before the overstretching transition occurs and the same physics no longer applies.

Typically, confinement and elasticity are not discussed together. When a chain is confined, the correlation-decay length is effectively increased above the bulk persistence length by the correlations imposed by the walls. In addition, transverse oscillation modes that contribute to the elasticity are restricted. Chen et al. [83] (not Jeff Chen) performed numerical simulations of a stretched chain in a slit and developed a modified Marko-Siggia relation based on an effective persistence and a nonzero equilibrium extension, but this model broke down at low tension. I spoke with Hendrick de Haan (HdH), formerly a postdoc at the University of Ottawa and now a professor at the University of Ontario, who over the years developed a full parameterization of the stretched confined chain.

CHAPTER 2
Experiments and Model

2.1 Experimental System

In contrast to the featureless slits and channels found in most nanofluidics experiments, the system used in this work is a hybrid device consisting of a quasi-two-dimensional nanofluidic slit embedded with a lattice of cavities (Figure 2–1). The slits are between 50 and 200 nanometers in height. The cavities, square pits etched in the floor of the slit, are twice as deep as the slit, several hundred nanometers wide, and separated by about a micron. The pits offer greater conformational degeneracy than the confining slit and act as entropic traps. A molecule can partition some of its contour in the slit to increase entropy, but increasing the local concentration in the cavity gives rise to excluded volume interactions, eventually driving contour back into the slit. To balance entropy disfavouring the slit and the excluded volume disfavouring the cavities, the molecule will occupy a discrete number of these pits, typically between one and four for λ-DNA (Figure 2–2). A molecule will diffuse through its environment by undergoing transitions between these different occupancy states. The number of pits a molecule occupies is based on a balance of three factors: entropy, excluded volume, and the entropic elasticity in the strand linking each adjacent pair of occupied pits. By examining how a molecule partitions itself into different geometries, the energetic factors leading to that partitioning can be measured.

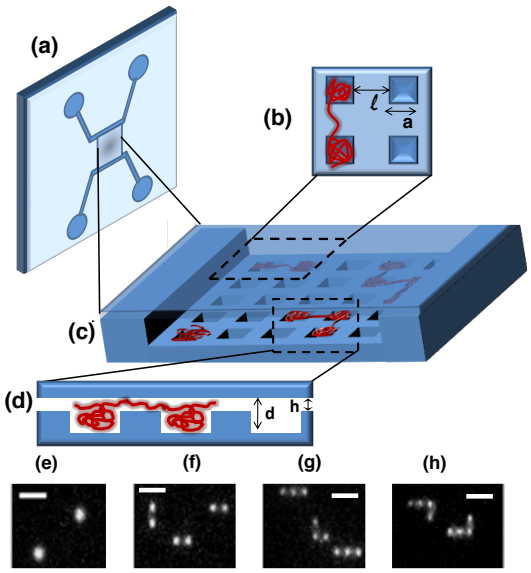

Figure 2–1: Schematic of the chip devices used in these experiments. (a) Overall organization of the chip showing the microfluidic reservoirs, nanofluidic slits, and nanopit arrays. (b) A top-view of a molecule occupying two pits. (c) An oblique view of molecules in various configurations. (d) A side-view of a molecule occupying two pits. (e)-(h) Fluorescence micrographs of molecules in 1, 2, 3, and 4 pits. Scale bar is two microns.

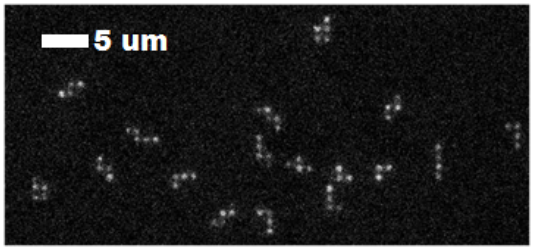

Figure 2–2: A typical fluorescence micrograph of an ensemble of λ-DNA molecules occupying beteen 3 and 5 pits.

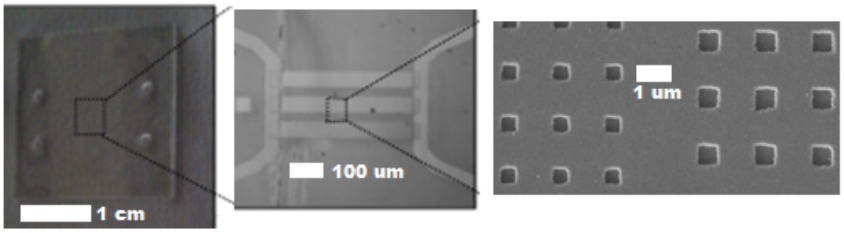

Figure 2–3: Left. Photograph of one of the devices. Middle. An optical micrograph of the chip centre; the three nanoslits are seen in between the microfluidic reservoirs. Right. An electron micrograph of two of the nanopit geometries in one of the slits.

2.1.1 Layout and Parameters

The lab-on-a-chip devices (Figure 2–3) consist of three to five nanofluidic slits, which are 50-80 microns wide and 500 microns long, each etched to the same height. Each slit is partitioned into different regions containing a unique nanopit lattice, with some combination of pit width and spacing. In some devices, each slit contains a common lattice spacing which is then divided into several different pit sizes. In other devices, the pit sizes in each slit are fixed while the spacing between them varies. Older devices typically have five to eight geometries per slit (up to 24 per chip), while newer designs have 30 geometries per slit (up to 90 per chip). Each combination of geometric parameters represents unique experimental conditions. At either ends of the slits, there are microfluidic reservoirs (roughly a micron deep and 50 microns wide) connecting the nanofluidic slit to macroscopic entry holes.

The slit heights (h) used are between 50 and 200 nanometers, meaning the cavity depths (d) are roughly between 100 and 400 nm. By design the depth is twice the height, but difficulties in maintaining a consistent etch rate in fabrication lead to variations in this ratio, in the worst-case of 10 %. The

smallest pit widths (a) are 200 nanometers wide and the largest are 1000 nanometers. The lattice spacings (ℓ) are at least 500 nanometers and the widest are spaced by five microns, although 2 microns is rarely exceeded.

With very few exceptions, λ-DNA was used for our experiments, stained with YOYO-1 in a 10:1 base-pair:dye ratio, which is known to extend the contour length by roughly 15 %. A Tris buffer was used, with 50 mM concentration at pH 8, although the concentration was varied in a few experiments from 3 to 100 mM. The ionic strength of the buffer is the concentration of dissociated ions in solution, calculated through chemical equilibrium conditions. At the pKa of Tris (8), half the ions dissociate and the ionic strength of the Tris buffer is half the nominal concentration. Beta-mercaptoethanol (BME) was used as an anti-bleaching agent. Experiments were not temperature controlled but "room temperature" was roughly 25 Celsius.

Table 2–1: Table of experimental physical parameters

Symbol	Meaning	Typical Value
N	Number of occupied pits	2
L	Total contour length	19 microns
p	Persistence length	52 nm
w	Effective width	9 nm
a	Cavity width	500 nm
ℓ	Lattice spacing	1000 nm
h	Slit height	100 nm
d	Cavity depth	200 nm
kT	Thermal energy	25 meV
I	Ionic strength	50 mM

2.1.2 Relevant Literature

The nanopit-nanoslit system was developed by Walter and originally used to demonstrate directed assembly of molecules using entropic forces [1]. Subsequently, the mobility of DNA driven through such a system was analyzed [2].

There have been some similar experiments that have not captured the same physics. Jongyoon Han's group uses an array of grooves in a nanofluidic slit to separate molecules by size, but typically each groove is larger than the DNA radius of gyration and contains many molecules [84]. Yeh et al. [49] observed large DNA molecules extended over a slit between two reservoirs, as the entropic forces in the reservoir play a "tug of war" with the molecule until it falls into a single reservoir. Kounovsky-Schafer et al. [60] extended this analysis to examine hydrodynamic interactions in long DNA molecules extended across a slit between two reservoirs, measuring the global translocation time. In the experiments of Yeh and Kounovsky-Schafer, the molecule is in the equilibrium state in a single reservoir, and there are no relevant excluded volume interactions that drive the molecule into higher-order states. Nykypanchuk used an array of nanofluidic cavities, an inverse opal crystal of spheres connected by pores, to show the molecule undergoing transitions between different pores [54]. In these experiments, higher occupancy states were studied and there are hints of some of similar phenomena, such as stability-damped diffusion, that I later observed.

2.2 Experimental Setup and Procedures

2.2.1 Device Design and Fabrication

The devices were made in four-inch fused silica wafers. The pit features were patterned with electron beam lithography in ZEP resist and etched using reactive ion etching (RIE). Slit and microchannel features were patterned using UV photolithography and etched using RIE. Wafers were diced into nine chips using a diamond saw, and were bonded to cover slips using an RCA cleaning process. The fabricated devices were compared to the design specifications using scanning electron microscopy.

The RIE protocol was designed with a specific etch rate of approximately 40-50 nanometers per minute. However, the outcome of etching was often different than expected from this nominal rate. To attempt to stabilize this, the RIE was run with a wafer covered only in photoresist, after which a dummy wafer was etched so that the etch rate could be calibrated. Despite this, there was difficulty getting the depth of the pits and of the slit to be the same, in chips fabricated at McGill. This was not as much of an issue for chips fabricated in Denmark. The etch depths of the microchannel reservoirs, the nanoslits, and the pits were measured using a scanning profilometer. A large alignment marker used to measure the depth of the e-beam stage etch.

Two small changes were made to the post-lithography processes over the past few years. One involves the sandplasting process, which entails affixing each chip to a metal mask using melted wax, and driving sand through the mask to make reservoir holes in the chip. Previously, the side of the chip with the features ("top") was positioned facing away from the mask and the bottom was affixed to the max with melted wax. A layer of photoresist was

applied to the top to protect the features from sand, and it was covered in plastic tape. Holes were poked in the tape to allow the sand through. A common pitfall was that the sand would collect between the tape and the chip, scratching the surface and making it very difficult to bond. To prevent this, we started waxing the top of the chip to the mask, using the wax and the metal to protect it from the sand. The other change involved removing superfluous steps from the bonding process. Initially, a piranha solution was used to clean the chips for ten minutes, before performing an RCA2 and RCA1 process (the numbers are in reverse order). Each involves heating a litre of fluid to 70 degrees with a hotplate and keeping it at that temperature for 20 minutes. The RCA processes add about 90 minutes to the bonding process. It was realized that these processes were superfluous, and that merely cleaning the chips in piranha for 20 minutes is sufficient to attain the van der Waals bonding between the two chips with similar success.

2.2.2 DNA and Buffer Chemistry

DNA molecules were stained with YOYO-1 fluorescent dye (a dimer of Yellow Oxazole) with a staining ratio of one dye molecule per ten base-pairs of DNA. Stained DNA was stored in 1xTE Buffer. The buffer typically used for experiments was a solution of Tris salt, brought to near pH 8, the pKa of Tris, by titration with hydrochloric acid. For experiments, 2% beta-mercaptoethanol (BME) was added to the buffer to prevent photobleaching.

Because Tris is a weak base, acid-base equilibrium calculations must be used to calculate the ionic strength from the concentration. At a pH of 8, the pKa of Tris, the ionic strength is half the nominal Tris concentration [29]. A 2 percent BME solution (pKa=9.6) dissociates partially and contributes 7 mM

to the ionic strength. Thus, a 50 mM Tris solution has an ionic strength of 32 mM. At very low Tris concentrations (below 10 mM), it is difficult to stabilize the pH without overwhelming the Tris with the titrating HCl or the BME. In addition, the buffer becomes unstable to acidification by atmospheric CO2, and can vary over the course of an experiment.

Buffers were degassed for at least an hour before experiments, and replenished with degassed deionized water to maintain concentration. The degassing was useful for eliminated dissolved oxygen, which promotes photobleaching, and bubbles, which make it difficult to control the hydrostatic pressure inside the chip. The Tris-BME solution was mixed with the stored DNA solution in a ratio ranging from 19:1 to 9:1, in order to ensure an ideal concentration of molecules inside the device (concentrated enough for good statistics, not so concentrated that they overlap).

2.2.3 Pressure Control and Macro-Micro-Nano Interfaces

The nanofluidc slits are too small for a human to directly inject a DNA buffer into them. In order for fluid loading, they are connected to microfluidic reservoirs, which are still too small for humans to access. Consequently, the microchannels are connected to millimeter-diameter holes blasted through the chip, which are large enough for humans to inject buffer with a micropipette tip.

The interface between the micro- and nanofluidic components of the chip and the rest of the world was through a plastic chuck (Figures 2–4 and 2–5). The original chuck was designed by Walter in Denmark (the DanChuck), and a more recent version was designed by Rob Welch in Canada (the CanChuck) and made in the McGill Physics machine shop. The basic principle involves

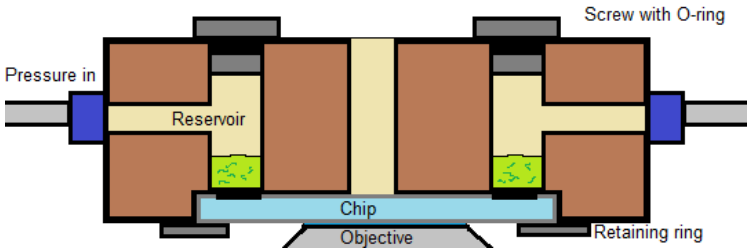

Figure 2–4: A diagram of the chuck in cross-section. The glass chip is affixed to the plastic chuck with a metal retaining ring, and vertical reservoir tubes allow pipette access. Transverse to the reservoir tubes are lines connected to an external gas source, to apply pressure to the reservoirs. A central borehole allows overhead white illumination.

lining up millimeter-diameter vertical reservoir tubes with the reservoir holes of the chip and sealing them with O-rings, tightening the chip onto the O-rings by screwing it on with a metal plate.

Each of the four reservoir tubes was connected transversely to a Luer connector through which air or nitrogen gas flowed. By increasing the pressure to each of the reservoirs, typically on the order of 0.1 bar, the fluid and DNA could be made to flow in the desired direction, either along the reservoirs by applying pressure to one, or from the reservoirs and into the nanoslit by applying pressure to two adjacent reservoirs simultaneously. The pressure required to drive DNA into the slit depended on the height of slit, with a full atmosphere of pressure insufficient for injecting DNA into a 30 nanometer slit, while tens of millibar were required to inject it into a 200 nanometer slit. There is a large body of work dedicated to understanding driven motion of fluid and polymers through microfluidic geometries [85], but in this thesis I am concerned with equilibrium behaviour.

2.2.4 Optics

An inverted fluorescence microscope was used for imaging with a high numerical aperture (NA) objective lens, typically a 100x oil immersion lens (NA 1.4), but occasionally a 60x oil or water lens, was used. Our imaging setup is a standard configuration used in single-molecule nanofluidics work. The chip, at the bottom of the chuck, sat atop the lens. The layer of oil separated the glass of the chip from the glass of the lens. The chuck, with the device fastened to its bottom side, is positioned so that the chip can be accessed by raising the objective. The chip is actually oriented such that the pits are on the top wall rather than the bottom, although I represent it the other way in schematics. Gravity is not relevant here as it is negligible compared to thermal motion at these scales. Illumination was provided by an X-Cite mercury lamp that was filtered by a dichroic filter to illuminate the YOYO-1 stain at a peak frequency of 491 nm and the emissions at 509 nm were detected by an Andor iXon EM-CCD, useful for faint sources.

The fluorescent stain in known to photobleach, and if the light is too intense it can cause the molecule to fragment (this is called photonicking). If possible, the full lamp power is not used, and it is controlled either with the power setting on the lamp or through neutral density filters. If the lamp is properly functioning, imaging is performed at 50 % illumination.

2.2.5 A Day in the Lab

An overview of the experimental procedures can be found in my master's thesis [86]. After degassing the buffer solution and mixing it with BME and DNA, it can be injected into the reservoirs of the chip. If the chip has never been used before, time is required for initial wetting by capillary action, as the

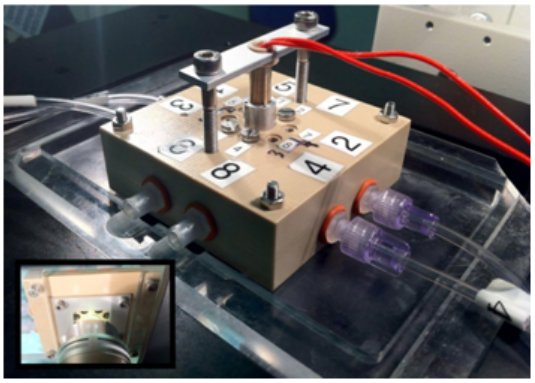

Figure 2–5: A photograph of the chuck on top of the microscope. Inset: a view from the bottom, showing the objective lens abutting the chip within the metal retaining ring. This image used with permission from Rob Welch.

fluid displaces the air. This can be seen by holding the chip up to a window and watching the reservoirs disappear as the air is displaced by water, whose index of refraction is closer to glass. Roughly two microliters of buffer solution are used in each reservoir for wetting, and only one reservoir on each side should be initially loaded so that bubbles do not get trapped in the middle. The chip is loaded onto the chuck by lining up its reservoir holes with the O-rings and screwing it in, then roughly 15-20 microliters of DNA-buffer are loaded into each reservoir tube, and the sealing screws are screwed onto the tops. The gas lines are connected to the Luer connections on the chuck, and it is loaded on top of the objective lens.

The fluidic network makes up a small fraction of the area of the chip, and can be hard to find, especially if out of focus. I typically find them by scanning around the chip with the positioning stage joystick, illuminating it with white light, and looking through the eyepiece until shadows are noticed. Then, I try focusing on the shadows, and if the microchannels appear then I follow them until I find the nanoslits. When I have found the slits, I switch to fluorescent

imaging and look for the DNA, making sure I can control its motion transverse and into the slits with the different pressure knobs. If there is good fluorescent signal, and the molecules can be controlled and equilibrated, the experiment can begin.

I focus the microscope on a specific geometry, and apply a burst of pressure to drive the DNA into the slit to that geometry. When the molecules are in equilibrium, I record a movie with the CCD, which is saved to the computer's hard drive. I typically film for 60 to 90 seconds at 10 continuous frames per second. I repeat this several times for each geometry, until I have filmed a large ensemble of molecules (typically five movies per geometry) before translating to another geometry on the chip. I repeat this for each geometry, approximately one every half-hour, moving throughout the entire chip over the course of a day. The experiment ends when all geometries have been filmed, when the signal becomes too weak, or when the experimenter becomes too fatigued. More recently, using chips with a greater number of geometries, I focus the camera on the interface of several of them, taking a bright-field image to locate the interfaces, and filmed two to four geometries at a time. Movies with a larger field of view and a long filming time are unfeasible and the size of the files must also be considered.

It is crucial to understand which geometry is being observed. In his initial experiments, Walter calibrated the positioning stage to the positions of the alignment marks on the chips, then recorded the position at which each movie was taken, allowing the geometry to be ascertained from the CAD designs afterwards. I opt for a different approach, using the filenames of the movies to store information about the geometries. Typically, the filenames of movies

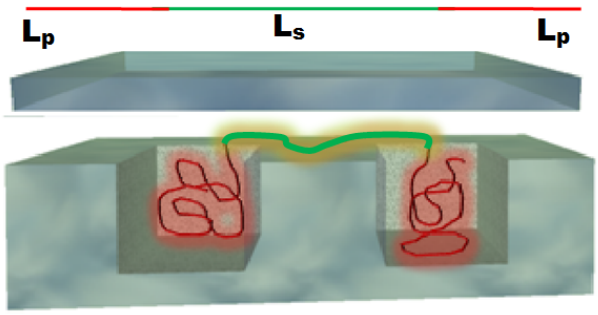

Figure 2–6: A diagram of a chain partitioning contour length L_p into $N = 2$ cavities, with a linker of length L_s between them.

would contain either the geometry (for example 500nmPits001.nd2) or about the position of the geometry on the chip (LeftSlitSecondFromTop001.nd2), ensuring that the overall orientation of the chip is recorded.

At the end of the day, all the movies were saved to a portable hard drive and taken to my office. There, they were converted from the microscope's file format to either AVI or TIF, so that they could be analyzed by one of the procedures described in the following chapters. The chuck was dismantled and cleaned, and the chip was stored in a low-salt buffer in the fridge.

2.3 The Free Energy of Confinement in the Nanopit-Nanoslit System

The measurements that are taken are used to probe the underlying polymer physics governing the confined DNA. The measurements and the physics are related through a free energy model that links the two.

Consider a chain of total length L that partitions an equal amount of contour into a number of pits, N (Figure 2–6). The length of contour per pit is L_p. When contour is removed from the tightly confining slit into the pit, it gains entropy as more conformational states become available. There

is a free energy benefit, linear with the contour removed from the slit, to this process. However, as the density of monomers inside the pit increases, excluded volume interactions arising from pairwise collisions along the chain contribute an energy that disfavours the pit [78]. The excluded volume free energy is thus quadratic with the contour length per pit, with a prefactor equal to the ratio of the effective width of the molecule and the volume of the pit. Each adjacent pair of occupied pits is connected by a linking strand with contour length L_s, and a certain amount of energy is required to stretch an entropic spring between the two pits.

Thus, the total free energy of confinement as a function of L_p is:

$$\frac{\Delta F}{kT} = N\left(-AL_p + BL_p^2\right) + (N-1)\,F_{spring}\,(L_s) \tag{2.1}$$

The value of L_s is constrained to the value of L_p through the conservation of the total contour length of the molecule, L, such that $NL_p + (N-1)L_s = L$. Here, we have assumed that the contour in each cavity is equal, as is the contour in each linker. This condition is on average satisfied at equilibrium, but can be relaxed. The parameters A, B, and F_{spr} represent the strengths of the entropic, excluded volume, and elastic energy factors respectively.

2.3.1 The "A" Parameter: Entropy

The A parameter represents the entropy gained from moving contour from the highly confining slit into the deeper cavity. Because free energy is minimized when entropy is maximized, this parameter is negative, implying energy decreases when L_p increases.

In reality, there is an additional entropic cost of confining contour in the cavities. This means that A is divided into two contributions:

$$A = A_{slit} - A_{cavity} \tag{2.2}$$

This energy difference is used to determine if a given configuration is stable. If a measurement of only A_{slit} is desired, A_{cavity} is something that must be taken into account in order to isolate the slit component. The simplest parameterization for A is that of the ideal chain, discussed in Chapter 1:

$$A_{slit}^{Ideal} = \alpha \frac{p}{h^2} \tag{2.3}$$

$$A_{cavity}^{Ideal} = \alpha \left(\frac{p}{d^2} + 2\frac{p}{a^2} \right) \tag{2.4}$$

The symbol α is often used in this thesis to denote dimensionless prefactors of order unity, whose importance is lessened when we are primarily concerned with scaling. In this case, the traditional value of α is $\pi^2/3$. In typical cases, $d = 2h$ and a is typically several times larger than h so it is tempting in the ideal case to neglect the transverse cavity component and have $A = 3/4A_{slit}$.

Similar arguments can be presented for the Odijk regime, but in reality h is such that neither limiting regime applies, and the Chen-Sullivan equation is the best theoretical point of comparison. Similarly, although a is larger than both h and p, it is not asymptotically larger than either, and a semi-flexible model for cavity confinement is required. Unfortunately, none existed prior to this thesis, but I spoke with Jeff Chen, a moiety of the Chen-Sullivan equation

and a world expert in polymer SCFT calculations, who developed a series of numerical solutions for the free energy of the wormlike chain in a cylinder.

The solutions are based on the energy eigenvalue problem for the wormlike diffusion equation in a cylindrical geometry, yielding the energy per Kuhn segment as a function of height and radius. Either geometric variable can range from much than to much larger than the Kuhn length, and the isotropy of the cylinder can vary from very tall and channel-like, to compact and isotropic, to very flat and slit-like. There are multiple limiting scalings based on both the isotropy and the dimensions: channel-Odijk, slit-Odijk, slit-Ideal, channel-Ideal, cavity-Ideal, and liquid crystalline (when everything is small and isotropic).

To map the round cylinders onto our square cavities, we make the ansatz that in the ideal cavity limit, a cylinder of effective radius r_{eff} should have the same energy eigenvalue as a box with width a. Both limiting cases are known (this is the particle in a box problem for a square and for a circle), and the two are equated with $r_{eff} = a/1.85$.

Although it has no theoretical basis, for use in closed-form expressions the semi-flexible cavity energy from SCFT can be well-fit by the following function:

$$A_{cavity} = \frac{1}{2p}\left[0.651\left(\frac{d}{2p}\right)^{-1.37} + 1.92e^{-\frac{0.34a}{p}}\right] \tag{2.5}$$

2.3.2 The "B" Parameter: Excluded Volume

The B parameter, the second virial coefficient, is the energy cost due to excluded volume interactions in the cavities, which is quadratic with L_p

as discussed in Chapter 1. This component is positive, meaning it favours partitioning contour in the slit rather than the cavities. According to the mean-field scaling for excluded volume, this term is proportional to the ratio of effective molecular width to the volume of the cavity, which is a square prism of width a and depth d:

$$B = \frac{\pi}{4}\frac{w}{a^2 d} \tag{2.6}$$

Because in our experiments d is fixed while a varies, we often normalize by the cross-sectional area a^2 and discuss the scaling of an "areal excluded volume" term B' that has units of energy.

The theory for a spherical cavity as presented by Sakaue has essentially been re-mapped onto a square cavity by equating the volume in both geometries. It is possible that additional small geometric prefactors may have been lost in translation. Additional "surface terms" or terms arising from entropy loss in the cavity are included within A_{cavity}, which favours the slit, rather than B which is only the component of the energy that is quadratic with contour.

2.3.3 The Elastic Term

The elastic component, F_{spring} is parameterized by integrating an elastic force over the distance separating adjacent pits, ℓ. The tension in the linking strand is minimized when its contour length L_s is large compared to the pit separation ℓ, and maximized when it equals ℓ and the chain is totally stretched. Thus, minimizing the elastic energy favours contour in the slit rather than the cavities. In its simplest form, the harmonic energy from the ideal chain is simply:

$$\frac{F_{spr}^{Ideal}}{kT} = \int_0^{\ell} \frac{3\ell}{2pL_s} d\ell = \frac{3\ell^2}{4pL_s} \tag{2.7}$$

With the semi-flexible Marko-Siggia force [82], the energy of the spring is:

$$\frac{F_{spr}^{MS}}{kT} = \int_0^{\ell} \frac{d\ell}{p} \left[\frac{\ell}{L_s} + \frac{1}{4\left(1 - \frac{\ell}{L_s}\right)^2} - \frac{1}{4} \right] = \frac{\ell^2 \left(3\, L_s - 2\, \ell\right)}{4p \left(L_s - \ell\right) L_s} \tag{2.8}$$

The Marko-Siggia energy applies to a stretched chain in the bulk. To find the force-extension relationship of a stretched chain in a slit, Hendrick de Haan and Tyler Shendruk performed molecular dynamics simulations and mapped them to a version of the Marko-Siggia equation that maps between the 2D and 3D limits [11]. They use an "effective dimensionality" that is based on the in-plane persistence correlation length, which increases towards twice the bulk value in the 2D limit. According to their parameterization of the effective dimensionality, my experiments take place between effective dimensions 2.24 and 2.78.

The parameterization of their model is:

$$\frac{F_{\text{spr}}}{kT} = \frac{\ell^2}{4pL_s} \frac{(D_{\text{eff}} - 1)}{4\,(L_s - \ell)} \left[2L_s D_{\text{eff}} - \ell\,(D_{\text{eff}} + 1)\right]. \tag{2.9}$$

The effective dimensionality, based on measuring in-plane correlations, is

$$D_{\text{eff}}(h) = 1 + \frac{2}{2 - e^{-0.882(p/h)^{1.441}}} \tag{2.10}$$

2.4 The Free Energy Landscape

All the terms in equation 2.1 have now been defined in terms of geometric parameters. With the simplest choices of parameterization, the free energy is:

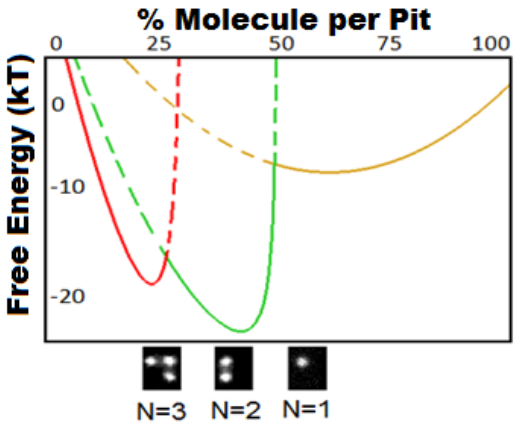

Figure 2–7: Free energy landscape for a molecule able to access the $N = 1$ $N = 2$ and $N = 3$ states. Within each state, there is a potential that depends on the partitioning of contour between the pits and slits. The $N = 2$ state has the deepest minimum and is thus most likely to be occupied.

$$\frac{\Delta F}{kT} = N\left(-\frac{\pi^2}{4}\frac{p}{h^2}L_p + \frac{\pi w}{8a^2h}L_p^2\right) + (N-1)\frac{3\ell^2}{4p\,(L - NL_p)} \tag{2.11}$$

For a common geometry, each different occupancy state defines a different free energy potential as a function of L_p (Figure 2–7). These different potentials represent a free energy landscape, where the molecule can move up and the potential of a given state by repartitioning contour around the equilibrium level, or undergo a transition to a new state and occupy a new potential.

2.4.1 Case Study: Single Molecule Diffusion

A demonstration of this free energy landscape, as well as the utility of this complex nano-device, can be seen by examining the hopping-mediated diffusion of DNA molecules through the nanopit lattice. The free energy model predicts a different potential for each occupancy state. The molecule will tend to occupy the state with the lowest free energy minimum, the ground state.

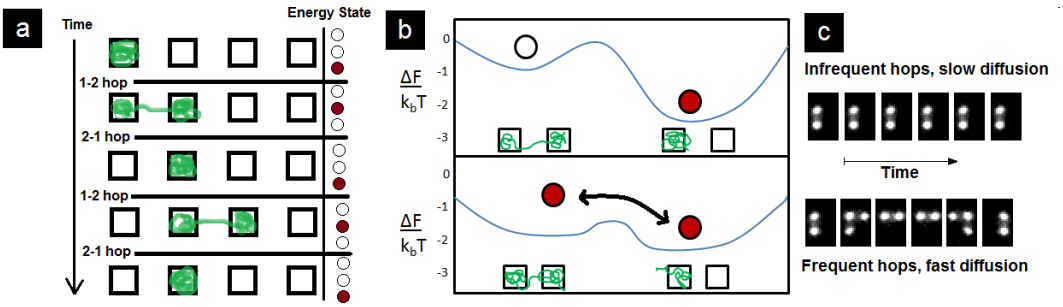

Figure 2–8: a) The mechanism of diffusion, involving discrete hops between energy states that displace the centre of mass. b) Two model free energy landscapes demonstrating that diffusion can be fast or slow depending on the stability of each state. c) Time series of a DNA molecule demonstrating slow and fast diffusion.

It will remain there until the molecule undergoes a thermal fluctuation into a higher energy state, either one of higher or lower occupancy. Then, it will relax back to the ground state, returning to its preferred occupancy. Through this process of excitation and relaxation between states, the molecule diffuses throughout the array (Figure 2–8).

The probability that a transition occurs is based on the energy difference between states. In some geometries, these energies are far apart, and excitations from the ground state are rare, and diffusion is strongly damped. In other geometries, the energies are close to one another and transitions are common, and diffusion is not expected to be significantly lower than its free-slit value.

The diffusion of DNA molecules hopping through the nanopit arrays was recorded, measuring an ensemble of molecules in different geometries. The positions of the molecules over time were measured by superimposing a digital grid of boxes over the pit matrix in each frame and registering the boxes in which the integrated intensity exceeded a threshold. The centre of mass

of each molecule was calculated over time, and the diffusion coefficient was calculated using an over-sampling technique (based on position correlations between frames) discussed by Wang et al. [87].

When a molecule is in the largest pits, the molecule occupies a single pit and there is essentially no diffusion as the monomer ground state is much lower in energy than the dimer state. However, as the pits become smaller, excluded volume interactions in the monomer state bring it closer in energy to the dimer state, and 1-2 hopping is seen, and the diffusion generally increases with decreasing pit size, as transitions between 1-2, 2-3 and eventually 3-4 become more common. Interestingly, there are certain regions of parameter space with local minima in the diffusion (Figure 2–9). As the pits get smaller, the ground state gradually increases, from $N = 1$ to $N = 2$ to $N = 3$ etc, and at a certain point in parameter space each occupancy ground state will be much lower than the first excited state, leading to these diffusion minima. The diffusion maxima correspond roughly to the transition between ground states: if both the $N = 1$ and $N = 2$ state are near the global minimum of the free energy landscape, there will be frequent hops between them.

This non-monotonic dependence of the centre-of-mass diffusion highlights the utility of a free energy landscape to describe this system, in that the difference in energies between states allows a knowledge of the conditions that will enhance or damp diffusion. Being able to fine-tune the diffusion to a local maximum or minimum also highlights the power of complex nanofluidic systems: being able to vary the partitioning of a molecule using multiple degrees of freedom can allow very precise control over dynamic as well as equilibrium

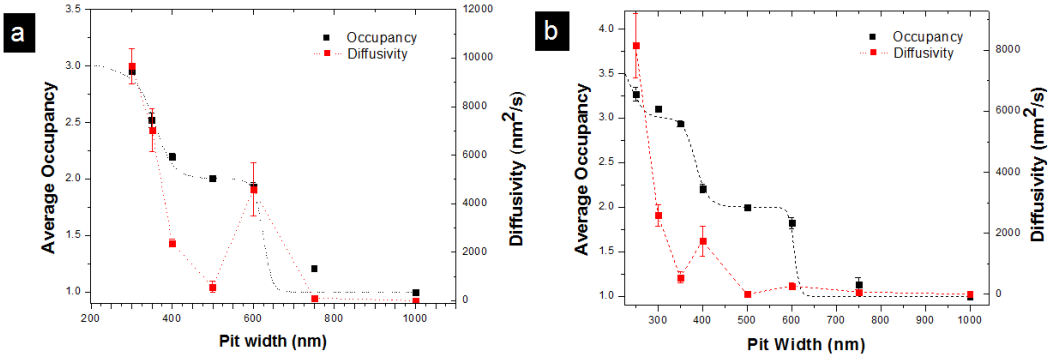

Figure 2–9: Measurements of molecule centre-of-mass diffusion with respect to pit width for two systems, alongside occupancy measurements. a. Diffusion and occupancy as a function of pit width in a nanoslit with h=100 nm. A local minimum in diffusion corresponds to a stable dimer state. b. Diffusion and occupancy as a function of pit width in a nanoslit with h=70 nm . Two local minima in diffusion correspond to stable dimer and trimer states.

properties. Similarly to how λ-DNA is either trapped or freely hopping depending on the choice of geometry, within a single geometry a size-distribution of DNA molecules will lead to certain sizes being trapped while others may diffuse freely, and such a device can be used to isolate certain sizes of molecules at equilibrium. Although we only looked at diffusion, the same considerations apply to mobility, and size-dependent damping of macromolecular mobility based on the free energy landscape can allow an effective "band-pass" filter for certain sizes of DNA.

More complex lattices can display even more interesting effects: if the sizes of adjacent pits increase in a gradient, for example, the system serves as an effective brownian ratchet where molecules will preferentially diffuse in the direction of larger pits. Brownian ratcheting was observed in a lattice with a pit size gradient, where molecules were observed to collect at the maxima of the gradients (Figure 2–10)

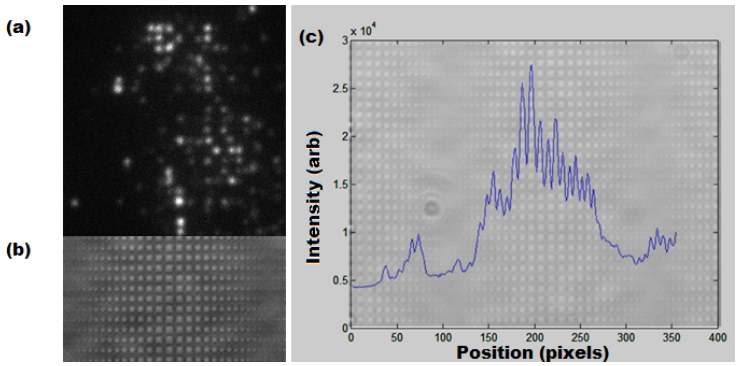

Figure 2–10: (a) DNA molecules of varying size in a lattice with a pit size gradient. (b) Bright field image of the gradient. (c) Intensity profile of DNA concentration, superimposed with the image of the lattice. Intensity peaks correspond to the largest pits.

2.5 Conclusion of Introduction

An overview of the experimental system and free energy model has been presented, and a case study of its application to single-molecule diffusion has been discussed. The remaining chapters will discuss how measurements of DNA in this system can be compared with the free energy model to make precise measurements of the underlying polymer physics.

CHAPTER 3
Single Molecule Tetris: Measuring the Free Energy of Confinement

3.1 Introduction

This chapter discusses measurements of the free energy of confinement and self-exclusion that can be made simply by imaging the molecules in their equilibrium nanopit configurations. In particular, I look at how observations of the average occupancy in different geometries can serve as a way to measure the entropic and excluded volume contributions to the free energy of confinement. In addition to their sensitivity to the underlying polymer physics, these energy measurements are crucial for understanding molecular behaviour in complex systems, for example, the conditions under which molecules can be stably trapped.

We use the canonical ensemble to relate the probability of a chain occupying a given state to the free energy that depends on the A and B parameters, and use measurements of the average occupancy to find experimental values for the energy contributions. We call this Single Molecule Tetris because when a molecule occupies four cavities, it looks like a shape from the classic video game Tetris.

3.2 Theory of Multiple-Pit Occupancy

We return to the free energy of confinement for a molecule occupying an arbitrary number N pits, with an equal amount of contour L_p per pit:

$$\frac{\Delta F}{kT} = N\left(-AL_p + BL_p^2\right) + (N-1)\,F_{spring} \tag{3.1}$$

Each occupancy state has an equilibrium value of L_p which minimizes the free energy, termed L_o. There is a simple expression for L_o at $N = 1$: $L_o = A/2B$, and there is an unreasonably complex expression for higher N states assuming an ideal spring, but generally for higher states, a closed-form solution for L_o does not exist and it must be found numerically.

A partition function can be defined based on the minimal free energy for each occupancy state ($\Delta F_{min}(N)$) and the degeneracy of each state, which is equivalent to the number of self avoiding walks with $N-1$ steps [88]:

$$Z = \sum_{N=1}^{\infty} \Omega_N e^{-\frac{\Delta F_{min}(N)}{kT}} \tag{3.2}$$

Within the framework of the canonical ensemble, the probability of a molecule being found in a given state is:

$$P(N) = \frac{e^{-\frac{\Delta F_{min}(N)}{kT}}}{Z} \tag{3.3}$$

The average occupancy can then be calculated with a weighted sum of the probabilities:

$$\langle N \rangle = \sum_{N=1}^{\infty} P(N)N \tag{3.4}$$

This is the parameter that is measured experimentally.

3.3 Experimental Procedures and Considerations

Our experimental procedure is quite simple: it involves filming molecules at equilibrium in the nanopit lattice (Figure 3–1). The average number of

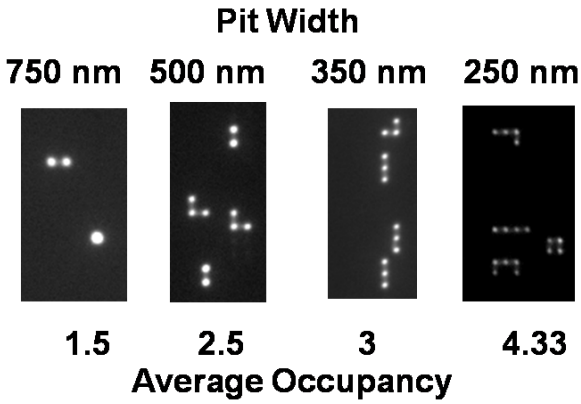

Figure 3–1: Fluorescence micrographs of molecules in several different lattices with decreasing pit width and increasing occupancy. The molecules undergo thermal transitions between states.

pits that they occupied in a given lattice is determined, and measuring this quantity in all geometries of a given chip, at different pit sizes and spacings. An experiment would involve flowing DNA into a given geometry, filming it for over a minute, and repeating with fresh molecules until sufficient statistics are acquired. This procedure is iterated over all lattice geometries present on a given device.

In order to ensure that the best approximation to the true ensemble average is obtained, it is essential that molecules undergo several conformational transitions between different nanopit states over the course of a given movie. The typical recording time was 90 seconds, at 10 frames per second (100 ms collection time) such that each movie was 900 frames. Movies over longer periods of time would have been desirable for aforementioned reasons, but would result in fewer total molecules imaged over the course of an experiment. A 900-frame 512 by 512 pixel image is roughly 600 megabytes, and files over 1 gigabyte are

very difficult to work with using the available software. If possible, the number of pixels in the image was reduced in order to use less memory, without sacrificing molecule count. The movies could be made longer by filming with a duty cycle, as was done in my work on long-time diffusion [12], but doing so discards information about short-time intramolecular fluctuations. Theoretically, the ergodic principle allows mere snapshots of molecules to serve as a measure of their statistical average, but the possibility of metastable states due to initial conditions necessitate filming a longer movie. The 900 frames 100 ms movies were found to be a happy medium of all these considerations. We chose illumination settings to achieve a balance between high signal and minimal photobleaching. Because in the occupancy measurements the molecules tended to occupy the same state for tens of seconds, we could frame-average after the experiments without losing information about the average occupancy.

These experiments required mechanical equilibrium, and a pressure imbalance across the slit negates this. A large pressure imbalance is obvious to detect because the molecules do not stay still. A small pressure imbalance is subtler, and only evident when watching the movie after it is recorded, to see that each molecule has made several transitions in one direction. If molecules are seen making transitions in both directions along the slit's flow axis, they are considered to be in thermal equilibrium, although a very slight imbalance, not enough to dislodge the molecules from their occupied state, may still bias their transitions in one direction. If the time-scale of flow-induced transitions is not much shorter than the time-scale of state occupation, then the instability will not significantly affect the occupancy, although it may shorten the time spent in the excited states.

A CEGEP student, Philippe Fortin Simard, measured the occupancy of a single geometry at different flow speeds to determine if there was an effect on the occupancy, and there was not, over the range of speeds he tested. A small flow can be used to sample a greater number of states in a given recording time and reduce sensitivity to metastability, but this method should be examined more systematically, before relying upon it for equilibrium measurements.

3.3.1 Occupancy Analysis

Molecules spanning multiple pits were analysed using a MATLAB program developed by Hugo Brandao as part of a summer research project, and was discussed extensively in my master's thesis [86] and Hugo's undergraduate report [89]. It involves aligning a digital grid over the movie such that the squares of the grid are aligned with the pits. An intensity threshold is set such that any grid square with an intensity above this is registered as occupied. Over the course of the movie, the occupancy of each molecule at each point in time is recorded, generating an average occupancy for each molecule and an ensemble average for each geometry. In simplified cases where the molecule does not move very much, it can sometimes be faster simply to write down the number of frames spent in each state and calculate the average occupancy by hand.

3.4 Analysis and Results

3.4.1 Occupancy Trends

Several occupancy plots are seen in Figure 3–2. For the largest pits with sufficient separation, a molecules occupies only a single pit. As the pits become smaller or closer, a molecule will occupy a greater number of them, and occupancy generally decreased with slit height. For sufficiently small pits, the

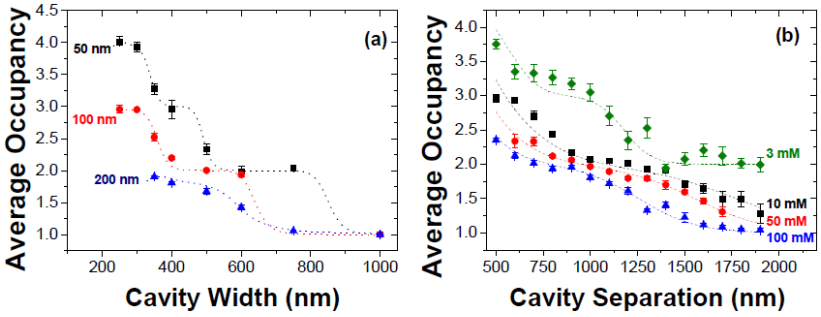

Figure 3–2: (a) Measured occupancy as a function of pit width at several slit heights. (b) Measured occupancy as a function of pit spacing at several ionic strengths.

effective free energy potential of the pits becomes relatively weak compared to the thermal energy scale, and the molecules can be seen disengaging from their lattice configurations. As the geometry is varied, there are regions of parameter-space termed plateaus where a single state dominates, and the average occupancy is close to an integer. Between these plateaus are transition regions where the two lowest states are close to each other in energy and thermal transitions are frequent.

Experiments were performed at several ionic strengths in a chip with a 170 nm slit height and 310 nm cavity depth. Overall, occupancy was observed to increase with decreasing ionic strength (Figure 3–3). This is non-trivial result sheds light on two competing effects: at lower ionic strength, the molecule stiffens as the electrostatic contribution to the persistence length increases, increasing the penalty for confinement in the slit and making the pits more favourable, decreasing the overall occupancy. However, the electrostatic screening length also increases at low salt, and the greater effective molecular width leads to more excluded-volume interactions, pushing the molecule out of the pits and increasing the overall occupancy. That occupancy increases with

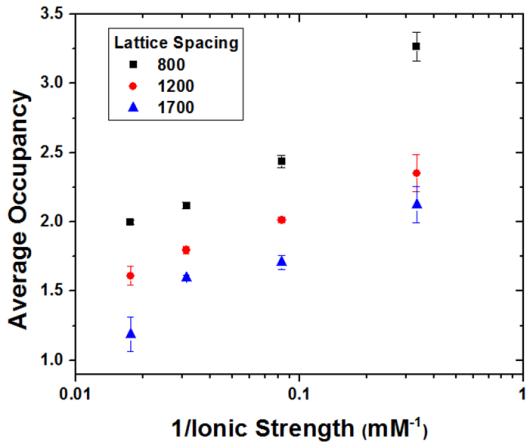

Figure 3–3: Average occupancy as a function of reciprocal ionic strength, at three lattice spacings in a given chip. As the ionic strength is decreased, the occupancy increases.

decreasing ionic strength suggests that the excluded volume effect dominates over the stiffening effect.

3.4.2 Fitting

The free energy parameters A and B have theoretical geometric definitions outlined in Chapter 1, but I am interested in quantifying them experimentally. To measure these parameters, the free energy model is fit to occupancy data, to measure A and B at each slit height.

The outcome of a single experiment is a series of data points for the average occupancy as a function of either pit width or pit spacing (Figure 3–2), typically around eight data points per experiment, but between five and fifteen. Fitting was performed by calculating the average occupancy for a given set of geometric constants, and two free parameters A and B. The occupancy was found by generating an array of free energies for each state (up to a cutoff of $N = 10$) for the entire range of L_p with nanometer resolution, and finding the minimum of this energy array. The minimal energy was used to generate

the partition function and calculate $\langle N \rangle$. This could be calculated for each experimental value of a or ℓ for a given data set.

The fitting was performed using the MATLAB nonlinear least-squares minimization algorithm lsqcurvefit (based on a Levenson-Marquardt algorithm with a trust region), which yielded measurements of A and B.

With the simplest analysis, there is no height-dependence in the energy measurements: a height scaling in A and B emerges naturally from the raw fits. However, as our analysis became more complex, we required two additional steps in the parameterization. The elastic component is parameterized according to the height-dependent effective-dimensionality in the de Haan-Shendruk force law. If we wish to measure A_{slit} instead of just A, it is necessary to add a parameterization of A_{cavity} to the fitting algorithm. In the simplest case this is done by adding an ideal component proportional to $1/a^2$. However, using Chen's full semi-flexible cylinder solutions for which there is no closed form expression, we add a cavity component based on interpolating between the four numerical points closest to the experimental a and d.

Once A and B are measured from the fitting, we can examine how they scale with slit height or cavity depth.

3.4.3 Measuring A: The entropic cost of confinement

The fitting algorithm without modifications makes a measurement of the absolute A parameter representing the difference in the entropic coefficients between the slits and the cavities. To verify whether the parameterization was appropriate, we examined measurements taken as a function of pit spacing,

such that the cavity contribution was the same for each data point, with similar pit widths (roughly 500 nanometers) at four heights (Figure 3–4). The entropic free energy difference in this case is not expected to follow any particular power law, because the cavity isotropy changes as well as the slit height. These measurements were compared to the difference between the Chen-Sullivan slit energy as a function of height and the cylindrical energy for that width as a function of twice the height. Taking into account a physical variation in the etch depths between slit and the pit, the measured energy difference is well-described by the semi-flexible prediction. This suggests that our cylindrical parameterization is justified and can be used to account for the cavity contribution.

To measure the slit component of the free energy, we add a term to the fitting algorithm corresponding to Chen's cylindrical energy at that specific width and depth. The remaining fit parameter is a measurement of A_{slit}, which is the primary quantity to be measured. These results (Figure 3–5) show that the free energy of confinement of slit-confined DNA is that of a semi-flexible chain, in the intermediate range between the Odijk and Ideal limits, governed by the Chen-Sullivan equation and not obeying any power scaling law. These are significant not only for being the first measurements of this quantity, but also because it clarifies the physics of the "transition" between strong and weak confinement (Figure 3–6). In their validation of the Chen-Sullivan formula, these measurements confirm the dominance of semi-flexibility over excluded volume in slit confinement.

The A parameter was measured as a function of ionic strength, using the OSF parameterization of the persistence length (Figure 3–7). At higher

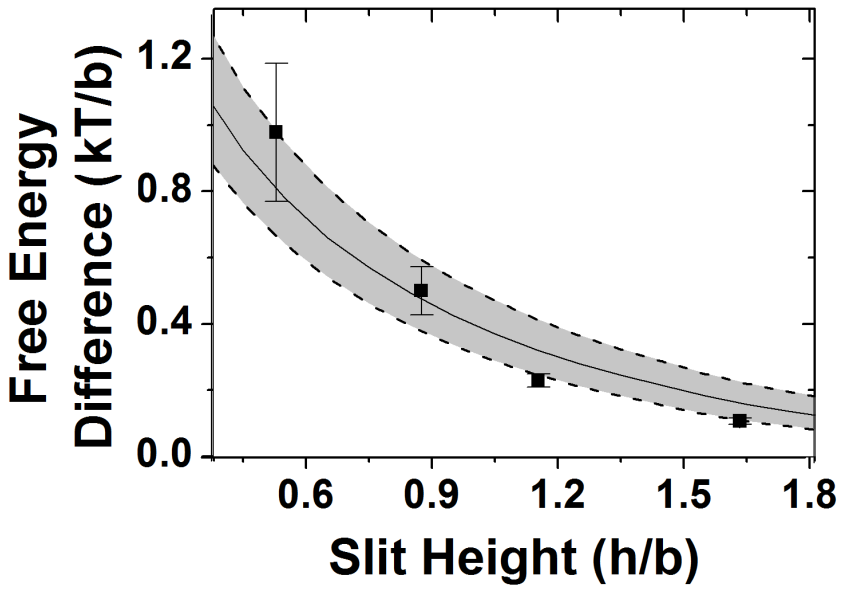

Figure 3–4: Slit-cavity entropic free energy difference for roughly 500 nanometer pits, as a function of the cavity depth. Units are in terms of Kuhn segments. Overlaid is the prediction of the confined semi-flexible chain. The gray region represents the variation in the theoretical prediction due to asymmetry in the slit and pit etch depths.

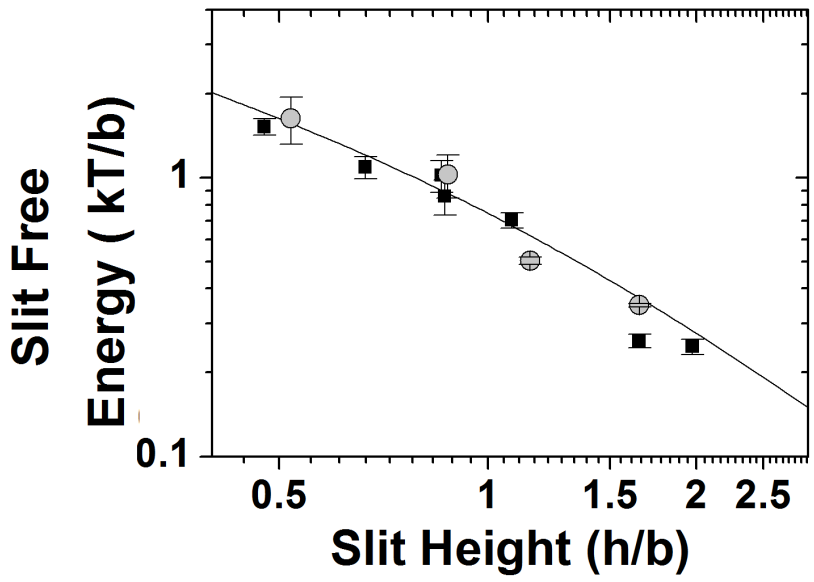

Figure 3–5: Slit free energy of confinement as a function of height, based on the full semi-flexible interpolation. The black points are from data taken with varying pit size and constant spacing, while the gray points are from data taken with varying spacing and constant pit size. Overlaid is the Chen-Sullivan prediction.

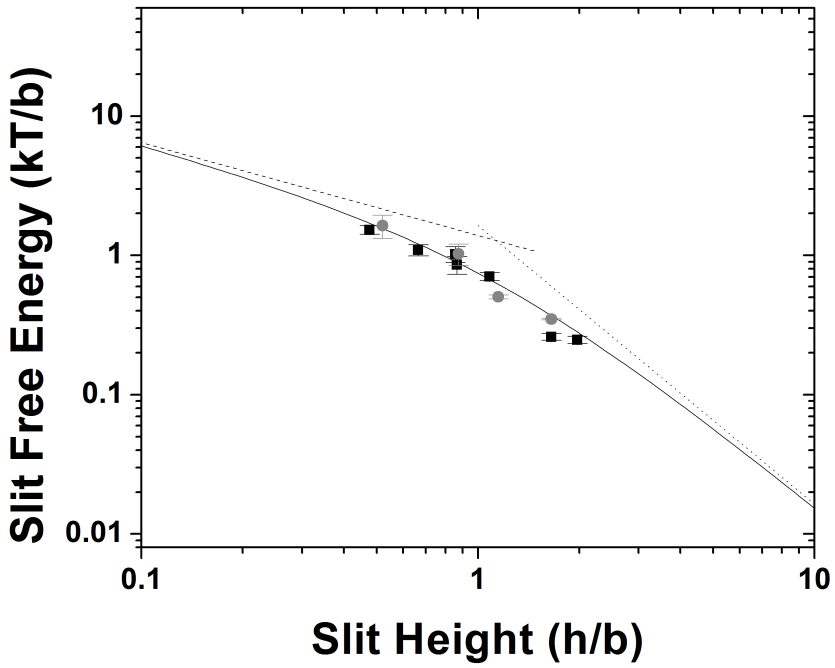

Figure 3–6: The same slit free energy data, with a larger range of heights, showing the approach to the established regimes in both limits.

ionic strengths, there was a relatively weak dependence, consistent with the ideal or semi-flexible chain, where the only change in confinement free energy due to ionic strength is due to the weakly varying persistence length. At lower ionic strengths there is a clear deviation seen from theory, although agreement improves when wall-depletion is taken into account. In addition, there may be a transition towards a stronger confinement regime occurring as the ionic strength is decreased: Stein in a retracted paper [48] found a transition occurring roughly when the persistence length exceeded 58 percent of the slit height. This is not exceeded in my experiments even at the lowest ionic strengths, and Lee et al. [22] did not notice any sharp differences as the ionic strength was decreased.

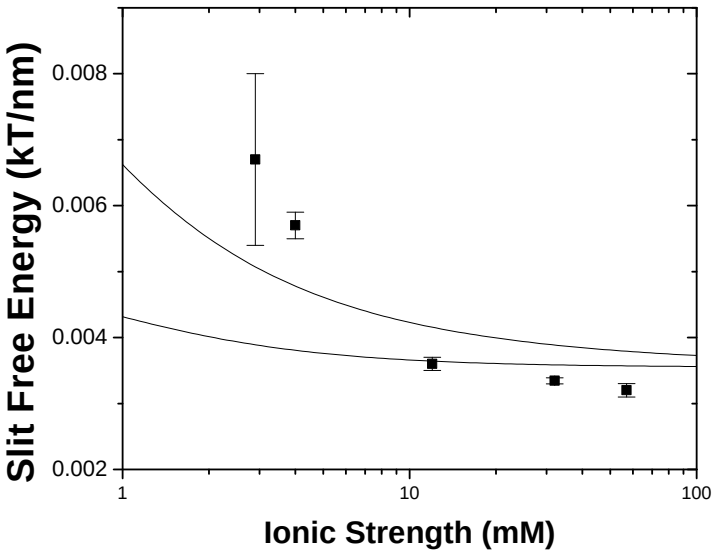

Figure 3–7: Slit free energy of confinement as a function of ionic strength, based on the full semi-flexible interpolation. Overlaid is the Chen-Sullivan prediction taking into account a varying persistence length with ionic strength.

There are generally some experimental issues with low ionic strength. It is difficult to maintain a pH of 8 while keeping Tris is as the primary contributor of ions below about 10 mM, because the BME and HCl will dominate. For the lowest ionic strength data point, only Tris was used and the pH was not controlled and was measured to be above 9. This may change the effective linear charge density of DNA, making it difficult to compare to experiments directly. The lack of BME also makes the molecules more sensitive to photonicking, and generally harder to visualize. In another experiment, 0.1x TBE was used instead of Tris, using 0.5 percent BME as both an anti-bleaching agent and a titrant, bringing the pH to 7.9, allowing an experiment with closer chemical conditions to the rest of the experiments.

3.4.4 Measuring B and w: The second virial coefficient and effective width

To compare between measurements taken with varying spacing and varying pit width, we examine the areal excluded volume coefficient rather than the absolute B parameter (Figure 3–8). According to the prediction of the mean field regime, this parameter should be proportional to the reciprocal cavity depth. Plotting the measured B' against the reciprocal depth yields a straight line, which upon a linear fit is consistent with an effective molecular width of 10.1 ± 1.3 nm, compared to the theoretical prediction of 9 nm. This measurement is particularly significant for two reasons. It represents the first systematic experimental probe of cavity confinement and the role of excluded volume therein. It also represents the first measurement of effective chain width on a single molecule basis, in comparison to all previous measurements that had been performed in bulk. The linear fit that yields the effective width also has non-zero x-intercept, corresponding to the reciprocal of 655 ± 370 nm. This is consistent with the bulk radius of gyration of λ-DNA. We interpret this intercept as a confinement length-scale above which there is no excess energy due to excluded volume.

Measurements of the excluded volume parameter can be converted to measurements of the effective molecular width as a function of ionic strength, using the finite-size offset as a calibration (Figure 3–9). The effective width was found to scale according to Stigter's charged rod theory, with deviations consistent with those in bulk measurements. This is the first set of measurements of this scaling on a single molecule level. There are deviations from

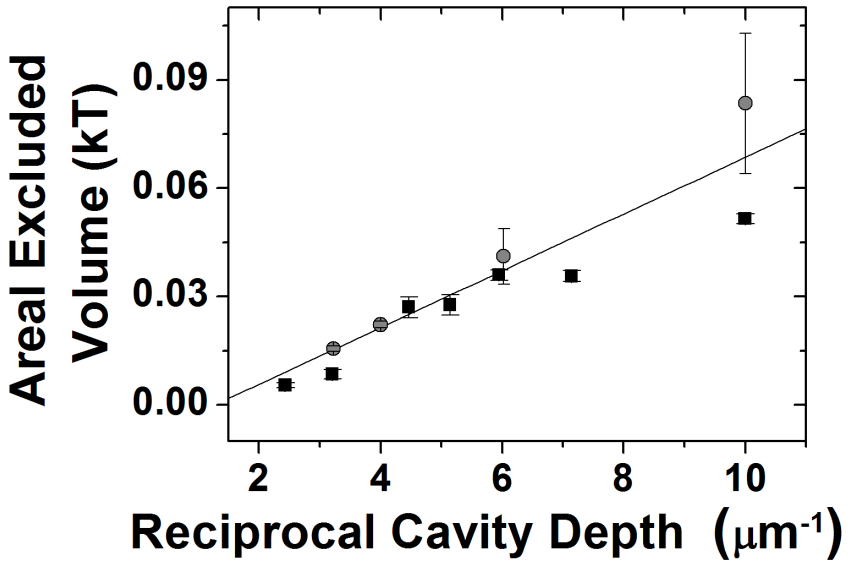

Figure 3–8: Areal excluded volume parameter as a function of reciprocal cavity depth. Black points are from measurements taken with varying width, and gray points are from measurements taken with varying spacing. A linear fit is overlaid.

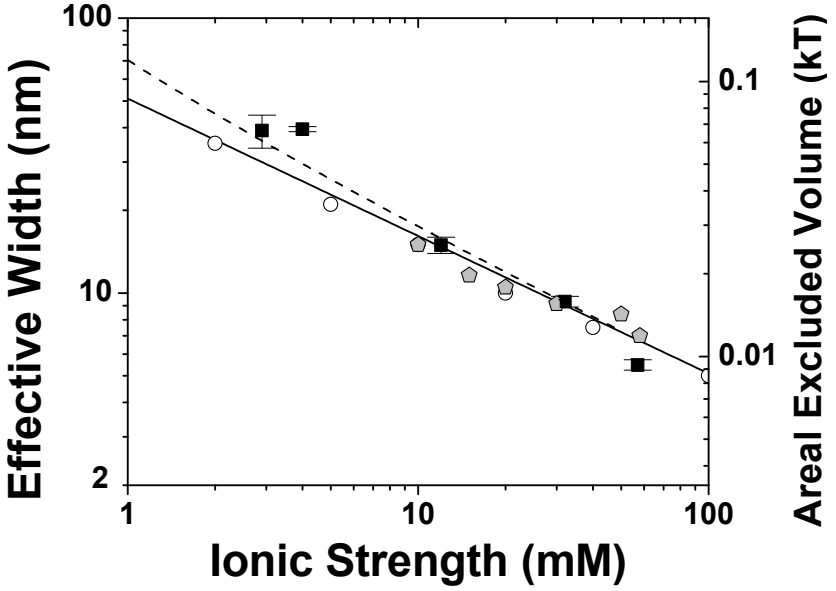

Figure 3–9: Effective molecular width as a function of ionic strength. Overlaid is the prediction of Stigter's charged rod theory. The dashed line corresponds to an imposed wall-offset, and the smaller points are from bulk measurements [10, 21]

theory at the lowest ionic strengths, which may be due to molecule-wall depletion interactions, yielding a smaller effective depth, that have not been taken into account. By attempting to account for these (by subtracting a parameterized effective width), we start to see better agreement at low ionic strength (Figure 3–9). There are also issues with the parameterization of the persistence length, which affects the final measurement from the fitting algorithm, which is not precisely known at low ionic strengths.

3.4.5 Stability Analysis

The molecules are bound to their nanopit states because the free energy potential minimum is below -kT, meaning thermal excitations are unlikely to drive the chain out of the pits into the slit. In certain cases, as the pits become

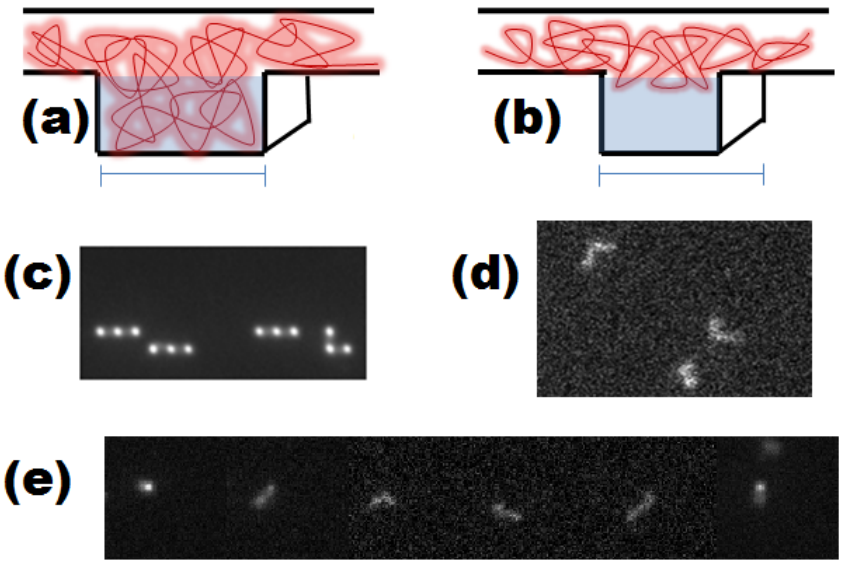

Figure 3–10: (a, b) Schematic showing the stability transition when the pit width becomes sufficiently small for a given height. Fluorescence micrographs show stable (c) and unstable (d) configurations. (e) A time series of a molecule in an unstable configuration starting in a single pit, diffusing out of the pit into the slit, and eventually back into the pit.

sufficiently narrow, this is no longer the case and molecules are seen jumping between the pits and the slit, or simply diffusing around the slit above the pits (Figure 3–10). This is significant from a device perspective, as it allows a knowledge the geometric parameters required to successfully trap DNA.

Normally, the pits act as entropic traps because they are twice as deep as the slit, but if they are narrow enough in the transverse direction then this acts as an additional restriction of degeneracy for contour in the pit, and below a certain threshold, the slit rather than the pit becomes the reservoir of degeneracy. Quantitatively, this occurs when A_{cavity} becomes comparable to A_{slit}

These cases set a limit on the sizes of pits that could be used to make observations, but the decoupling phenomenon itself serves as another method of studying the physics at hand. A molecule will occupy a stable state (here, stable referring to its occupancy in the pits, not the lifetime of one pit-state compared to another) if the minimum of its free energy landscape is below -kT, being unlikely to diffuse out. Considering the free energy for a molecule in a single pit, the conditions by which its minimum is -kT imposes a condition on the relation between A and B. Combining these conditions with our theoretical expressions, a relation is found for the minimum pit width yielding a stable state as a function of slit height. This represents the boundary line on a phase diagram in height-width space of stable and unstable states. Finding these unstable states in recorded videos and placing them on the phase diagram shows that the theoretical line describes the transition well (Figure 3–11).

From the single-pit case, the stability threshold can be found by equating the minimal energy to -kT, by substituting the minimal filling length $L_o = A/2B$ into the expression for the energy. This imposes a constraint on the relationship between the A and B parameters.

$$\frac{\Delta F}{kT} = -A\left(\frac{A}{2B}\right) + B\left(\frac{A}{2B}\right)^2 = -\frac{A^2}{4B} = -1 \tag{3.5}$$

In the simplest case, we can use known geometric definitions of A and B from the ideal chain and mean-field models, the critical pit width at a given height is constrained:

$$4\frac{\pi w}{4da^2} = \left(\alpha p\left(\frac{1}{h^2} - \frac{1}{d^2} - \frac{2}{a^2}\right)\right)^2 \tag{3.6}$$

In the case where $d = 2h$, the critical pit width as a function of height has the closed form solution:

$$a_{crit} = \frac{2}{3}\frac{h}{\alpha p}\sqrt{\pi\, wh + 6\, p^2\alpha^2 + \sqrt{\pi^2 w^2 h^2 + 12\,\pi\, whp^2\alpha^2}} \tag{3.7}$$

This can be solved for other scenarios: the Odijk regime, using the full semi-flexible parameterization of A, or taking into account the bulk offset for the excluded volume parameter. For more complex models, this boundary must be found numerically. For multiple pit occupancies, the stability threshold can be determined numerically, although the position of the threshold is largely independent of occupancy until the widest slits, when it is likely to be found in a single pit regardless. The stability threshold allows us to verify the results of our free energy measurements in a model-independent manner. The measurements are simply a qualitative check of whether the molecule leaves the pits, and the stable-unstable phase diagram can be populated from the results of each experiment. The prediction of the free energy model roughly runs through the stability threshold, lying at most only one data point away from the experimental stability boundary. Figure 3–11 is an additional experimental validation of this model that does not rely on fitting parameterizations.

3.5 Additional Analysis and Considerations

3.5.1 Sensitivity

Two parameters are input into the fitting algorithm as constants: the total contour length of the molecule, and its persistence length. The persistence length depends on the ionic strength of the buffer, but depending on which description of its ionic dependence is used, it is between 52 and 56 nm

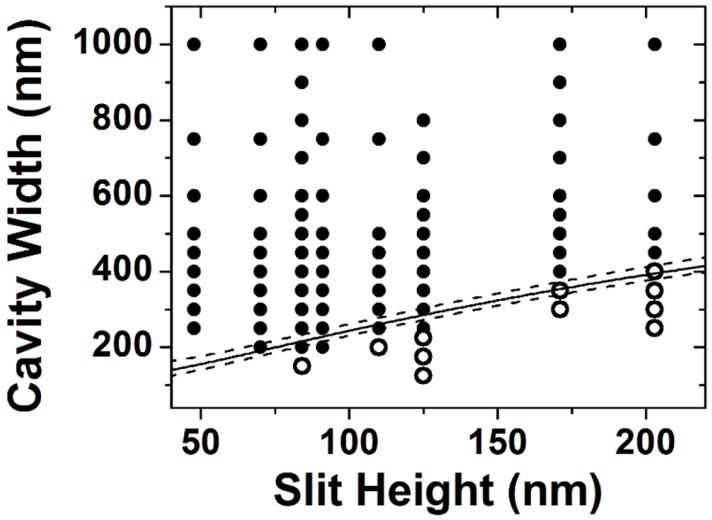

Figure 3–11: Stability phase diagram for DNA in a nanopit-nanoslit lattice. Filled points correspond to geometries where stable tetris states were observed, unfilled points where the molecules were observed diffusing from the pits to the slits, or not occupying the pits at all. The solid line corresponds to the prediction for the the potential minimum equaling -kT, with the dashed lines taking into account 10 percent variation in the slit-pit etch depths.

for 50 mM Tris. Both the persistence length and the total length depend on the intercalation ratio of YOYO-1 dye. A low 10:1 base-pair to dye ratio was used, but the exact lengthening and stiffening due to this is not fully known. In particular, different experimental papers show opposite dependence for the persistence length, whether stiffening or floppening. The contour length dependence is better understood, and is a stronger effect than the weak persistence variation. With 10:1 YOYO-1 intercalation, the lengthening is thought to be roughly 15 % and the change in persistence is thought to be negligible [23].

To test the dependency of the fitting outputs on these input parameters, the fitting algorithm was run with a varied range of inputs (Figure 3–12). Data sets from narrow (50 nm) and wide (170 nm) slits were fit, and the bare-bones parameterization was used (Marko-Siggia force with no cavity component). With respect to persistence length, the measured parameters decrease as its input value is increased, roughly the same for narrow and wide slits and for A and B. With respect to the contour length, again a larger input value leads to smaller parameters, but the dependence of the B parameter was significantly stronger than A. The ambiguity over the lengthening role of YOYO-1 may indicate that our uncertainties are underestimated. The fact that the dependence on the input parameters is roughly the same for narrow and wide slits indicates that the overall observed scaling trends are robust under changes in these parameters, even if their values may not be.

There is also a sensitivity to our choice of parameterization of the ionic dependence of persistence length. At the higher ionic strengths used for most experiments, this is a relatively minor difference. At the lowest salt concentrations used, this varies between 60 and 80 nm, a significant difference. We

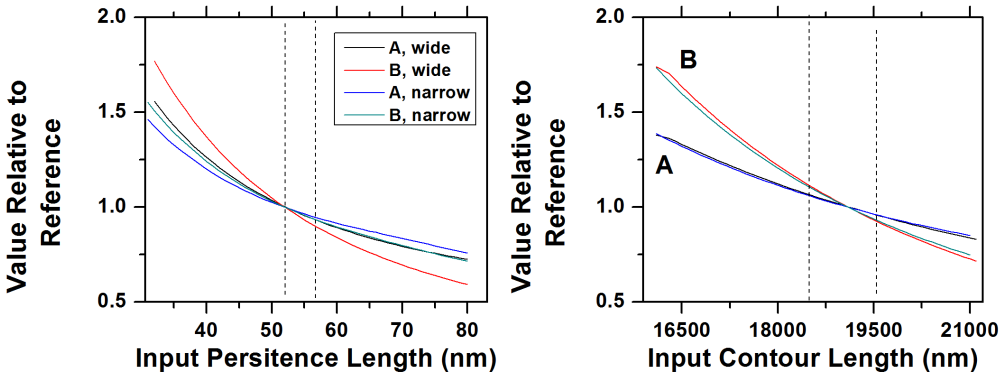

Figure 3–12: Left: Sensitivity of fitting parameters to the input persistence length, for two sets of data. The range of ambiguity is outlined with dashed lines. Right: Sensitivity of fitting parameters to the input persistence length, for two sets of data. The range of ambiguity is outlined with dashed lines.

can parameterize the fits at different ionic strength using both the OSF and Dobrynin models to see what effect this has on the measured fit parameters (Figure 3–13). Ultimately the difference in the fit parameters is negligible, but the observed behaviour in the scaling of A is closer to that predicted by OSF. The results for excluded volume have very little dependence on this.

3.6 Conclusion for Chapter 3

In this section I have used measurements of the average occupancy to study the first two virial contributions to free energy of confinement. Measurements of the entropic cost of confinement, are consistent with the expected energies of a confined semi-flexible chain. The slit component of this free energy falls with height consistently with the Chen-Sullivan interpolation formula, which is not described by a power law. I have made the first set of systematic measurements of cavity-confinement physics with DNA, measuring

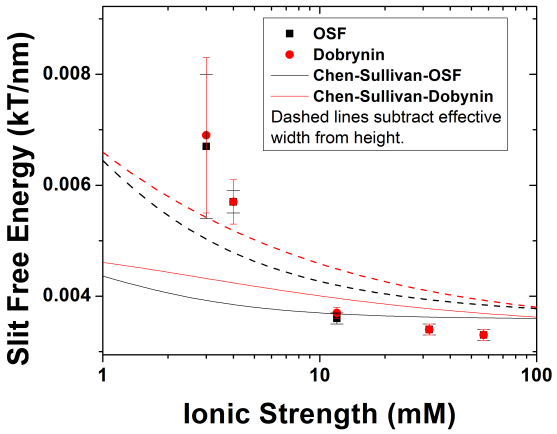

Figure 3–13: Measured A_{slit} and theoretical predictions for the two models of the ionic dependence of persistence length.

the effective width and its scaling with ionic strength on a single-molecule basis. I have solved two long-standing mysteries: the role of excluded volume under confinement, and the transition between strong and weak confinement.

Beyond the measurements themselves, this analysis further demonstrates the power of using complex nanofluidic devices. The measurements take advantage of the multple confinement scales within a given lattice, without which partitioning would be impossible, and the multiple experimental regions on each device, which allows the parameters to be fit to the occupancy scaling. These measurements are also significant in that they begin to look at the actual values of quantities predicted by polymer theory, rather than just their scalings. This will become an important tool as the field moves towards complex phenomena that cannot be simply described by a power law.

From an applications perspective, the single molecule tetris assay can serve as a general laboratory for examining more complex biochemical phenomena, such as the physical effects of DNA-binding proteins like RecA. The

full validation of the free energy model can allow an accurate prediction of the average occupancy, useful for designing devices to trap DNA with certain configurations, like zero-mode waveguides. This will allow a more efficient design of complex nanodevices for trapping DNA, both by allowing a specific state to be tailored by the choice of geometry, and by characterizing the conditions required for DNA to be trapped at all.

CHAPTER 4
Single Molecule Pong: Fluctuations Between Two Pits

4.1 Introduction

When a DNA molecule spans multiple pits, the intensity in all the pits is seen by eye to fluctuate. More quantitatively, in a molecule occupying two pits, the intensity can be measured over time and is seen to fluctuate out of phase between the two pits (Figure 4–1). This is intuitive, because there is a fixed number of fluorophores (fluorescence is proportional to local monomer concentration) and when DNA leaves one pit it will enter another. In this section, we focus on the time-scale associated with contour transfer. We are interested in measuring this time-scale and understanding it theoretically. This section is not a "big picture" exploration of the underlying physics, but rather an investigation into how to control these time-scales. From a device perspective, one may wish to minimize the fluctuation time-scale, so that a higher framerate can be used to image genetically independent samples of DNA, or to maximize it, to allow the greatest possible imaging time of a given sample.

First I will discuss some observations that were made about these fluctuations, before outlining the physics required to understand them.

4.1.1 Experimental Considerations

The experiments here are effectively a subset of the previous section, where molecules were observed to occupy two pits for long periods of time. Each

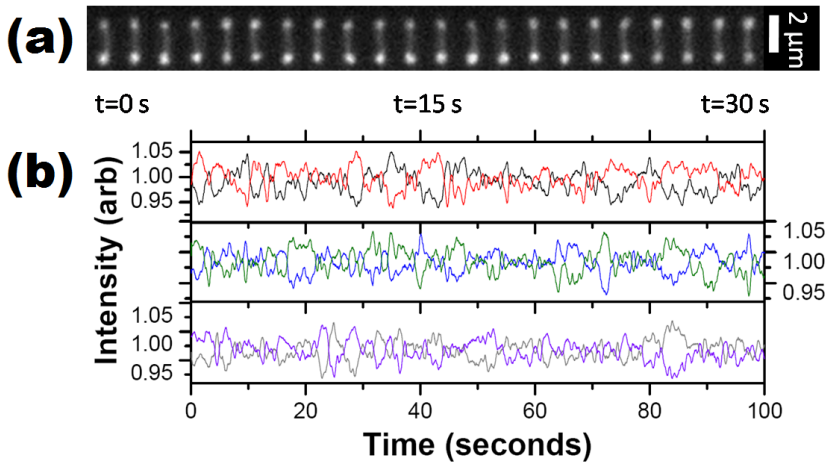

Figure 4–1: (a) A time series of a molecule in two pits showing variations in intensity in both pits. (b) Three plots are shown of the intensity in each of two occupied pits over time. In all cases, the intensities in each of the pits fluctuate out-of-phase with each other.

movie of a molecule in two pits was isolated and oriented vertically. The two intensity peaks were found and a 3x3 or 5x5 pixel box around each peak was summed for each frame, leading to a time-series for each pit intensity, I_1 and I_2. The cross-correlation function of the two time-series was calculated, as were the autocorrelation functions of the sum and difference of the two intensities. Exponential fits were performed.

It was desirable to image at faster framerate, so that short-time correlations could be measured. To this end, in some experiments the molecules were imaged at 30 ms rather then 100 ms exposure.

4.1.2 Observations

Typical time-series of the fluctuating cavity intensities, shown in Figure 4–1, suggest that the cavity intensities are strongly anti-correlated. The large anti-correlation between I_1 and I_2 implies that the difference in cavity intensities $I_{\text{diff}} \equiv I_1 - I_2$ fluctuates with large amplitude (Figure 4–2(b)), while

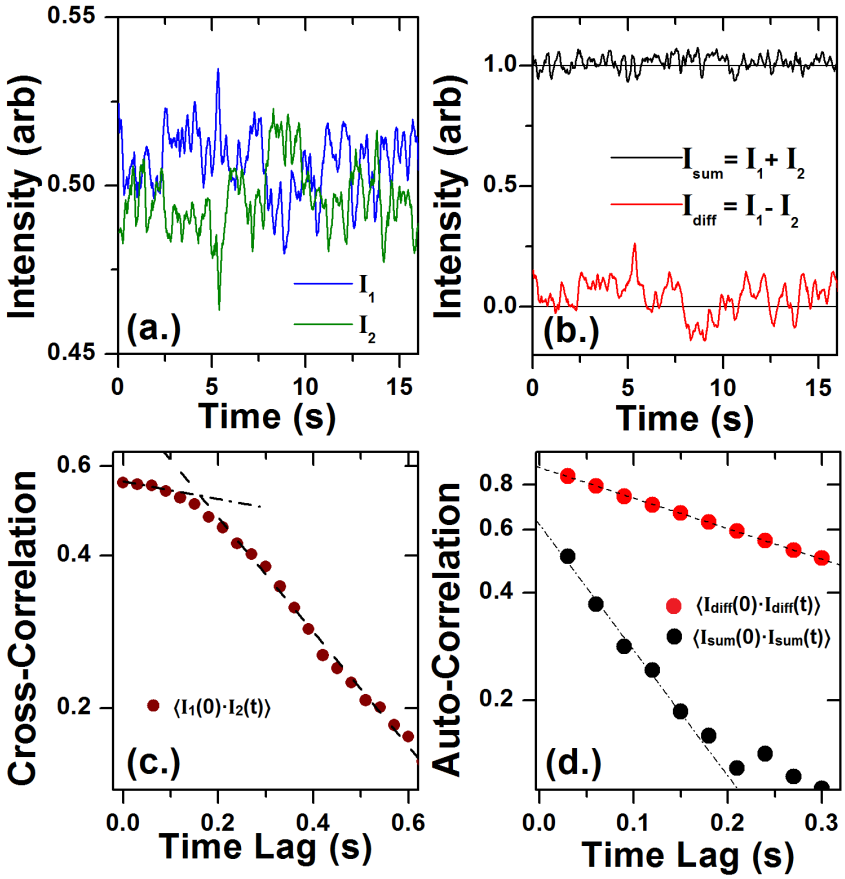

Figure 4–2: (a) Time series of the integrated intensities in two occupied cavities. (b) Time series plot of the summed two-cavity intensity I_{sum} (black) and two-cavity intensity difference I_{diff} (red), corresponding to the two intensities in (a). (c) The cross-correlation of the two data sets in (a), the fluctuating integrated intensity between the two cavities. (d) The autocorrelation of the two data sets in (b), the two-cavity intensity sum autocorrelation $\langle I_{\mathrm{sum}}(0) \cdot I_{\mathrm{sum}}(t) \rangle$ (black) and two-cavity intensity difference autocorrelation $\langle I_{\mathrm{diff}}(0) \cdot I_{\mathrm{diff}}(t) \rangle$ (red) with overlaid exponential fits.

correlations in the sum $I_{\text{sum}} \equiv I_1 + I_2$ are not expected. However, at sufficiently short time-scales, there is evidence of time-correlation in I_{sum} (Figure 4–2(d)), suggesting a faster dynamic mode. Additional evidence for the existence of two relaxation time-scales arises from examination of the cross-correlation of the two fluctuating cavity intensities ($\langle I_1(0) \cdot I_2(t) \rangle$), shown in Figure 4–2(c) for an example molecule (note that the raw cross-correlation function is negative; it has been multiplied by -1). Remarkably, we see that the cross-correlation does not follow a single exponential decay, but instead exhibits two distinct time-scales: a short time-scale $\sim 0.1\,\text{s}$ and a longer time-scale $\sim 0.5\,\text{s}$.

We interpet these two modes as corresponding to two modes of a coupled harmonic oscillator system (Figure 4–3). There is an anti-symmetric mode, where contour fluctuates back and forth between cavities while keeping the tension in the linker constant. This corresponds to the coupled harmonic oscillator mode where the two masses move from side to side, compressing and expanding the springs connected to the wall, while the spring connecting the two remains at its equilibrium extesion. There is also a symmetric mode, where the ratio in the two cavities stays fixed but DNA fluctuates in and out of the slit in tandem, changing the tension in the linking strand. This corresponds to the mode where the two masses move in and out in tandem, stretching and compressing the central spring but keeping the centre of mass fixed. In this analogy, the springs connecting to the walls are the free energy potentials binding the DNA to the cavities, while the central spring is the tension in the chain.

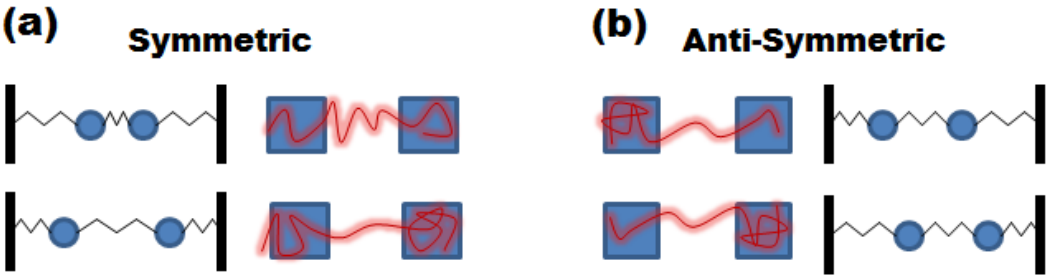

Figure 4–3: Cartoons of the symmetric (a) and anti-symmetric (b) modes, making comparisons between trapped DNA and coupled harmonic oscillators.

4.2 The Physics of Fluctuations

4.2.1 Literature Overview

Initial measurements by Reisner et al. of DNA relaxation times in nanochannels showed a relaxation time-scale on the order of a second, with a local maximum at a transition between two regimes near the Kuhn length [28]. In slits, measurements of diffusion and relaxation time by Hsieh et al. show dynamics in between those described by Rouse and Zimm physics [46]. In a more detailed study, structural time-correlations in slit-confined DNA were examined by Jones et al. who found that the hydrodynamic exponent of internal correlations grew with spatial separation towards a plateau governed by Zimm physics, before decaying as the separation exceeded the size of the channel, providing experimental evidence that hydrodynamic interactions are screened beyond length-scales equivalent to the height of the slit. The internal fluctuation modes of nanoconfined DNA were examined by Karpusenko et al. [33] in the context of density variations along stretched molecules, making analogy to standing wave modes on a string. In bulk, a polymer would undergo fluctuations through a large number of Rouse-type modes, each with its own effective spring constant and relaxation time. In a confining system, the

free energy potential effectively imposes a global spring constant that dictates the molecule's fluctuations. This was realized by Karpusenko et al. [33] who showed that nanochannel confinement lead to several apparent standing wave modes. Confining the molecule in a potential landscape is a way of controlling the dominating mode.

The time-scales associated with molecular partitioning in cavities have largely not been explored. Our earlier work on nanocavity physics focused on static equilibrium physics [1] and diffusion [12]. Nykypanchuk et al. [9] examined DNA fluctuating between two adjacent spherical cavities of different size, focusing on cases where the molecule occupied a single cavity and Cifra [90] modelled the statics of a similar system experimentally in the context of nanopore translocation. Yeh et al. [49] examined a DNA molecule confined over a slit between two reservoirs, to study the forces acting on the molecule as equilibrium is broken. Kounovsky-Schafer et al. [60] examined the time taken for a large molecule spanning two reservoirs across the slit to translocate. Here, we are concerned with the fluctuations of contour between adjacent cavities, for which there has been no quantitative investigation. Beyond merely observing the equilibrium fluctuations of a molecule, we desire to control the fluctuation time-scales via sculpting of the equilibrium ground state.

The time scale of intramolecular fluctuations are governed by two parameters: the effective spring constant κ and the friction factor ξ. The effective spring constant is the curvature of the local confining potential, and the friction factor is the hydrodynamic drag on the chain. The friction factor is sensitive to *hydrodynamic interactions*, the phenomenon where a perturbation of one

part of a chain in solution affects another through coupled motion through the fluid.

4.2.2 Hydrodynamic Interactions

There are two principal models of hydrodynamic interactions within polymers, that predict different behaviours for their relaxation and diffusion at different time-scales. The Rouse model of hydrodynamics treats the chain as a bead-spring system that is subject to Brownian noise and hydrostatic drag. The Zimm model extends this to include hydrodynamic interactions between the beads. The universality of hydrodynamic interactions in the bulk was considered by Tree et al. They found that the dynamics of a chain approach those of Zimm physics as the chain becomes asymptotically long, but that λ-DNA is not in this limit [26].

The prevailing wisdom about hydrodynamic interactions under confinement is that they are screened beyond the length-scale of confinement. Returning to a blob picture, this means that monomers within a blob interact hydrodynamically with each other, but there is no hydrodynamic interaction between blobs. With a blob picture of hydrodynamics, the Rouse model implies that there are no hydrodynamic interactions at all, while the Zimm model assumes that they are relevant within the blob and screened at length-scales beyond the blob length scale, which under confinement is the height of the system. The relaxation time of a free chain in a slit scales as $h^{-1/2}$ for Rouse and $h^{-7/6}$ for Zimm, and experiments [45] showed an intermediate height dependence of $h^{-0.92}$, roughly in between the two limits. A more detailed experiment by the same group [47] fit a stretched exponential to the time-scale of correlation at different separations throughout the molecules, and examined

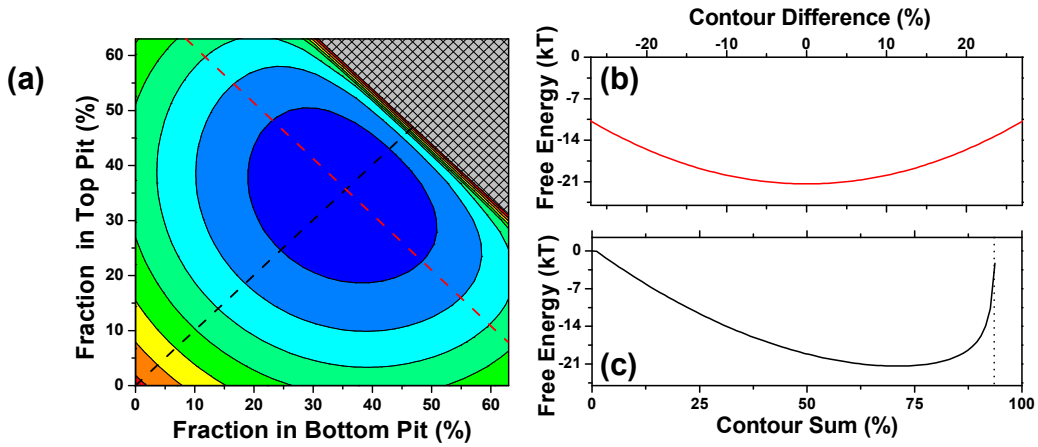

Figure 4–4: (a) A contour contour plot of the free energy landscape of a chain straddling two cavities as a function of the fraction of contour L_1/L and L_2/L stored in each cavity. (b) The energy as a function of $L_{\text{diff}} = L_1 - L_2$ and (c) the energy as a function of $L_{\text{sum}} = L_1 + L_2$. The forbidden region corresponds to configurations where $L_1 + L_2 + L_s > L$.

how the exponent of this fit grew with separation. They found that it grew from the Rouse limit towards the Zimm limit as the distance increased, before reaching a maximum and falling off when the separation exceeded the slit height. Interestingly, they showed that for the heights relevant in this thesis, the hydrodynamics are effectively Rouse-like.

4.2.3 Theory of Two Pit Fluctuations

We return again to the free energy model for the case of $N = 2$, relaxing the restriction that the contour in both pits is equal. Instead of both containing L_p, one contains L_1 and the other L_2, the index of the labels being arbitrary. The ideal chain entropic elasticity is used for simplicity, although a more complex spring model such as Marko-Sigga or de Haan-Shendruk can be used.

$$\frac{\Delta F}{kT} = -AL_1 - AL_2 + BL_1^2 + BL_2^2 + \frac{3l^2}{4pL_s} \tag{4.1}$$

The contour in the slit L_s is such that the total length is conserved: $L = L_1 + L_2 + L_s$. The above expression can be rewritten with a change of basis to the variables L_{sum} and L_{diff}, the total contour in the cavities and the difference between them:

$$L_{sum} = L_1 + L_2 \quad L_{diff} = L_1 - L_2 \tag{4.2}$$

Rewriting the free energy, we have:

$$\frac{\Delta F}{kT} = -AL_{sum} + \frac{1}{2}BL_{sum}^2 + \frac{1}{2}BL_{diff}^2 + \frac{3l^2}{4p\left(L - L_{sum}\right)} \tag{4.3}$$

It can be seen that the only term that depends on the difference is quadratic with respect to L_{diff} with an effective spring constant equal to the excluded volume parameter.

The relaxation time is the ratio of the chain friction to the effective spring constant.

$$\tau = \frac{\xi}{\kappa} \tag{4.4}$$

From blob theory, the hydrodynamic friction on the chain is the friction per blob, taken from the Stokes-Einstein relation, times the number of blobs, whose size is constrained by the height. DeGennes showed that the friction of a chain confined in a nanochannel depends only on the extension along the channel, not directly dependent on the chain length or channel size.

$$\xi = \alpha\eta\ell \tag{4.5}$$

Where η is the buffer viscosity (typically 0.001 Pascal-second) and α is some dimensionless prefactor, typically of order 1 although deGennes uses 6π. This *ansatz* lends itself well to this experimental system: the extension of the molecule is simply the distance between adjacent pits, independent of the tension in the chain. Combining this with our free energy model that tells us that the spring constant κ is equivalent to the excluded volume parameter, we have a simple expression for the relaxation time of the two-pit system.

$$\tau_a = \frac{\xi}{\kappa_a} = \alpha\frac{\eta}{kT}\frac{d}{w}a^2\ell \tag{4.6}$$

The symmetric fluctuation mode does not obey as simple a prediction. The free energy depends on a balancing of all three contributions including the elasticity, rather than just the excluded volume, and the potential is asymmetric about equilibrium. Typically, the second derivative of the potential will be evaluated numerically to find the spring constant. Within the *ansatz* we are using to describe hydrodynamic friction, the friction factors of the two modes should be the same. Thus, the ratio of relaxation times of the two modes is the ratio of their potential curvatures. From this, a very approximate expression can be written for the symmetric relaxation time:

$$\tau_s = \frac{\xi}{\kappa_s} = \alpha\frac{\eta}{kT}\frac{d}{w}a^2\ell\left(1 - \frac{81w^2a^2hp^5L^2}{\left(3wLp^2 - 2\pi^2h^2a^2\right)^3}\left(\frac{\ell}{L}\right)^2 + O\left(\frac{\ell}{L}\right)^4\right) \tag{4.7}$$

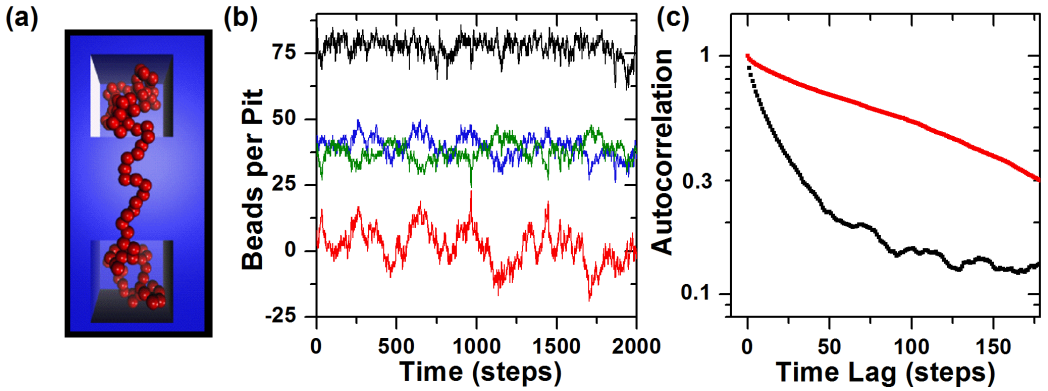

Figure 4–5: (a) Sample image from a simulation. (b) Time series of the number of beads in each cavity (blue, green), as well as their sum (black) and difference (red). (c) The autocorrelation function of the summed bead occupancies for each cavity (black) and the autocorrelation of the difference in bead number for each cavity (red).

4.3 Simulations

To confirm that the two time-scales represent a universal feature of the confined polymer dynamics, and not specific to our specific experimental model, we perform Langevin dynamics simulations of a coarse-grained polymer in a two-cavity system (Figure 4–5(a)). As shown in Figure 4–5(c), both the symmetric and asymmetric modes were reproduced by the simulations. This verifies that it is possible to observe both modes of oscillations in a simple system consisting of a standard bead spring polymer model between two entropic traps subject to thermal noise.

The Langevin dynamics simulations use a coarse-grained method to model the molecule as a chain of connected monomers [91]. Excluded volume interactions are implemented by a Lennard-Jones repulsion (known as the Weeks-Chandler-Anderson or WCA potential in this context [74]) between monomers, which gives them an effective diameter δ which is analogous to w and sets the

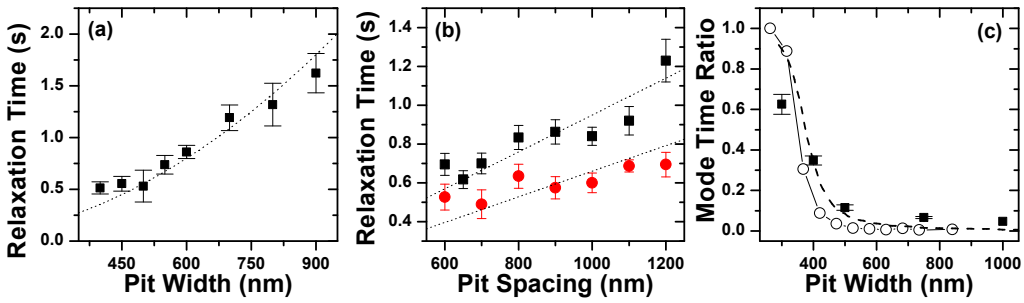

Figure 4–6: (a) Measurements of anti-symmetric correlation time as a function of cavity width compared to a quadratic dependence. (b) Measurements of the anti-symmetric correlation time as a function of cavity-to-cavity spacing, for 500 nm (red) and 600 nm (black) wide cavities. Theoretical prediction of free energy model is overlaid. (c) Ratio of the correlation times of the symmetric mode to the anti-symmetric mode τ_s/τ_a, compared to the free energy model prediction (dashed curve) and the Langevin dynamics simulations (connected circles). Error bars represent standard error between multiple molecules.

length-scale of the system. A polymer chain consists of 100 to 300 monomers, connected via a finitely-extensible spring potential. Semi-flexiblity is imposed by a harmonic bending potential with a spring constant chosen to give an effective persistence length of 5δ, giving the chain similar monomer isotropy to DNA. The chain was simulated in a slit with walls separated by 2δ with square pits of depth 5δ and varying width and spacing. Pits of width 5-16 δ and spacings of 6-16 δ were simulated for 10,000 time points. Geometric parameters were not necessarily chosen to match experimental parameters, but to ensure stable two-pit occupation. The relaxation times were calculated by fitting the exponential decay over the first 10 time-lag steps of the correlation functions of the simulation time-series (Figure 4–5).

4.4 Experiments and Analysis

Our free energy analysis suggests that the fast and slow time-scales observed in experiments and simulations arise from the symmetric and asymmetric transfer modes. We see only one relaxation time-scale in the autocorrelation functions $\langle I_{\mathrm{sum}}(0) \cdot I_{\mathrm{sum}}(t) \rangle$ and $\langle I_{\mathrm{diff}}(0) \cdot I_{\mathrm{diff}}(t) \rangle$ because I_{sum} and I_{diff} represent independent modes. The cavity pair-correlation function $\langle I_1(0) \cdot I_2(t) \rangle$, according to our model, is the sum of the correlation functions for the independent sum and difference modes, explaining why we observe two distinct-time scales in Figure 4–2(c).

Moreover, if our model is correct, we would expect to see the dependence of τ_{a} and τ_{s} on device parameters predicted by Eq. 4.6 and Eq. 4.7. Measurements of τ_{a} as a function of cavity width (Figure 4–6 (a)) suggests that τ_{a} has a dependence on cavity width consistent with the quadratic scaling predicted by Eq. 4.6. Using known geometric values and an effective width $w = 9$ nm from theory, Eq. 4.6 predicts an $\alpha = 0.48 \pm 0.02$. Measurements of τ_{a} as a function of cavity-to-cavity spacing (Figure 4–6 (b)) are consistent with the linear dependence predicted by Eq. 4.5. The friction prefactor of roughly $1/2$ that we observe is significantly smaller than the 6π deGennes predicted based on the Stokes-Einstein coefficient of a spherical blob. More detailed simulations [92] and measurements [28] of relaxation in nanochannels suggest a friction prefactor on order unity. The deviation from the deGennes prefactor is likely due to the asphericity and deformability of the blobs, leading to deviations from the hard-sphere coefficient, as well as latent hydrodynamic interactions that are not fully screened.

As seen in Figure 4–2 (d), the symmetric mode typically relaxes faster than the anti-symmetric mode. The ratio of the two relaxation times is, however, highly sensitive to the cavity width (Figure 4–6(c)). The spring constant associated with the symmetric mode arises from the curvature of the free energy potential landscape at equilibrium (see Figure 4–4). This curvature is strongly related to the tension in the linker. High tension leads to a high κ_s. However, as the tension at equilibrium decreases, the curvature of the potential softens, and the spring constant decreases. Moreover, increasing the cavity width pulls contour out of the slit and increases the tension. A small cavity width leads to low tension. Consequently, the behaviour of τ_{s} as a function of cavity width is opposite that of τ_{a}. As the width of the cavities becomes smaller (lower tension), we expect the ratio $\tau_{\mathrm{s}}/\tau_{\mathrm{a}}$ to increase. Experimental measurements of $\tau_{\mathrm{s}}/\tau_{\mathrm{a}}$ are shown in Figure 4–6(c) and compared to the predictions of our free energy model. We find decent qualitative agreement, although the theory overestimates $\tau_{\mathrm{s}}/\tau_{\mathrm{a}}$ for small cavity width. Our theoretical model assumes that only the curvature of the two modes differs (i.e. it uses the same friction for both), meaning that the ratio of time-scales is given by the function G in Equation 4.7. It is possible that tension reduces the blob length-scale to below that of the confinement scale h, giving rise to a tension dependent friction factor. However, the tension blob length-scale is typically larger than h, thus we expect these differences to be insignificant.

Due to a wide gap between the experimental and simulation contour length- and time-scales, it is difficult to precisely map the simulation results to experiment. Instead, the dimensionless mode ratio as a function of cavity size is compared between the simulations and experiments as shown in Figure 4–6

(c). We have rescaled the bead diameter by a factor of 52 nm/σ to match experiments. This rescaling includes a factor of 9 nm/σ to match the bead diameter to the effective width and a factor of 5.8 from a simple scaling argument that would ensure two-pit occupancy if the chain were lengthened to match λ-DNA. We find comparable agreement to the data that is seen using the free energy model (equation 4.7). In both cases, there is deviation from theory for small cavity sizes, where the symmetric mode is faster than expected. Nevertheless, the trends found in the experimental data, the simulation results, and the thermodynamic model are consistent.

From an engineering point of view, these considerations suggest a series of design guidelines for controlling the fluctuation modes. The time-scale of the dominant asymmetric mode can be increased by increasing the size and spacing of the traps, and conversely this time-scale can be minimized by shrinking the size and spacing. For fast relaxation and no symmetric mode, large cavities can be placed close together. For fast relaxation with a strong symmetric mode, small cavities can be placed close together. For slow relaxation with a symmetric mode, large cavities can be placed far apart, and for slow relaxation with a strong symmetric mode, small cavities can be placed far apart.

4.5 Further work

4.5.1 Noise Budget

The intensity fluctuations measured for any individual pit are a sum of true molecular fluctuations, local noise (for example shot noise reaching each individual pixel), and global noise (for example due to fluctuations in lamp intensity). For a molecule straddling two pits, we can examine the autocorrelation of each pit individually, of the sum and difference of the two intensities,

and the cross-correlation between the two pits to examine how each noise source affects the correlation. In particular, the extrapolated zero-time-lag auto-correlation represents the fraction of the total signal variance that is correlated, and its counterpart is the noise magnitude.

Because the global noise affects both pits simultaneously, the difference between them is unaffected by it. The only noise contribution to the difference autocorrelation is local shot noise. Each individual pit autocorrelation noise will simply be the sum of local and global noise. The cross-correlation will only be sensitive to global noise because the shot noise affecting each pit is uncorrelated, however it emergences from a combination of pro- and anti-correlated fluctuations meaning its zero-time-lag value is not a good measure of noise.

Formally, we can write out the noise contributions to the zero-time correlations and expand them in terms of the different sources (global noise σ_g and local noise σ_l), removing terms uncorrelated with each other. For the individual autocorrelation, two-pit cross-correlation, difference autocorrelation, and sum autocorrelation, we have:

$$\langle I_1 \cdot I_1 \rangle = \sigma_g^2 + \sigma_l^2 \tag{4.8}$$

$$\langle I_1 \cdot I_2 \rangle = 2\sigma_g^2 \tag{4.9}$$

$$\langle I_{diff} \cdot I_{diff} \rangle = 2\sigma_l^2 \tag{4.10}$$

$$\langle I_{sum} \cdot I_{sum} \rangle = 2\sigma_l^2 + 4\sigma_g^2 \tag{4.11}$$

This gives us an approximate hierarchy of the different zero-time-lag values, based on the relative strength of local and global noise, and a way to estimate them from autocorrelation functions. For example, looking at the correlation functions seen in Figure 4–7 it is seen that the autocorrelation of the sum has an extrapolated zero-value of 0.93, giving a value of 0.035 for the local noise, and the cross-correlation has a zero-value of 0.76, giving 0.12 for the global noise. From these values, the expected value for the single-pit zero-value is 0.85, which is in between the two measured extrapolated single pit zero-values (0.83 and 0.86). The expected sum autocorrelation zero-value is 0.45, which is close to its extrapolated value of 0.41. A question arises as to why the global noise is so much stronger than the local noise, which may be resolved by measuring lamp intensity over time under controlled conditions.

4.5.2 Higher Order States

In addition the dynamics of two-pit systems, the dynamics of molecules in three or more pits were investigated. The number of pairwise pit-pit correlation functions that can be considered is $N(N-1)/2$. To simplify the analysis, we can consider correlations between nearest-neighbour pits, and correlations between pits at opposite ends of the molecule.

In three pits, there are correlations between the middle pit and its two neighbours, and between the pits at opposite ends (Figure 4–8). It was observed that the correlation between opposite ends was stronger than the nearest neighbour correlations, and over varying pit width showed a much stronger increase. The times associated with the opposite-end mode were comparable to dimers with large extensions. We interpret this as an extension of the pit-to-pit anti-symmetric mode that was discussed in the context of two pits. The

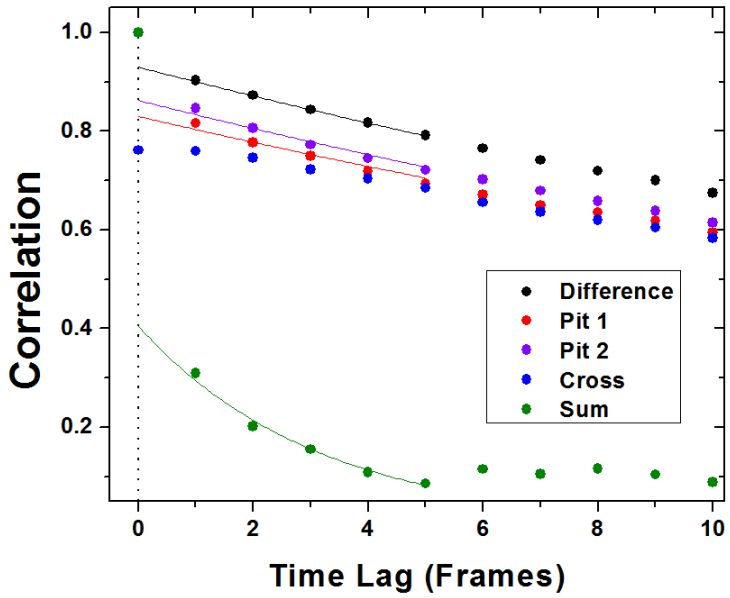

Figure 4–7: Correlation functions for a molecule in two pits: the autocorrelation functions of each individual pit intensity, the sum and difference of intensities, and half the cross-correlation function between the pits. Exponential fits are used to extrapolate to find the zero-time-lag value for each auto-correlation function, which is the fraction of variance due to correlated fluctuations.

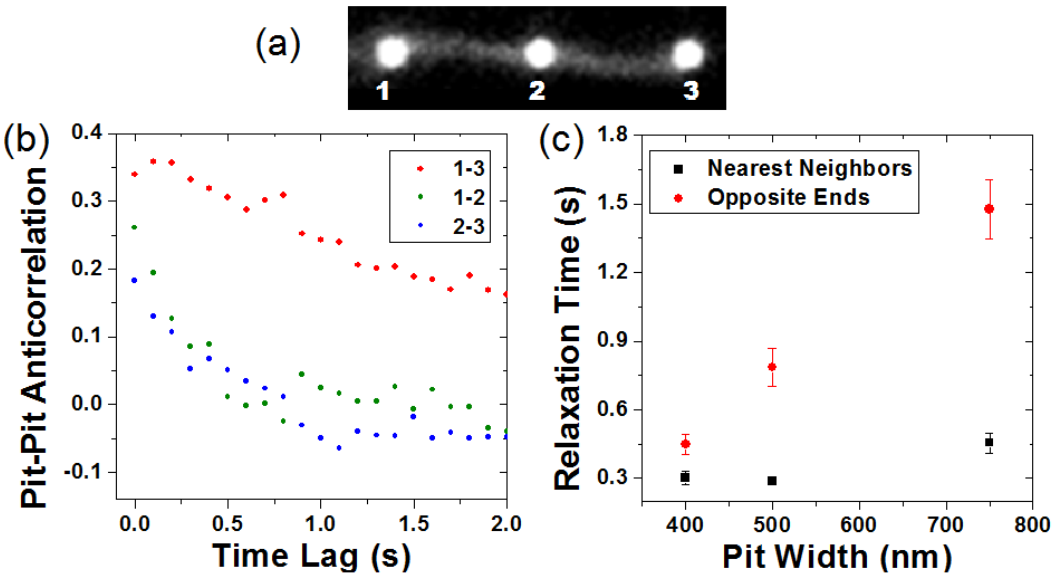

Figure 4–8: Left: Cross-correlation functions for a typical molecule in the three pit state. The pits at opposite ends of the molecule had much stronger anticorrelation compared to nearest neighbours. Right: The relaxation time for nearest-neighbour (averaged) and opposite-end correlations in molecules spanning three pits.

nearest-neighbour correlations are a more complex combination of modes: if contour leaves pit one for pit two, they two would be anti-correlated, but as contour goes from pit three to pits one and two, they both see an increase and would be correlated with each other.

Experiments were performed with T4 DNA to allow molecules to occupy many pits (Figure 4–9). In systems with a large number of pits, it is difficult to make out trends in the correlation functions, although at short times there appears to be a growth across the chain to opposite-end anti-correlation. However, correlated noise, due to the fact that the longest-time fluctuations can only occur a few times in a short movie, makes it difficult to examine longer-time interactions between pits.

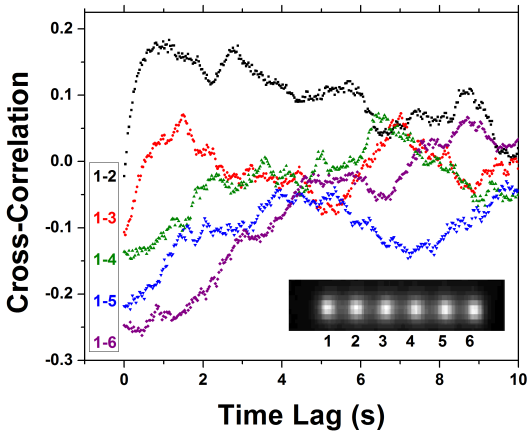

Figure 4–9: Cross-correlation functions between a molecule at one end and the other five of six occupied pits. These have not been multiplied by -1.

There is also suggestive evidence that the peak of the cross-correlation between the opposite ends is not at zero frames, indicating a finite time measurement for tension to propagate from one pit to the other, effectively a "speed of sound" through DNA (Figure 4–10). This can be measured by considering the time at which the cross-correlation function is minimal. For essentially every dimer molecule, there is no evidence of a finite-time offset. For trimer molecules, we begin to see evidence of this offset in the opposite-end correlation. However, it is difficult to get good measurements of this because opposite-end correlations are subject to finite-time fluctuation noise.

By examining kymographs (time-projected averages of movies), fluctuations in intensity can be seen propagating from one side of the molecule to the other, manifesting as local increases in intensity that are staggered in time between pits (Figure 4–11). Based on the time lag in the wave between one side and the other, the speed of tension propagation can be estimated to be roughly 1.6 microns per second.

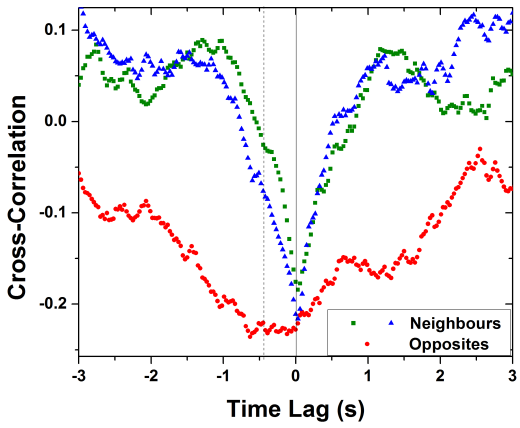

Figure 4–10: Cross-correlation functions for a molecule in the three pit state. The opposite-end correlation has a minimal value at nonzero time.

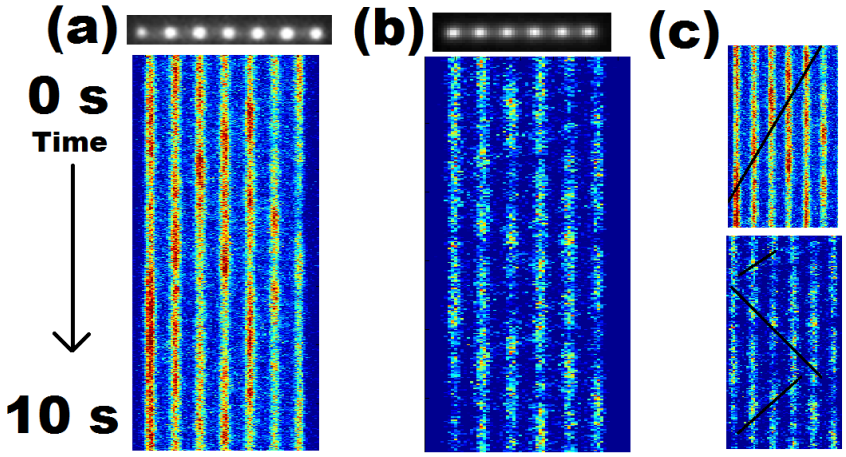

Figure 4–11: (a) Kymograph of a molecule spanning seven pits. An intensity wave can be seen propagating from the fifth to the first pit. (b) Kymograph of a molecule spanning six pits. An intensity wave can be seen propagating back and forth across the molecule. (c) The same images with black lines to highlight the waves.

4.5.3 Tension Blob Scale

The assumptions that lead to the expression for the friction factor rely on the fact that the statistical blob size is the same as the slit height. A stretched chain in bulk has its own tension-blob length-scale, which is the ratio of the thermal energy to the applied force. When considering a stretched chain under confinement, it is not obvious which length-scale dominates, although it is presumed that the smaller length-scale will be more relevant. We can consider both to determine whether tension would affect the confinement blob scale. The blob scale in the linker between two pits can be derived by considering the ideal chain entropic force as a function of L_s and ℓ. It is found that the tension length-scale is:

$$\ell_{blob} = \frac{2}{3} p \frac{L_s}{\ell} \tag{4.12}$$

Without knowing the ration of the L_s to ℓ, it can be ascertained that for the heights used in these experiments, typically on the order of $2p$, the tension length-scale may dominate in the wide-slit high-tension limit. Whether the tension blob scale is smaller or larger than the slit, we can further suppose that the tension blob length-scale manifests itself transverse to the slit in the unconfined directions. An argument for the chain friction based on blob partitioning shows that the friction factor is the same as the extension if the chain obeys ideal statistics within the blob, meaning the transverse tension blob argument gives the same results as the confinement blob argument. If the in-blob statistics are self-avoiding, then a different dependence emerges. However, based on the semi-flexible chain model that we verify in Chapter 3,

it is thought that ideal statistics are appropriate. In particular, this suggests that if the drag acting on the chain is independent of the tension, then the friction factor for the two modes is the same, and the only difference is their spring constant.

4.6 Fluctuation Conclusions

In this chapter, I have made measurements of the correlation-relaxation time of DNA straddling two pits. I developed a model based on the free energy of confinement and blob-style friction to predict this time, and found good agreement between measurements, the model, and numerical simulations. I also showed how imposing the free energy potential landscape with the entropic trapping system can be used to enforce harmonic modes that dominate over the chain's intrinsic Rouse-modes.

There is a rich experimental playground to be found when examining the correlations between molecules occupying a very large number of pits, that I did not have time to explore fully. A systematic study of contour propagation and correlation through these arrays would be a natural next step.

CHAPTER 5
Single Molecule Whac-a-Mole: Filling of a Single Pit

5.1 Introduction

This chapter is about a series of experiments examining molecules occupying a single pit, measuring what fraction of the molecule lies within the pit as a function of the size of the pit (Figure 5–1). The primary motivation is to independently verify the mean-field excluded volume interactions in cavities, which have been taken as an assumption in Chapter 3, and in doing so we explore an under-utilized technique based on measurements of single-molecule partitioning.

In Chapter 3, a model of the free energy of confinement was fit to occupancy data to make measurements of the free energy parameters and their scalings. The model assumed a linear and a quadratic contribution to the free energy with respect to contour, as well as a parameterized elastic contribution.

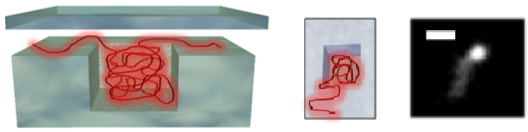

Figure 5–1: Left: A cartoon of a molecule occupying a single pit seen from the side, with some contour inside the pit and some in the slit. Middle: A top view cartoon. Right: A micrograph of a single molecule in one pit, in a similar configuration to the middle cartoon. The bulk of the intensity is localized near the pit, while some originates from the part of the chain in the slit. Scale bar is two microns.

In this section, we attempt to make similar measurements with fewer assumptions, removing sensitivity to the spring parameterization and allowing us to verify the quadratic scaling of the self-exclusion free energy.

When a molecule occupies a single pit, it is partitioned with some contour in the cavity and some in the slit (Figure 5–2). When the pits are very small, the molecule is mostly in the slit with only a toehold in the cavity. When the pits are large, the molecule can fall completely into a single cavity, making occasional excursions into the slit. The fraction of the molecule that fill the pit, which we have termed the "filling factor", depends on a balance of excluded volume pushing it out of the cavities and entropic forces pulling it in, and measuring this filling fraction as a function of the size of the pits provides an independent method of measuring these different free energy parameters.

Compared to slits and channels, studies of polymer physics in confining cavities is sparse. In one study [9], Nykypanchuk measured the probability of DNA occupying one of two adjacent pores of different sizes, and use the probability and size difference to compare to various theoretical predictions. It was concluded that in this case, the theory matched the data better when excluded volume was taken into account. Other studies on cavity-confined DNA have looked at the dynamics of bacteriophage genomes confined within a capsid, concluding that excluded volume is indeed relevant [70].

Much of this research was made possible by the painstaking efforts of two McGill undergrads, Lyndon Duong and Laurence Coursol, who spent many hours in the lab taking data and even more hours in front of the computer implementing the early stages my analysis algorithm, before I was able to automate it. Early work was also done by a CEGEP student, Simon Papillon.

5.1.1 Experimental Considerations

These experiments require molecules to occupy a single pit at equilibrium. Data can be taken from a subset of multi-pit data where $N = 1$, which is common for larger pit sizes, but difficult to get for smaller pits unless they are comparatively far apart. A better method was to use geometries specifically for single λ-DNA molecules, which were five microns apart. These devices contained pits separated by five microns with sizes from 200 to 1000 nanometers, with two rows of each size (Figure 5–2). Rather than focusing on a single geometry, a frame consisting of many geometries was recorded, with a bright-field image used to ascertain which molecules were in which sized pits. Molecules were typically filmed for 300 to 1000 frames.

While the experiments are similar to those in the multi-pit project, the analysis is more complex. Rather than simply counting the number of pits, the intensity coming from within the pit must be measured. Because the pits are only a few pixels wide and comparable to the diffraction limit of the microscope, and it is a challenge to measure this fraction in a way that does not impose a trend.

5.2 Theory of Single Pit Filling

5.2.1 Scaling Model

We return to our initial free energy in the case of $N = 1$, expressing it as a function of the contour in the pit, L_p:

$$\frac{\Delta F}{kT} = -AL_p + BL_p^2 \tag{5.1}$$

This is easily minimized to find the equilibrium value L_o:

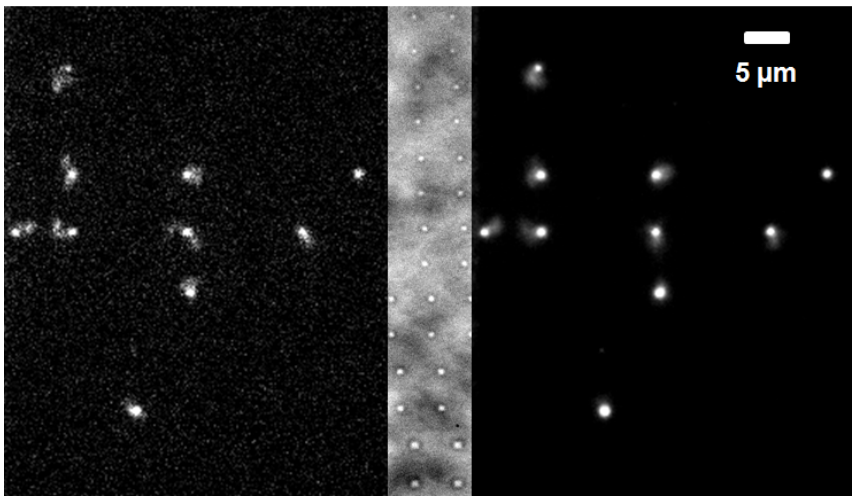

Figure 5–2: A typical single-pit experiment, with a screen capture on the left, a time-projection on the right, and a bright field image in the middle. Molecules occupy a single pit, partitioning some of their contour within. At the top of the image, the pits are small and the molecule is mostly in the slit. At the bottom, the pits are larger, and the less of the molecule is found in the slit.

$$L_o = \frac{A}{2B} \approx A\frac{d}{w}a^2 \tag{5.2}$$

With the geometric definition of B and neglecting transverse contributions to A, we find that this scales quadratically with the width of the pit.

In addition to examining the equilibrium filling, we can also examine the fluctuations about equilibrium by applying the Boltzmann distribution to the free energy:

$$P(L_p) \approx e^{-\frac{\Delta F(L_p)}{kT}} \tag{5.3}$$

Given our free energy, we have:

$$P(L_p) \approx e^{-\left(-AL_p+BL_p^2\right)} = e^{-B(L_p-L_o)^2} \tag{5.4}$$

Thus, assuming the mean field model, the distribution of observed fillings should be Gaussian, with a variance that is related to the reciprocal of the excluded volume parameter. By mapping this expression onto the form of a Gaussian probability distribution we can find the variance:

$$\sigma^2 = \frac{1}{2B} = \frac{2}{\pi}\frac{V}{w} = \frac{2}{\pi}da^2w \tag{5.5}$$

Again, we see that the variance is expected to scale quadratically with pit width, and the standard deviation should be linear in a. It also implies that a measurement of the filling variance of a single molecule would allow a measurement of the effective molecule width.

5.2.2 The Full-Filling Transition

If the cavity is large enough, it can contain the entire molecule at equilibrium, and the potential is minimized at a value of L_p greater than the total contour length. The minimum energy state that can actually occur in this scenario is $L_p = L$, which has some free energy that is greater than the potential minimum, a zero-point energy so-to-speak. This is a finite size effect, that can only occur if the molecule is small enough to fully or almost-fully occupy the pit. This has been explicitly accounted for in the multi-pit analysis: there is an if-statement in the code bringing the minimal energy of the $N = 1$ state to that of full-filling if the true minimum is inaccessible. When this is not taken into account, the monomer state is overfavoured.

The equilibrium filling factor can be found while taking this into account by generating a partition function by integrating the Boltzmann factor by dL_p

from 0 to L. This effectively excludes the inaccessible states from contributing to the ensemble average. Ignoring degeneracy, the partition function is:

$$Z = \int_0^L e^{-AL_p + BL_p^2} dL_p \tag{5.6}$$

This has a closed form expression in terms of error functions which is not particularly useful compared to its integral form. The equilibrium filling can then be calculated:

$$\langle L_p \rangle = \int_0^L \frac{L_p}{Z} e^{-AL_p + BL_p^2} dL_p \tag{5.7}$$

Again, this has a closed form expression that is not worth writing. Substituting geometric values for A and B yields a scaling with respect to a that is quadratic when a is small and plateaus towards full-filling when a becomes large. The variance and standard deviation can also be calculated, from the second moment of the partition function:

$$\sigma^2 = \left\langle L_p^2 \right\rangle - \langle L_p \rangle^2 = \int_0^L \frac{L_p^2}{Z} e^{-AL_p + BL_p^2} dL_p - \left(\int_0^L \frac{L_p}{Z} e^{-AL_p + BL_p^2} dL_p \right)^2 \tag{5.8}$$

Rather than only increasing linearly with pit width, the standard deviation grows, reaches a maximum, then decreases as excursions from full-filling become less likely.

The predictions from minimizing the free energy and the predictions from the partition function are different in the large-pit limit because there are inaccessible states contributing to the free energy. Including the full semi-flexible free energy in the predictions of the partition function model yield a

closed-form but cumbersome expression. To compare to experiments, we can examine both the scalings as predicted by the much simpler model, as well as the predictions of the full model.

5.3 Filling Factor Analysis

5.3.1 The Procedure

The filling factor was measured by calculating the intensity fraction within odd-by-odd boxes around the brightest point in each image, and interpolating to find the contribution from the pit itself (Figure 5–3). These steps were applied to each movie of a molecule occupying a single pit. To distinguish it from other possible analysis procedures, the Procedure will marked with a capital P. The analysis Procedure to calculate the filling factor is as follows.

1. The background, defined as the average intensity on the edge of the projection of the movie, is subtracted from every pixel of every frame.
2. The brightest pixel in the projection is identified.
3. The intensity in odd-by-odd boxes corresponding to 1x1, 3x3, 5x5, and 7x7 stencils around the brightest pixel (Figure 5–3) in each frame is summed, giving four time-series for each movie (Figure 5–4).
4. An odd-by-odd box that is larger than the pit is zeroed, and the pitless movie is convolved by a point-spread function, and the total intensity diffracted into the empty pit (known as the leakage) is summed for each frame, and subtracted from the intensity time-series.
5. A new time-series is found by linearly interpolating between the two (leakage-subtracted) time-series corresponding to the stencil sizes on either side of the true pit size (for example, if the pit is 600 nm wide, and each pixel is 160 nm, the true pit size is between a 3x3 480 nm stencil

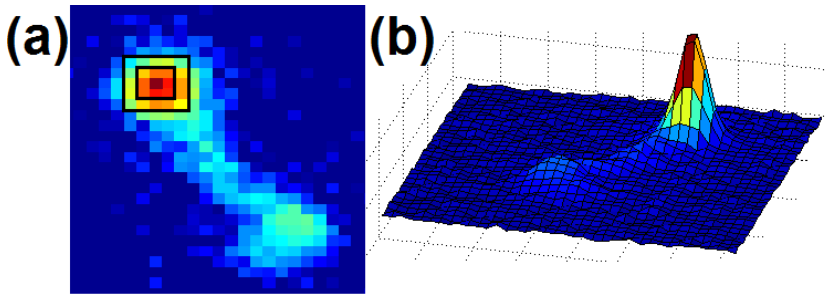

Figure 5–3: (a) For this image of a molecule in a 500 nanometer pit, the boundaries of the pit are within 3x3 and 5x5 pixels of the intensity peak. The filling is calculated by interpolating between the intensity fractions in each odd-by-odd stencil. (b) The 3D surface plot shows the dominance of the pit intensity.

and a 5x5 800 nm stencil). The interpolated time-series is divided by the total background-subtracted intensity of each frame, to measure the filling.

6. The interpolated time-series is divided by an optical fudge factor calculated as the fraction of intensity from a diffracted square source that comes from within the square.
7. The mean and standard deviation of this time series are taken as the measured values.

5.3.2 The Optical Fudge Factor

Even if the dimension of the pit perfectly line up with the pixel grid of the camera, a measurement of the intensity fraction within these pixels will underestimate the filling because of diffraction. The Rayleigh criterion for the optical set-up was roughly 180 nanometers, smaller than the smallest pits but large enough that the intensity coming from within the pit was significantly smeared. Diffraction was taken into account by calculating a "fudge factor." This was the theoretical intensity fraction that is found inside a given square

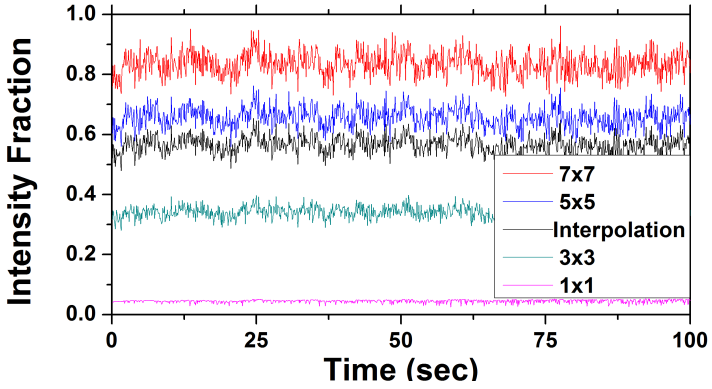

Figure 5–4: The fraction of total intensity within 1x1, 3x3, 5x5, and 7x7 boxes. The black time series is an interpolation between 3x3 and 5x5 to estimate the contribution from the pit.

source that is subject to diffraction (Figure 5–5). It is calculated by convolving an image of a square with a point-spread function and measuring what fraction of the total intensity lies within the original dimension of the box. The fraction of total intensity coming from the box intuitively increases with box size, roughly quadratically for small boxes and square-radically for larger boxes.

5.3.3 Analysis Calibration

To test whether the Procedure can actually measure the filling, I tested it on a series of molecular dynamics simulations from Hendrick de Haan of a molecule confined in a single pit (Figure 5–6), with the same physics described in Chapter 4. Each movie consisted of 200 frames and had a well-defined pit with a known width. To compare the simulations to the data, they were convolved with a point-spread function, coarse-grained into pixels, and speckled with Gaussian noise. The same analysis Procedure used to measure the filling from the data was used to measure the filling from the modified simulation movies, by linearly interpolating between odd-by-odd squares surrounding the

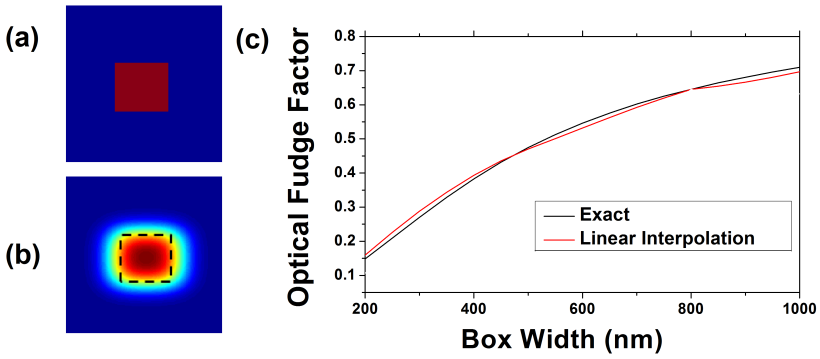

Figure 5–5: (a, b) A square intensity source is convolved with a point-spread function, and the fraction of total intensity originating within the square is the optical fudge factor for that size pit. (c) The calculated fudge factor as a function of pit size based on our microscope optics, and a linear coarse-grained interpolation between odd-by-odd stencils.

brightest point and dividing by an optical factor. Good agreement was found, although increasing the width of the point-spread function or the amplitude of the noise worsens the agreement. In particular, the measured standard deviation increases with increasing noise amplitude. This calibration can be used to refine the analysis Procedure. For example, although intuition suggests that quadratic interpolation between stencil sizes may be more appropriate, the calibration suggests linear interpolation is better.

5.4 Results and Discussion

5.4.1 Time-Series and Histograms

Because the free energy of confinement is roughly quadratic, the probability distribution of the filling is expected to be Gaussian. By examining histograms of an individual molecule's filling time series, it is seen that this is indeed the case. Histograms were created with a method known as superbinning, where the time-series was histogrammed into a too-large number of bins which were then averaged into larger bins to obtain error estimates on the

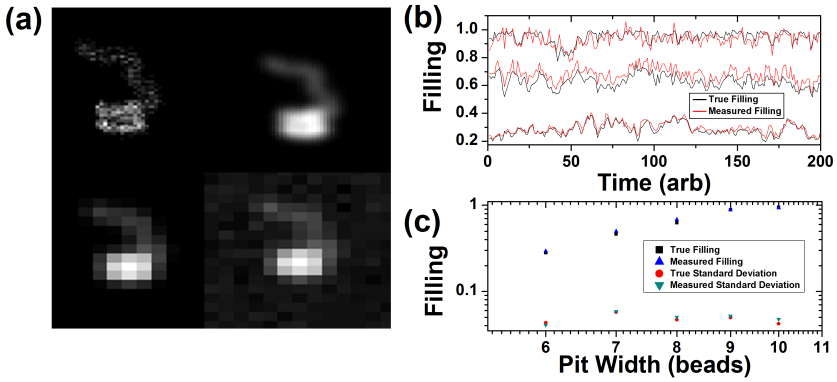

Figure 5–6: (a) A simulation of a chain in a pit is convolved by a point-spread function, coarse-grained by a factor of 4, and speckled with Gaussian noise. (b) The measured filling over time according to the analysis procedure, compared to the true value. (c) Measured and true fillings and standard deviations as a function of nominal pit width.

frequency of each bin. The histograms (Figure 5–7) appeared to be Gaussian as expected from theory. The histograms show that the mean and variance both increase with increasing pit size.

5.4.2 Filling

From the scaling prediction, it is expected that filling increases with pit width quadratically. However, with more detailed theory this is expected to break down in both the large- and small-width limit. For large pits it is expected to plateau as the entire molecule fills the pit, and for small pits, the filling falls below the quadratic level as the transverse entropy becomes significant. It is observed that the filling generally increases with pit width and reaches a plateau for the largest pits (Figure 5–8). Agreement is seen with the theoretical prediction for smaller pits, but for larger pits the measured value lies below the prediction. Evidence for plateaus are seen, but they occur at

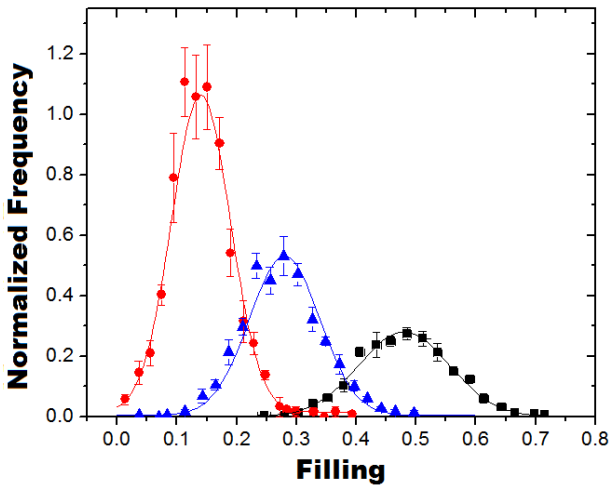

Figure 5–7: Three filling histograms for a molecule in pits width widths of 300 nm (red), 400 nm (blue) and 500 nm (black). They appear Gaussian and the mean and variance of the filling histograms both increase with pit size.

filling levels smaller than predicted. This may be due to an underestimation of the filling at larger pits.

Examining data from pits of the same widths at varying slit height revealed an unexpected trend: the filling reached a peak at around 100 nm slit height, decreasing on both sides (Figure 5–9). This is curious; it implies that a 100 nanometer deep pit can hold more DNA than a 200 nm deep pit. Why does this peak occur? We can write out the single-pit free energy with explicit height dependence, assuming an arbitrary power-law scaling $A = \alpha h^{\gamma}$ for the entropic component, and minimize it:

$$\frac{\Delta F}{kT} = -\alpha h^{\gamma} L_p + \frac{w}{2ha^2} L_p^2 \quad \rightarrow \quad L_o = h^{\gamma+1} \frac{\alpha a^2}{w} \tag{5.9}$$

Thus, given constant pit width, the filling will increase with height if $\gamma > -1$ and decrease with height if $\gamma < -1$. From our understanding of slit

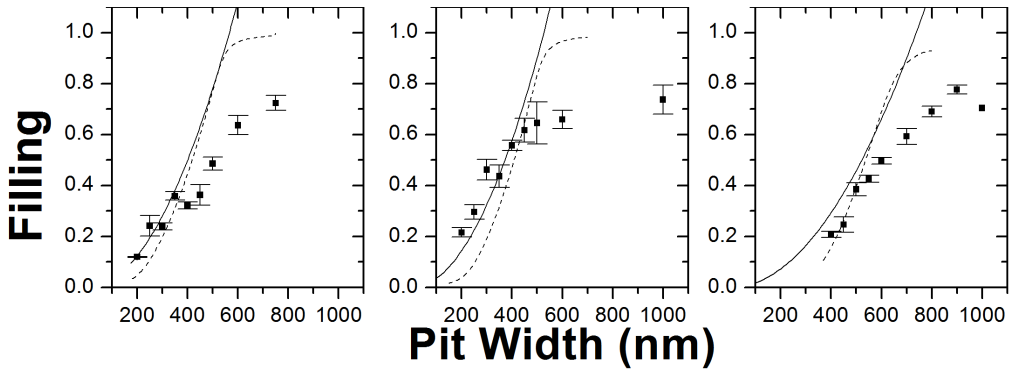

Figure 5–8: Filling as a function of pit width for three data sets, with average heights of 70 nm, 96 nm, and 155 nm (from left to right). In each figure the solid line is the simple scaling prediction and the dashed line is the complete theory.

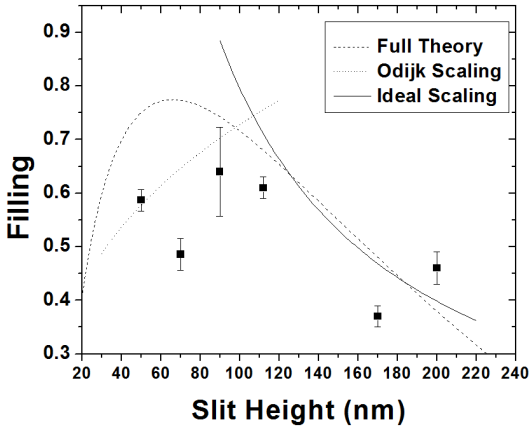

Figure 5–9: Filling for 500 nm pits as a function of slit height, with the prediction of the full theory as well as two scaling predictions.

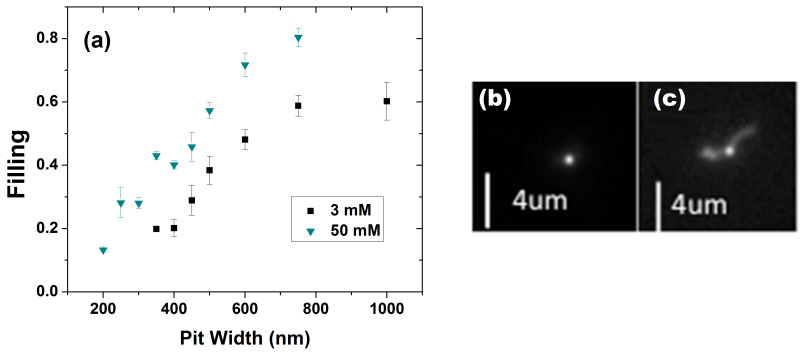

Figure 5–10: (a) Measured filling as a function of pit width in the same device at two ionic strengths. The lower ionic strength has lower filling. On the right, two molecules in the same geometry at two ionic strengths are shown: (b) the 100 mM example is much more localized in the pit than (c) the 10 mM example.

confinement, we expect a transition between the Odijk regime ($\gamma = -2/3$) to the ideal regime ($\gamma = -2$) at around the Kuhn length (100 nm), which is roughly where the filling maximum is located. However, this argument is overly simplistic: using the Chen-Sullivan free energy for the slit, the semi-flexible cylinder model for the cavity, and taking into account finite-size effects, there is a smooth maximum that is expected at a slightly narrower height. The data is not of high enough quality to fully map out this curve.

Experiments were also performed at different ionic strengths (Figure 5–10). It is observed that the filling is smaller at lower ionic strength. As the ionic strength decreases at higher ionic strength, a greater amount of contour can fill the pit without excluded volume interactions driving it into the slit. The salt measurements also provide an additional sanity check on the Procedure: the same geometries yield different results when the experimental conditions are different.

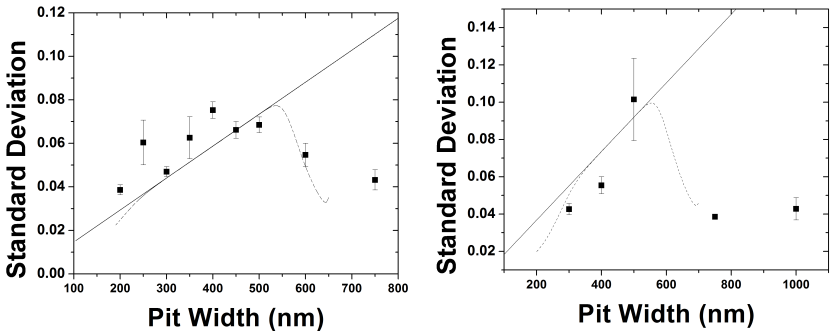

Figure 5–11: Standard deviation of filling as a function of pit width for two data sets, with average heights of 70 nm and 110 nm (from left to right). In each figure the solid line is the simple scaling prediction and the dashed line is the complete theory.

5.4.3 Variance and Standard Deviation

Again, the scaling prediction for the standard deviation of the filling distribution is simpler than the reality. We expect from scaling arguments the standard deviation to have a linear dependence on pit width, and with a more detailed analysis this should fall sharply beyond a certain point, when excursions from full-filling become less common.

Measurements of the standard deviation of the filling distribution as a function of pit width show that it increases towards a maximum and then falls off (Figure 5–11). The data is inherently noisy, as we are measuring fluctuations of fluctuations. The full free energy partition model, taking into account all discussed effects, described the general form of the data well with no free parameters. The partition model is not perfect, as it diverges for sufficiently large pit size (truncated in the figure). It does not exactly predict the experimental values, although it is able to approximately predict the cutoff before the variance falls.

5.4.4 Single-pit Discussion and Conclusions

We have presented partitioning measurements of DNA into cavities of increasing size, and measured that the fraction of the molecule occupying the pit increases with the pit size, but the fluctuations about this fraction reach local maximum before being surpressed. Based on the data that is presented in this chapter, the single-pit investigation failed to achieve most of its goals. The filling data do not convincingly show the quadratic dependence on pit size, nor do they conform to the more detailed theoretical predictions. The standard deviation data are noisy and do not give reliable estimates of the effective molecular width. This is not entirely due to the data quality, as the theoretical aspects of the system turned out to be more complex than initially realized. Despite this, there are still a few useful features that have come out of this analysis. It is undeniable that the filling increases with pit width, and a clear dependence on ionic strength is seen. This provides validity to the concept of single-molecule intensity partition measurements, imperfect though they may be. It also provides evidence of interesting non-monotonic effects in the filling measured with respect to height, and in the standard deviation measured as a function of pit width. Both have implications for polymer physics and device design.

The filling peak serves as a sharp probe of the transition between strong and weak slit confinement, which as shown in Chapter 3 is a subtle feature. There is still controversy in the literature about this transition, and mapping out this peak will provide useful insight that is not available through other means. From a device perspective, it informs us that there is a specific size slit that DNA **does not** want to partition into, which is useful knowledge when

choosing device parameters, for example, designing a section of a device that stores DNA in cavities for future analysis. The location of this peak depends on the pit-slit depth ratio, and tuning it can give a designer a powerful knob with which to control DNA at equilibrium. The non-monotonicity in the standard deviation is not the signature of a confinement regime change, but rather a change in behaviour due to finite size effects, a subject of recent interest [26]. The sharp drop-off in fluctuations after the full-filling transition may guide the design of zero-mode waveguide devices, which may seek to minimize fluctuations.

One of the most challenging aspects of this analysis was the fact that the pits were only a few pixels wide and of comparable to the diffraction limit. In addition to adding ambiguity to the validity of each analysis choice, it also introduced additional sensitivity to optical signal quality, which is not necessarily the same between different experiments. To avoid this issue, the cavities can be coupled to nanochannels rather than slits, and the total extension of the molecule can be used as a metric. This is typically many microns long and is not as close to the diffraction limit, and is easier to measure at low signal strength compared to just the pit intensity. I believe that the results in this section show promise but are limited by issues with diffraction, signal quality, and varying conditions between experiments, and a future recreation in nanochannels would be quite interesting.

CHAPTER 6
Extensions and Conclusions

6.1 Introduction

In this final chapter, I will describe a few projects I investigated that were not developed to completion, but still may be of interest for future readers or attempted replicators. I will also compare the three preceding analyses and suggest future experimental work, before concluding.

6.2 Incomplete Investigations of Interest

6.2.1 Comparison of Intensity Fractions

Rather than examining the equilibrium occupancy, the energetics of confined DNA can be examined by the distribution of intensity in different states. For example, if a molecule is seen transitioning between the $N = 1$, 2, and 3 states, and it is observed that the intensity per pit in the dimer pit is 40 percent as strong as a single pit, and 30 percent as strong in the trimer state, information about the equilibrium contour length can be learned. This is best examined on a per-molecule basis in chains that are observed to transit between multiple states, such that differences in molecule staining ratios no not skew the data. In order to analyze this, the occupancy analysis program can be used to record the integrated intensity within each pit over time, ignoring the optical considerations discussed in the single-pit analysis. If there exists a range of parameter space over which the same two states are common, the intensity ratios can be examined as they scale with pit size or spacing. In more

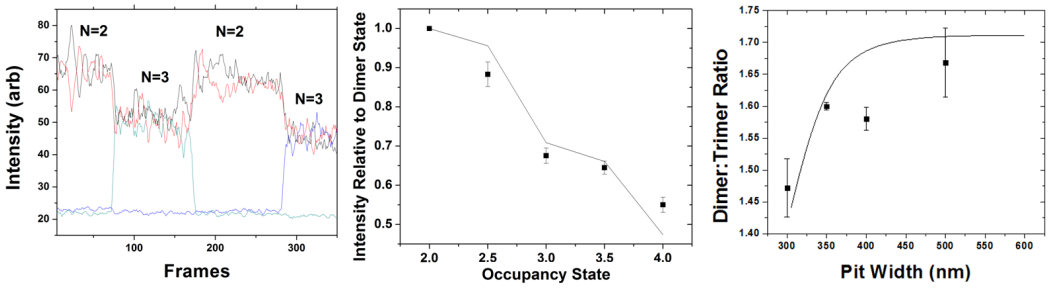

Figure 6–1: Left: Time series of the intensity coming from four pits, two to three of which are occupied at any given time. The intensity per pit in the dimer state is greater than in the trimer state. Middle: Relative pit intensities for a single molecule seen to occupy five different states (.5 represents states with diagonal linkers). Overlaid is a prediction from theory. Right: Averege dimer:trimer intensity fractions measured as a function of pit width, compared to a theoretical prediction.

loosely-bound systems, molecules may occupy many states in a given movie, including diagonal states, so that a single molecules can provide multiple data points. The ratio of the different states can be measured with varying geometry, in addition to the average occupancy, to compare with the theoretical prediction of the free energy model.

Presented in Figure 6–1 is some preliminary data of these intensity ratios, showing the relative intensities between states of a single molecule observed to occupy five different states, as well as the dimer:trimer intensity ratios for an ensemble molecule as a function of pit size. Qualitative agreement with theory is seen.

6.2.2 Two Incorrect Blob Proposals

I explored two models extending the blob argument in regimes where blob scaling does not apply, which ultimately failed to explain the data.

Blob models are typically derived by enforcing that the confinement scale is the size of the blob, and ascribing chain statistics to the physics within the blob and between blobs. As discussed in the introduction, the confinement free energy is the thermal energy times the number of blobs, which is the total contour length divided by the contour length per blob, while the effective radius of gyration is the blob length-scale times the number of blobs. For some confined intra-blob Flory exponent ν_c and an inter-blob exponent ν_b, the free energies and in plane sizes scale as:

$$\frac{\Delta F}{kT} \approx h^{-1/\nu_c} \qquad R_{||} \approx h^{1-\nu b/\nu_c} \tag{6.1}$$

For example, if a chain in a slit is described as a 2D self-avoiding walk ($\nu_b = 0.75$) of blobs containing contour obeying 3D random walk statistics ($\nu_c = 0.6$) then the expected size-scaling is $h^{1-.75/.6} = h^{-.25}$ and the expected free energy scaling is $h^{-1/.6} = h^{-1.66}$. I thought to use the relationship between the free energy scaling and the size scaling to find new theoretical predictions.

My first such idea was inspired by the paper by the Dorfman group [26] showing that the effective Flory exponent of DNA depended strongly on its length, falling from 1.0 to a minimum of about 0.52 and rising up to .588. They calculated an exponent specifically for λ-DNA of approximately 0.56, in between the ideal and self-avoiding limits. I thought that our data for the A parameter, with respect to both height and ionic strength, could be explained using this exponent in a blob model, and I asked Douglas Tree from that group to calculate the exponents for the different ionic conditions in my experiments, which he kindly did. Using the connection between size-scaling and free energy scaling, and the salt-dependent λ-specific Flory exponents I

received, I was able to derive a generalized result to explain both the height and the salt data, although neither set was explained particularly well. Repeating the experiments under more controlled conditions eliminated the need for this investigation. It is conceptually incorrect because these bulk Flory exponents do not necessarily apply under confinement.

My second such idea was an attempt to explain the measured scaling of the in-plane radius of gyration of slit-confined DNA, which does not agree too well with the classic blob scaling [7]. I sought to use the Chen-Sullivan interpolation formula for the free energy of confinement to calculate the "local scaling exponent" for slit confinement, which is found by taking the logarithmic derivative, $d\ log\ F/d\ log\ h$ of the Chen-Sullivan equation (Figure 6–2). The local effective exponent does indeed interpolate between $-2/3$ and -2 with height, but when used to calculate the size-scaling, does not agree at all with experimental conditions. This investigation did reveal an illuminating fact: the experiments in this thesis occur in the regime where power-law scaling is *least* applicable.

6.2.3 Circular DNA

A few experiments were attempted with circular DNA (Figure 6–3). However, the largest circular DNA that is commercially available is 42 kilobase-pairs long, slightly shorter than λ-DNA. To first order, if the molecule remains circular then it will extend roughly half as far along a slit as λ, and will occupy roughly half as many pits. There is not as large a parameter space available over which the molecule can occupy many states, and will often collapse into a single pit. In systems where the pits are close together, such that the molecule occupies more, it is difficult to measure intensity correlations. The ensemble

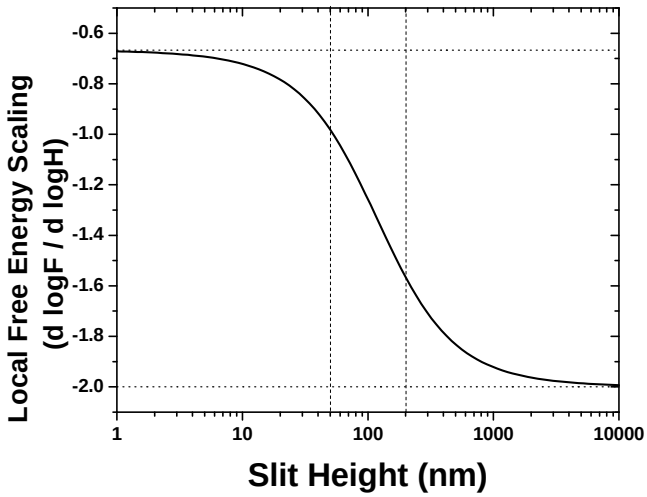

Figure 6–2: Local scaling exponent as a function of height as calculated from the logarithmic derivative of the Chen-Sullivan equation. The experiments in this thesis are in the regime where power laws are least applicable.

of available states is larger for circular compared to linear DNA. A molecule occupying three pits in a right triangle shape can either form a complete triangle with a single linker between each pit, have two double linker connections between nearest neighbours and none along the hypotenuse, or form a double linkage along the hypotenuse and one of the short sides. Initial interest in this was motivated when I was studying diffusion; I was interested in the difference between end-hops and herniations. Nykypanchuk also examined this, with circular DNA in his array of spheres, and he found that circular diffusion was typically slower [55] than its linear counterpart.

6.2.4 Plastic Chips

For our typical fabrication procedure, each glass wafer yields a maximum of nine experimental devices, at a cost typically of over a thousand dollars. Not all nine wafers are typically used in experiments: some are used for SEM

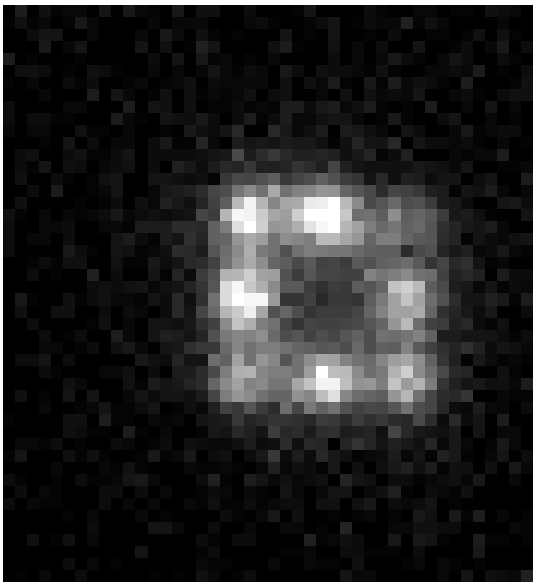

Figure 6–3: A circular DNA molecule occupying a ring of eight pits.

imaging, some do not bond well to cover slips, some crack when being loaded onto the chuck. An alternative to glass fabrication is mass production of plastic chips, which were developed by Peter Friis Ostergaard at the Dansh Technical University as part of the PolyNano collaboration. Peter and Walter published a paper demonstrating that these mass produced and disposable devices could be used for nanochannel genomic mapping [93].

Experimental plastic devices were made using injection moulding. A silicon master wafer was fabricated using standard cleanroom methods and a nickel shim was grown by electroplating it over the master. This was used as a mould for the plastic chips, which were created en masse by flowing molten plastic over the mould. There were several potential advantages of the plastic chips, chiefly their indestructability and the fact that they could be produced by the dozen. The chips I designed contained a number of nanopit geometries for single- and multiple-pit experiments, a series of nanochannels for genomic

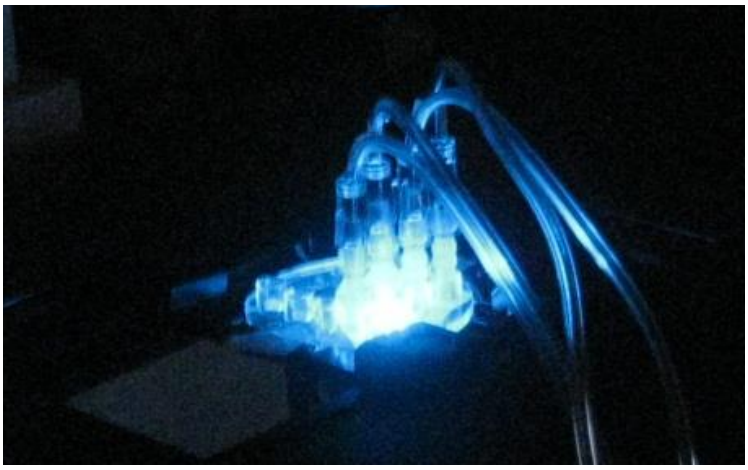

Figure 6–4: Photograph of a plastic chip set up for an experiment, illuminated by the filtererd lamp. Four Luer lines connect directly to the chip reservoirs.

mapping, and a series of funnel-shaped nanochannels for confinement spectroscopy experiments. The chips had Luer connectors built in, and could be operated directly on the microscope positioning stage without a chuck (Figure 6–4). Lyndon and Laurence devised several clever schemes for performing the experiments.

We performed several experiments with DNA in these devices but a number of experimental issues made the plastic chips unsuitable for the type of quantitative measurements required for these experiments. There was a greater propensity for wall-molecule sticking, which was partially mollified by wetting the chips first with ethanol and then with Triton-X surfactant, but was never fully eliminated. It was also very difficult to bring the fluid to mechanical equilibrium, due to the much larger reservoirs that couldn't be fully sealed and the formation of bubbles due to uneven wetting. It was nearly impossible to prevent constant flow, even compensating with back-pressure of several hundred millibar. In addition, the structure of the pits was uneven, as evidenced by

fluorescene images of them, which may be due to the process of molten plastic drying over these nanostructures. Ultimately we chose to return to the glass chips.

6.2.5 COMSOL Solutions for Boundary Conditions

We have assumed that the difference in free energy of confinement for a chain partitioned between a slit and a cavity is simply the difference between the contributions of both the slit and the cavity. However, this assumes boundary conditions where the concentration vanishes at the walls of the cavity, which may not be the case at the virtual interface above the etched pit, where the boundary conditions are not known.

To test this, a McGill undergraduate, Mikhail Mamaev, used COMSOL to solve the modified diffusion equation in a geometry similar to the one used in experiments (Figure 6–5). He calculated the energy eigenvalue for the diffusion equation in a three dimensional square anisotropic slit with a pit at the centre. This was iterated for a range of slit heights and pit widths. The energies for the pure-slit case were used as a calibration, and the difference between the pure-slit energies and the slit-pit energies were compared to the scaling predictions of the ideal chain, assuming typical Dirichlet and Neumann conditions.

Generally, the ideal model underpredicted the energy difference, and fell off more quickly than the calculated eigenvalue. However, it remains to be seen how the semi-flexible eigenvalue solutions would behave in such a geometry. A general investigation of boundary conditions at confinement interfaces would be an interesting theoretical project.

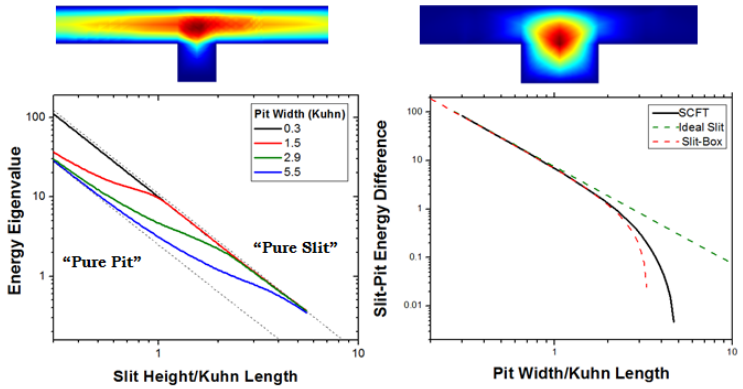

Figure 6–5: Top: Cross sections of the concentration distribution inside the slit-pit systems solved by Mikhail in COMSOL, for a narrow and wide pit. Bottom left: Energy eigenvalues as a function of slit height at fixed pit width, interpolating between the cavity prediction when the height is small, to the size prediction when the height is large. Bottom right: Difference between slit and pit energy, compared to the prediction of the ideal chain with reflecting boundary conditions.

6.2.6 Freezing and Melting

Ilja Czolkos, a former postdoc in our lab, was experimenting with lowering the temperature of the buffer during nanochannel experiments in order to reduce fluctuations and noise. His experimental setup involve dropping small pieces of dry ice into the borehole of the chuck, while using a pump to blow away condensation from the bottom of the chip, using an air-objective. Out of curiosity, I attempted this in a nanopit device, and managed to freeze the entire contents of the chip. The most noticeable effect of the freezing is that the expansion of water into ice, increasing the volume by roughly 10 %, leads to a propagating front of ice that either pushes DNA out of the way or traps it between different ice domains or between the ice and the walls. In a bright-field observation, dendritic ice crystals were seen to form in the microfluidic reservoirs.

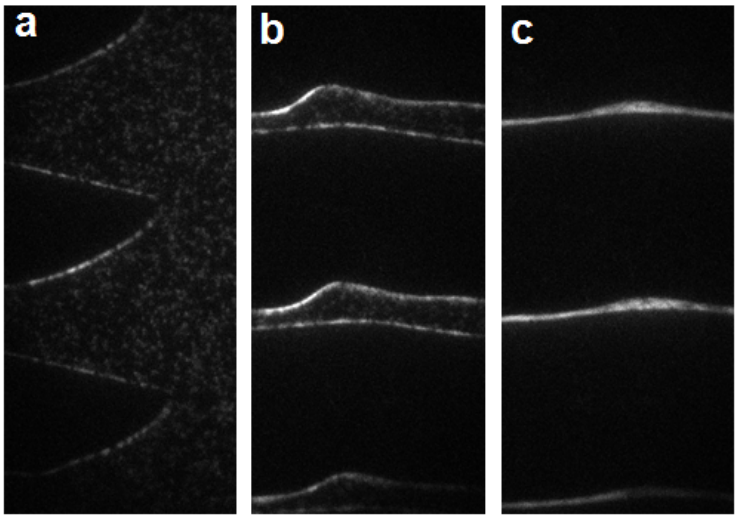

Figure 6–6: (a) Finger-like ice crystals propagate from left to right, pushing DNA-containing liquid out of the way. (b) The remaining liquid and DNA collects in between the domains. (c) Highly concentrated lines of DNA remain.

This lead to a series of curiosity driven experiments exploring freezing and melting as a means of controlling DNA. In one experiment, I watched DNA on a cover-slip and placed dry ice on one side of the microscope slide. This lead to a propagating freeze-front of finger-like ice crystals, that trapped DNA at the grain boundaries, as salt and DNA were excluded from the crystal structure leaving a higher-salt region between the domains (Figure 6–6). I experimented with the idea of using crystal propagation to stretch out DNA, and I had some success trapping stretched DNA underneath or in between growing ice crystals.

Another idea we discussed was using micro- or nano-wires to dynamically write and erase microfluidic channels in frozen slabs of ice, and to use the freeze-melt transition as a nanofluidic valve. I experiment with an old nanowire chip designed by Walter, and found that small amounts of current driven through the wire would cause the entire region around the wires to melt. We

designed a device to precisely control the temperature on a chip device, a variant of the standard chuck design with a copper plate that abuts the chip. The temperature in the plate is controlled through dry ice and an electric heating element. I began to design a chip consisting of four nanowire circuits that would melt different types of microfluidic channels and valves depending on which voltages were applied to which circuits, but never made the chip.

I also did some experiments with Ahmed Khorshid using the optical trap infrared laser to write liquid features in ice. I showed that applying the laser while freezing the system with dry ice would allow a create growing or decaying liquid region around the beam. By scanning the laser up and down, we could begin to create transient microchannels. The liquid-solid phase boundary oscillated in phase with the position of the laser.

6.3 Comparison of Analyses

Three separate analyses have been presented: free energy measurements from fitting to occupancy data, filling and variance measurements in single pits, and relaxation time measurements of correlated fluctuations. All of these are considered in light of the free energy model, assuming a full semi-flexible parameterization of the entropic coefficient, a mean field description of the second virial coefficient, and a height-dependent entropic elasticity. Do the different investigations agree with each other, and the theory? The single-molecule Tetris experiments generally validate the model, and its predictions describe the observed behaviour in the correlation relaxation time. The mean field excluded volume model is used to predict the dependence of the anti-symmetric fluctuation mode on pit width, and agrees with the single-molecule tetris analysis if the numeric prefactor is not rigidly set at 6π. The theoretical

prediction for the mode ratio as a function of pit width is that taken from the full semi-flexible parameterization and the confined elasticity, thus agreement between the data and theory also indicates agreement between the tetris and pong analyses. The single-pit measurements sought to verify the quadratic dependence on contour length in the excluded volume, but two factors conspired against this: finite size effects and contributions from the transverse entropy meant that the theory didn't actually predict scaling laws, and ambiguities in the data analysis generally cast doubt over the results. However, good agreement is found between the prediction of the semi-flexible model for the filling of small pits, and of the location of the peak in the variance. Overall, the measurements presented in this thesis are consistent with each other and the free energy model.

6.4 Proposals for Future Experiments

I have proposed two investigations in the body of this thesis: a systematic study of correlations in large-N states to study tension propagation, and using nanochannels coupled to cavities to repeat the single-pit experiments with less noise sensitivity. A general extension to this work would be to replicate the same analysis in nanochannels rather than slits. The pits in these experiments would extend out the sides of nanochannel arrays but would be etched to the same depth, to avoid issues with alignment. A single device could vary the cavity size, spacing, and feature multiple channel widths for a given depth. Many geometries could be sampled within a single image, thus there is the potential for very high scientific throughput within a single device. It is advisable that future devices be designed with circular rather than square cavities, to better match Chen's cylindrical theory.

With the same experimental setup, it would be interesting to probe the breakdown of equilibrium physics as a pressure or voltage imbalance is applied to the system. The effect of larger imbalances has been studied [2] and theoretical papers have examined highly non-equilibrium cases [94]. Measurements of the occupancy and fluctuation behaviour as a function of pressure or flow speed would effectively probe polymer physics in a tilted periodic potential and it would be interesting for example to look at the frequency of transitions with, against, and transverse to the flow. It would also be interesting to examine the transition between molecular motion characterized by hopping, towards a reptation-like process that would occur when large molecules occupy many pits, where the initial injection conditions would define a virtual reptation tube around the molecule. Observing end-pit hops along this tube, and middle-pit herniations transverse to it, could be used to monitor this transition.

The free energy of confined DNA was measured statistically in this work, by comparing observed probabilities to the Boltzmann distribution. Future experiments can attempt to measure these quantities directly. The free energy of confinement is related to the force between the confining walls and the molecule, which is the derivative of the free energy with respect to the confining dimension. Optical tweezers are a proven tool for precision force measurements experiments of DNA, and experiments by Ahmed Khorshid have shown early success at using optically trapped beads as force probes in nanofluidic confinement. A molecule tethered to a bead under confinement can serve as a direct probe of the confinement force, for example, by measuring the force pulling on the bead as a molecule partially occupies a pit, or is attempts to escape into the microfluidic reservoir. The confinement force can also be measured by

coupling the molecule to a force-sensitive system, such as an optomechanical silicon nitride membrane. Incorporating a membrane in a nanofluidic device, as Yuning Zhang has done, may cause the membrane to deform in such a way that it can be detected optically. The confinement force on a fully confined T4 molecule is of order 10 piconewtons, which may be at the limit of detection by this method. Alternatively, the molecule can be confined within a soft surface such as a droplet or a membrane [95], such that the deformation of the confining system can provide information on the force exerted by DNA. A potential system for this involves droplet microfluidics, where droplets of varying sizes containing DNA molecules can be studied.

6.4.1 Future Biotechnology Connections

A large part of the motivation for DNA nanofluidics research is biotechnology that uses nanofluidics to map or sequence DNA. Many of the technologies rely on single-stranded DNA rather than double-stranded, which is much more flexible. Attempting to replicate this research for single-stranded DNA would be worthwhile for the optimisation of zero-mode waveguide sequencing. Potential applications of this research to zero mode waveguide sequencing include a better understanding of how much DNA is in each waveguide and how to deterministically get DNA in its desired location. Another application is nanochannel single-cell genomic mapping, which is being developed at McGill [96]. Parts of the single-cell DNA extraction process require that the DNA remain stationary as the chemical conditions are modified (for example, cell lysis, buffer exchange, dying, and protein removal). Incorporating nanopits as entropic traps to contain and immobilize the DNA during these processes can improve the operation of the device overall. In addition, knowledge of the free

energy of confinement and fluctuation timescale can be useful for knowing, for example, what voltage is required to get DNA into the nanochannel region in an automated process. Another potential technology is nanopore sequencing, which is limited by the large electric fields required to get DNA into the pore. A student at McGill, Yuning Zhang, has successfully incorporated a nanoslit-nanopit-nanopore geometry to exploit entropic trapping to enhance the translocation probability.

6.5 Unrelated Work

If this thesis represents my development into an independent research physicist, two other projects I have worked on deserve mention.

Prior to coming to McGill, I worked in the Focused Ultrasound Lab at the Sunnybrook Research Institute in Toronto, where I developed theory and ran simulations to describe the oscillation of bubbles inside blood vessels and heat transfer to surrounding tissue. The major findings of this research were published in Physics in Medicine and Biology [97]. Throughout this research I became familiar with the Rayleigh-Plesset differential equation, describing the radial evolution of a bubble in a fluid, which does not have a closed form solution. I attempted to generalize the equation to arbitrary spatial dimensions with the intension of being able to solve it in some higher dimension. This was not successful, but during the investigation I developed enough new results to publish a paper in Physics of Fluids [98]. To summarize the paper, I derived the collapse time, resonant frequency, and Rayleigh-Plesset equation for a bubble in arbitrary spatial dimensions, validated an approximation for the collapse of the bubble whose correctness was debated, and showed that the nonlinear

response of a bubble's resonance frequency to initial conditions has a unique form in three dimensions.

In 2013 I began thinking about the problem of falling through the Earth in a tunnel under the influence of gravity. This is a classic undergraduate physics problem, and it can be shown by treating the Earth as a uniformly dense sphere that a falling object can be treated like a simple harmonic oscillator with a period of 42 minutes, the same amount of time it takes to orbit from one side of the Earth to the other. I was interested in how the realistic density profile of the Earth would affect this time, because the fact that the Earth is denser towards the centre means that the gravity would be comparatively stronger than under the assumption of uniform density. I developed a method finding the falling time under an arbitrary gravitational field and used a model of the Earth's interior field based on seismic data to find that it would be 38 rather 42 minutes. I also showed that the time it takes to fall along a cord is not independent of surface distance, as is the case for a uniform sphere, but varies between 42 and 38 minutes. In all cases, the falling time is similar to the time predicted by a constant radial field. Despite being unrealistic, a uniform is applicable to Earth's interior because Earth's mass increases with radius at roughly the second power, almost cancelling Newtonian gravity. This was published in the American Journal of Physics [99]. After its publication, I was interviewed by Science about it, and subsequently "went viral," with stories about me and my paper appearing in news outlets worldwide. I made a brief appearance on the Discovery Channel and was invited to give a guest lecture at the American Association of Physics Teachers conference. I wrote another

small paper on the topic, investigating similar phenomena in other planetary bodies [100].

These two projects were totally unrelated to each other and to my thesis, however they do share one coincidental feature. In the bubble paper, it was shown that in the high-dimensional limit, two formulations of an exponent describing the bubble collapse time vary by a factor of $\frac{\pi^2}{8}$. In the gravity paper, the times taken to fall through a uniformly dense planet and through a planet with a constant interior field differ by a factor of $\sqrt{\frac{\pi^2}{8}}$.

6.6 Conclusion

By observing DNA at equilibrium in a complex nanofluidic device, several novel measurements have been made. Using single-molecule tetris partitioning measurements, we have mapped out the free energy of slit confinement over the transition between the Odijk and ideal regimes and, performed the first systematic analysis of cavity confinement, and made measurements of the effective width as a function of ionic strength on a single molecule basis. By measuring the time-scale of correlated fluctuations between two cavities, we have shown how a free energy landscape can control the dominant fluctuation modes of a dynamic polymer. Developing a method of analyzing single-cavity partitioning has allowed us to observe the restriction of fluctuations due to finite-length effects. The free energy landscape has been used to control macromolecular diffusion, enhancing or damping it by tailoring the energies of the accessible states.

These measurements would not have been possible in a simple nanofluidic device, because partitioning the chain into different regions of confinement

allows this analysis. More importantly, being able to probe multiple environments on a single device, with multiple degrees of freedom to be tuned, allows a multi-faceted investigation.

The typical data analysis method in this field involves applying power-law fits to data, and comparing those to some sort of blob model. Indeed, that is what we initially sought to do with these analyses: measuring the power-scaling of the free energy fit parameters and compare them to the Odijk or ideal regimes, measure the quadratic scaling of the filling measurements as a function of pit width, etc. However, the reality of the situation is more complicated, and taking into account the full host of relevant physical effects means that both the theoretical and experimental results are not necessarily power laws. Rather than just looking at scaling, we can now look at the measured values and the exact predictions of theory, comparing values to values rather than best-fit exponents to power-law predictions.

Beyond just serving as a neat tool for separating DNA by size or forcing molecules into interesting shapes, we have shown that complex nanofluidics can be used to probe polymer physics more precisely than was previously possible.

REFERENCES

[1] Walter Reisner, Niels B Larsen, Henrik Flyvbjerg, Jonas O Tegenfeldt, and Anders Kristensen. Directed self-organization of single dna molecules in a nanoslit via embedded nanopit arrays. *Proceedings of the National Academy of Sciences*, 106(1):79–84, 2009.

[2] J T Del Bonis-O'Donnell, W Reisner, and D Stein. Pressure-driven dna transport across an artificial nanotopography. *New Journal of Physics*, 11(7):075032, 2009.

[3] Walter Reisner, Jonas N Pedersen, and Robert H Austin. Dna confinement in nanochannels: physics and biological applications. *Reports on Progress in Physics*, 75(10):106601, 2012.

[4] Yanwei Wang, Douglas R. Tree, and Kevin D. Dorfman. Simulation of dna extension in nanochannels. *Macromolecules*, 44(16):6594–6604, 2011.

[5] Dirk Stigter. Interactions of highly charged colloidal cylinders with applications to double-stranded dna. *Biopolymers*, 16(7):1435–1448, 1977.

[6] P. G. de Gennes and T. A. Witten. Scaling Concepts in Polymer Physics. *Physics Today*, 33:51–+, 1980.

[7] Elizabeth A Strychalski, Samuel M Stavis, and Jon Geist. A localized transition in the size variation of circular dna in nanofluidic slitlike confinement. *AIP Advances*, 3(4):042115, 2013.

[8] Jie Gao, Ping Tang, Yuliang Yang, and Jeff ZY Chen. Free energy of a long semiflexible polymer confined in a spherical cavity. *Soft matter*, 10(26):4674–4685, 2014.

[9] Dmytro Nykypanchuk, Helmut H Strey, and David A Hoagland. Single molecule visualizations of polymer partitioning within model pore geometries. *Macromolecules*, 38(1):145–150, 2005.

[10] V V Rybenkov, N R Cozzarelli, and A V Vologodskii. Probability of dna knotting and the effective diameter of the dna double helix. *Proceedings of the National Academy of Sciences*, 90(11):5307–5311, 1993.

[11] Hendrick W de Haan and Tyler N Shendruk. Force–extension for dna in a nanoslit: Mapping between the 3d and 2d limits. *ACS Macro Letters*, 4:632–635, 2015.

[12] Alexander R Klotz, Hugo B Brandao, and Walter W Reisner. Diffusion resonance of nanoconfined polymers. *Macromolecules*, 45(4):2122–2127, 2012.

[13] Manish Nepal, Alon Yaniv, Eyal Shafran, and Oleg Krichevsky. Structure of dna coils in dilute and semidilute solutions. *Physical review letters*, 110(5):058102, 2013.

[14] Rae M Robertson, Stephan Laib, and Douglas E Smith. Diffusion of isolated dna molecules: dependence on length and topology. *Proceedings of the National Academy of Sciences*, 103(19):7310–7314, 2006.

[15] Douglas E Smith, Thomas T Perkins, and Steven Chu. Dynamical scaling of dna diffusion coefficients. *Macromolecules*, 29(4):1372–1373, 1996.

[16] Marc L Mansfield and Jack F Douglas. Is duplex dna a swollen random coil? *Soft Matter*, 9(37):8914–8922, 2013.

[17] Alexey Savelyev. Do monovalent mobile ions affect dna's flexibility at high salt content? *Physical Chemistry Chemical Physics*, 14(7):2250–2254, 2012.

[18] M Fixman and J Skolnick. Polyelectrolyte excluded volume paradox. *Macromolecules*, 11(5):863–867, 1978.

[19] Andrey V Dobrynin. Electrostatic persistence length of semiflexible and flexible polyelectrolytes. *Macromolecules*, 38(22):9304–9314, 2005.

[20] AA Brian, HL Frisch, and LS Lerman. Thermodynamics and equilibrium sedimentation analysis of the close approach of dna molecules and a molecular ordering transition. *Biopolymers*, 20(6):1305–1328, 1981.

[21] Taco Nicolai and Michel Mandel. The ionic strength dependence of the second virial coefficient of low molar mass dna fragments in aqueous solutions. *Macromolecules*, 22(1):438–444, 1989.

[22] Jinyong Lee, Sulhwa Kim, Huisu Jeong, Gun Young Jung, Rakwoo Chang, Yeng-Long Chen, and Kyubong Jo. Nanoslit confined dna at low ionic strengths. *ACS Macro Letters*, 3(9):926–930, 2014.

[23] Katrin Günther, Michael Mertig, and Ralf Seidel. Mechanical and structural properties of yoyo-1 complexed dna. *Nucleic acids research*, 38(19):6526–6532, 2010.

[24] M Maaloum, P Muller, and S Harlepp. Dna-intercalator interactions: structural and physical analysis using atomic force microscopy in solution. *Soft Matter*, 9(47):11233–11240, 2013.

[25] Fredrik Persson and Jonas O Tegenfeldt. Dna in nanochannelsdirectly visualizing genomic information. *Chemical Society Reviews*, 39(3):985–999, 2010.

[26] Douglas R Tree, Abhiram Muralidhar, Patrick S Doyle, and Kevin D Dorfman. Is dna a good model polymer? *Macromolecules*, 46(20):8369–8382, 2013.

[27] Jonas O Tegenfeldt, Christelle Prinz, Han Cao, Steven Chou, Walter W Reisner, Robert Riehn, Yan Mei Wang, Edward C Cox, James C Sturm, Pascal Silberzan, et al. The dynamics of genomic-length dna molecules in 100-nm channels. *Proceedings of the National Academy of Sciences of the United States of America*, 101(30):10979–10983, 2004.

[28] Walter Reisner, Keith J Morton, Robert Riehn, Yan Mei Wang, Zhaoning Yu, Michael Rosen, James C Sturm, Stephen Y Chou, Erwin Frey, and Robert H Austin. Statics and dynamics of single dna molecules confined in nanochannels. *Physical Review Letters*, 94(19):196101, 2005.

[29] Walter Reisner, Jason P Beech, Niels B Larsen, Henrik Flyvbjerg, Anders Kristensen, and Jonas O Tegenfeldt. Nanoconfinement-enhanced conformational response of single dna molecules to changes in ionic environment. *Physical review letters*, 99(5):058302, 2007.

[30] Ce Zhang, Pei Ge Shao, Jeroen A van Kan, and Johan RC van der Maarel. Macromolecular crowding induced elongation and compaction of single dna molecules confined in a nanochannel. *Proceedings of the National Academy of Sciences*, 106(39):16651–16656, 2009.

[31] Ce Zhang, Armando Hernandez-Garcia, Kai Jiang, Zongying Gong, Durgarao Guttula, Siow Yee Ng, Piravi P Malar, Jeroen A van Kan, Liang

Dai, Patrick S Doyle, et al. Amplified stretch of bottlebrush-coated dna in nanofluidic channels. *Nucleic acids research*, 41(20):e189–e189, 2013.

[32] Tianxiang Su, Somes K. Das, Ming Xiao, and Prashant K. Purohit. Transition between two regimes describing internal fluctuation of dna in a nanochannel. *PLoS ONE*, 6(3):e16890, 03 2011.

[33] Alena Karpusenko, Joshua H Carpenter, Chunda Zhou, Shuang Fang Lim, Junhan Pan, and Robert Riehn. Fluctuation modes of nanoconfined dna. *Journal of applied physics*, 111(2):024701, 2012.

[34] Damini Gupta, Julian Sheats, Abhiram Muralidhar, Jeremy J Miller, Derek E Huang, Sara Mahshid, Kevin D Dorfman, and Walter Reisner. Mixed confinement regimes during equilibrium confinement spectroscopy of dna. *The Journal of chemical physics*, 140(21):214901, 2014.

[35] Chunda Zhou, Walter W Reisner, Rory J Staunton, Amir Ashan, Robert H Austin, and Robert Riehn. Collapse of dna in ac electric fields. *Physical review letters*, 106(24):248103, 2011.

[36] Ahmed Khorshid, Philip Zimny, David Tétreault-La Roche, Geremia Massarelli, Takahiro Sakaue, and Walter Reisner. Dynamic compression of single nanochannel confined dna via a nanodozer assay. *Physical Review Letters*, 113(26):268104, 2014.

[37] Jonas N Pedersen, Christopher J Lüscher, Rodolphe Marie, Lasse H Thamdrup, Anders Kristensen, and Henrik Flyvbjerg. Thermophoretic forces on dna measured with a single-molecule spring balance. *Physical Review Letters*, 113(26):268301, 2014.

[38] Theo Odijk. The statistics and dynamics of confined or entangled stiff polymers. *Macromolecules*, 16(8):1340–1344, 1983.

[39] M. Daoud and P.G. De Gennes. Statistics of macromolecular solutions trapped in small pores. 1977.

[40] Liang Dai, Johan van der Maarel, and Patrick S Doyle. Extended de gennes regime of dna confined in a nanochannel. *Macromolecules*, 47(7):2445–2450, 2014.

[41] Abhiram Muralidhar, Douglas R Tree, Yanwei Wang, and Kevin D Dorfman. Interplay between chain stiffness and excluded volume of semiflexible polymers confined in nanochannels. *The Journal of chemical physics*, 140(8):084905, 2014.

[42] Abhiram Muralidhar, Douglas Tree, and Kevin Dorfman. Backfolded odijk regime for semiflexible polymers confined in nanochannels. *Bulletin of the American Physical Society*, 60, 2015.

[43] E Werner and B Mehlig. Confined polymers in the extended de gennes regime. *Physical Review E*, 90(6):062602, 2014.

[44] Po-keng Lin, Chih-Chen Hsieh, Yeng-Long Chen, and Chia-Fu Chou. Effects of topology and ionic strength on double-stranded dna confined in nanoslits. *Macromolecules*, 45(6):2920–2927, 2012.

[45] A. Balducci, P. Mao, J. Han, and P. S. Doyle. Double-Stranded DNA Diffusion in Slitlike Nanochannels. *Macromolecules*, 39:6273–6281, September 2006.

[46] Chih-Chen Hsieh, Anthony Balducci, and Patrick S Doyle. An experimental study of dna rotational relaxation time in nanoslits. *Macromolecules*, 40(14):5196–5205, 2007.

[47] Jeremy J Jones, Johan RC van der Maarel, and Patrick S Doyle. Intrachain dynamics of large dsdna confined to slitlike channels. *Physical review letters*, 110(6):068101, 2013.

[48] Yongqiang Ren and Derek Stein. Coulomb forces on dna polymers in charged fluidic nanoslits. *Physical review letters*, 106(6):068302, 2011.

[49] Jia-Wei Yeh, Alessandro Taloni, Yeng-Long Chen, and Chia-Fu Chou. Entropy-driven single molecule tug-of-war of dna at micro- nanofluidic interfaces. *Nano letters*, 12(3):1597–1602, 2012.

[50] Jun Lin, Fredrik Persson, Joachim Fritzsche, JonasO. Tegenfeldt, and OmarA. Saleh. Bandpass filtering of dna elastic modes using confinement and tension. *Biophysical Journal*, 102(1):96 – 100, 2012.

[51] Peter Cifra. Weak-to-strong confinement transition of semi-flexible macromolecules in slit and in channel. *The Journal of chemical physics*, 136(2):024902, 2012.

[52] Liang Dai, Jeremy J Jones, Johan RC van der Maarel, and Patrick S Doyle. A systematic study of dna conformation in slitlike confinement. *Soft Matter*, 8(10):2972–2982, 2012.

[53] Douglas R Tree, Wesley F Reinhart, and Kevin D Dorfman. The odijk regime in slits. *Macromolecules*, 2014.

[54] Dmytro Nykypanchuk, Helmut H Strey, and David A Hoagland. Brownian motion of dna confined within a two-dimensional array. *Science*, 297(5583):987–990, 2002.

[55] Dmytro Nykypanchuk, David A Hoagland, and Helmut H Strey. Diffusion of circular dna in two-dimensional cavity arrays. *ChemPhysChem*, 10(16):2847–2851, 2009.

[56] Erez Lieberman-Aiden, Nynke L van Berkum, Louise Williams, Maxim Imakaev, Tobias Ragoczy, Agnes Telling, Ido Amit, Bryan R Lajoie, Peter J Sabo, Michael O Dorschner, et al. Comprehensive mapping of long-range interactions reveals folding principles of the human genome. *science*, 326(5950):289–293, 2009.

[57] Wesley F Reinhart, Jeff G Reifenberger, Damini Gupta, Abhiram Muralidhar, Julian Sheats, Han Cao, and Kevin D Dorfman. Distribution of distances between dna barcode labels in nanochannels close to the persistence length. *The Journal of chemical physics*, 142(6):064902, 2015.

[58] Walter Reisner, Niels B. Larsen, Asli Silahtaroglu, Anders Kristensen, Niels Tommerup, Jonas O. Tegenfeldt, and Henrik Flyvbjerg. Single-molecule denaturation mapping of dna in nanofluidic channels. *Proceedings of the National Academy of Sciences*, 107(30):13294–13299, 2010.

[59] R.L. Welch, R. Sladek, K. Dewar, and W.W. Reisner. Denaturation mapping of saccharomyces cerevisiae. *Lab on a Chip*, 2012.

[60] Kristy L Kounovsky-Shafer, Juan P Hernández-Ortiz, Kyubong Jo, Theo Odijk, Juan J de Pablo, and David C Schwartz. Presentation of large dna molecules for analysis as nanoconfined dumbbells. *Macromolecules*, 46(20):8356–8368, 2013.

[61] Rodolphe Marie, Jonas N Pedersen, David LV Bauer, Kristian H Rasmussen, Mohammed Yusuf, Emanuela Volpi, Henrik Flyvbjerg, Anders Kristensen, and Kalim U Mir. Integrated view of genome structure and sequence of a single dna molecule in a nanofluidic device. *Proceedings of the National Academy of Sciences*, 110(13):4893–4898, 2013.

[62] Michael J Levene, Jonas Korlach, Stephen W Turner, Mathieu Foquet, Harold G Craighead, and Watt W Webb. Zero-mode waveguides for single-molecule analysis at high concentrations. *Science*, 299(5607):682–686, 2003.

[63] Chris Rowe Taitt, George P Anderson, and Frances S Ligler. Evanescent wave fluorescence biosensors: Advances of the last decade. *Biosensors and Bioelectronics*, 2015.

[64] Grégory F Schneider and Cees Dekker. Dna sequencing with nanopores. *Nature biotechnology*, 30(4):326–328, 2012.

[65] Michael Zwolak and Massimiliano Di Ventra. Dna sequencing via electron tunneling. In *Circuits and Systems (ISCAS), 2012 IEEE International Symposium on*, pages 2295–2298. IEEE, 2012.

[66] Combined nanochannel-nanopore device for single- molecule dna analysis and manipulation.

[67] Alexander S Mikheyev and Mandy MY Tin. A first look at the oxford nanopore minion sequencer. *Molecular ecology resources*, 14(6):1097–1102, 2014.

[68] Hendrick W de Haan and Gary W Slater. Memory effects during the unbiased translocation of a polymer through a nanopore. *The Journal of chemical physics*, 136(15):154903, 2012.

[69] Mario E Cerritelli, Naiqian Cheng, Alan H Rosenberg, Catherine E McPherson, Frank P Booy, and Alasdair C Steven. Encapsidated conformation of bacteriophage t7 dna. *Cell*, 91(2):271–280, 1997.

[70] Nicholas Keller, Shelley Grimes, Paul J Jardine, Douglas E Smith, et al. Repulsive dna-dna interactions accelerate viral dna packaging in phage phi29. *Physical review letters*, 112(24):248101, 2014.

[71] James Pelletier, Ken Halvorsen, Bae-Yeun Ha, Raffaella Paparcone, Steven J Sandler, Conrad L Woldringh, Wesley P Wong, and Suckjoon Jun. Physical manipulation of the escherichia coli chromosome reveals its soft nature. *Proceedings of the National Academy of Sciences*, 109(40):E2649–E2656, 2012.

[72] Bae-Yeun Ha and Youngkyun Jung. Polymers under confinement: Single polymers, how they interact, and as model chromosomes. *Soft matter*, 11(12):2333–2352, 2015.

[73] Suckjoon Jun and Andrew Wright. Entropy as the driver of chromosome segregation. *Nature Reviews Microbiology*, 8(8):600–607, 2010.

[74] John D Weeks, David Chandler, and Hans C Andersen. Role of repulsive forces in determining the equilibrium structure of simple liquids. *The Journal of chemical physics*, 54(12):5237–5247, 1971.

[75] Hsiao-Ping Hsu, Wolfgang Paul, and Kurt Binder. Breakdown of the kratky-porod wormlike chain model for semiflexible polymers in two dimensions. *EPL (Europhysics Letters)*, 95(6):68004, 2011.

[76] Michael Rubinstein and Ralph H Colby. *Polymer physics*. OUP Oxford, 2003.

[77] Masao Doi. *The theory of polymer dynamics*. Number 73. oxford university press, 1988.

[78] Takahiro Sakaue. Semiflexible polymer confined in closed spaces. *Macromolecules*, 40(14):5206–5211, 2007.

[79] Jeff ZY Chen and DE Sullivan. Free energy of a wormlike polymer chain confined in a slit: crossover between two scaling regimes. *Macromolecules*, 39(22):7769–7773, 2006.

[80] M.R. Smyda and S.C. Harvey. The entropic cost of polymer confinement. *The Journal of Physical Chemistry B*, 2012.

[81] Lincoln D Carr, Charles W Clark, and Wilhelm P Reinhardt. Stationary solutions of the one-dimensional nonlinear schrödinger equation. i. case of repulsive nonlinearity. *Physical Review A*, 62(6):063610, 2000.

[82] John F Marko and Eric D Siggia. Stretching dna. *Macromolecules*, 28(26):8759–8770, 1995.

[83] Yeng-Long Chen, Po-keng Lin, and Chia-Fu Chou. Generalized force-extension relation for wormlike chains in slit confinement. *Macromolecules*, 43(24):10204–10207, 2010.

[84] J. Fu, R.B. Schoch, A.L. Stevens, S.R. Tannenbaum, and J. Han. A patterned anisotropic nanofluidic sieving structure for continuous-flow separation of dna and proteins. *Nature nanotechnology*, 2(2):121–128, 2007.

[85] Reto B Schoch, Jongyoon Han, and Philippe Renaud. Transport phenomena in nanofluidics. *Reviews of Modern Physics*, 80(3):839, 2008.

[86] Alexander Klotz and Walter Reisner. Statics and dynamics of confined dna in a nanopit array. In *APS Meeting Abstracts*, volume 1, page 44011, 2011.

[87] YM Wang, H Flyvbjerg, EC Cox, and RH Austin. When is a distribution not a distribution, and why would you care: Single-molecule measurements of repressor protein 1-d diffusion on dna. In *Controlled Nanoscale Motion*, pages 217–240. Springer, 2007.

[88] David C. Sullivan, Tiba Aynechi, Vincent A. Voelz, and Irwin D. Kuntz. Information content of molecular structures. *Biophysical Journal*, 85(1):174 – 190, 2003.

[89] Hugo B Brandao and Walter Reisner. Equilibrium dynamics of single dn a molecules confined to nanopit structures. *McGill Science Undergraduate Research Journal*, 6(1), 2011.

[90] P Cifra. Partitioning of macromolecules between two interconnected spherical cavities. *Macromolecules*, 38(9):3984–3989, 2005.

[91] Gary W Slater and Christian et al. Holm. Modeling the separation of macromolecules: A review of current computer simulation methods. *Electrophoresis*, 30(5):792–818, 2009.

[92] Douglas R Tree, Yanwei Wang, and Kevin D Dorfman. Modeling the relaxation time of dna confined in a nanochannel. *Biomicrofluidics*, 7(5):054118, 2013.

[93] Peter Friis Østergaard, Marco Matteucci, Walter Reisner, and Rafael Taboryski. Dna barcoding via counterstaining with at/gc sensitive ligands in injection-molded all-polymer nanochannel devices. *Analyst*, 138(4):1249–1255, 2013.

[94] Santtu TT Ollila, Colin Denniston, Mikko Karttunen, and Tapio Ala-Nissila. Biopolymer filtration in corrugated nanochannels. *Physical review letters*, 112(11):118301, 2014.

[95] Yolanda Schaerli, Robert C Wootton, Tom Robinson, Viktor Stein, Christopher Dunsby, Mark AA Neil, Paul MW French, Andrew J demello, Chris Abell, and Florian Hollfelder. Continuous-flow polymerase chain reaction of single-copy dna in microfluidic microdroplets. *Analytical chemistry*, 81(1):302–306, 2008.

[96] Sara Mahshid, Mohammed Jalal Ahamed, Daniel Berard, Susan Amin, Robert Sladek, Sabrina R Leslie, and Walter Reisner. Development of a platform for single cell genomics using convex lens-induced confinement. *Lab on a Chip*, 15(14):3013–3020, 2015.

[97] Alexander R Klotz, Liis Lindvere, Bojana Stefanovic, and Kullervo Hynynen. Temperature change near microbubbles within a capillary network during focused ultrasound. *Physics in medicine and biology*, 55(6):1549, 2010.

[98] Alexander R Klotz. Bubble dynamics in n dimensions. *Physics of Fluids (1994-present)*, 25(8):082109, 2013.

[99] Alexander R Klotz. The gravity tunnel in a non-uniform earth. *American Journal of Physics*, 83(3):231–237, 2015.

[100] Alexander R Klotz. A guided tour of planetary interiors. *arXiv preprint arXiv:1505.05894*, 2015.